Development of Diffraction Enhanced Computed Tomography for Imaging Joints

A Thesis Submitted to the College of

Graduate Studies and Research

in the Partial Fulfillment of the Requirements

for the Degree of Master of Science

in the

Division of Biomedical Engineering

University of Saskatchewan

Saskatoon

Saskatoon, SK

Canada

PERMISSION TO USE

In presenting this thesis/dissertation in partial fulfillment of the requirements for a Postgraduate degree from the University of Saskatchewan, I agree that the Libraries of this University may make it freely available for inspection. I further agree that permission for copying of this thesis/dissertation in any manner, in whole or in part, for scholarly purposes may be granted by the professor or professors who supervised my thesis/dissertation work or, in their absence, by the Head of the Department or the Dean of the College in which my thesis work was done. It is understood that any copying or publication or use of this thesis/dissertation or parts thereof for financial gain shall not be allowed without my written permission. It is also understood that due recognition shall be given to me and to the University of Saskatchewan in any scholarly use which may be made of any material in my thesis/dissertation.

Requests for permission to copy or to make other uses of materials in this thesis/dissertation in whole or part should be addressed to:

Head of the Division of Biomedical Engineering

University of Saskatchewan

Room 2B60, 57 Campus Drive

Saskatoon, Saskatchewan, Canada S7N 5A9

- OR -

Dean

College of Graduate Studies and Research

University of Saskatchewan

107 Administration Place

Saskatoon, Saskatchewan S7N 5A2

Canada

ABSTRACT

This research was inspired by a need to discover more refined technologies for imaging growing joints to facilitate research in childhood arthritis, which is among the most common chronic conditions of childhood.

The objective of this project was to develop and test a new technology for imaging growing joints using diffraction enhanced imaging (DEI) combined with computed tomography (CT) using a synchrotron radiation source. DEI is a modality that derives contrast from x-ray *refraction*, *extinction* (an extreme form of scatter rejection), and *absorption* (as in conventional radiography). The ability to add to an image's contrast from the refraction of x-rays, rather than that solely from absorption, generates more detailed visualization of soft tissue and of interfaces between tissues. Additionally, refraction-based imaging allows reduction of absorbed radiation dose by the sample tissue.

For this research, stifle joints from four-week piglet joints were imaged by DEI-CT using the BioMedical Imaging and Therapy (BMIT) beamline at the Canadian Light Source (CLS) synchrotron facility. This new modality for imaging growing joints incorporated a novel feedback control to maintain precise alignment of the analyzer crystal, which is used to re-diffract the beam that passes through the object, throughout the scanning procedure.

Results showed that high-resolution DEI-CT provided three-dimensional images of the bone and soft tissue of growing joints at a resolution on the order of microns. Fine detail within and between all joint structures and tissues, including striking detail of cartilage vasculature, a

characteristic of growing but not mature joints, was demonstrated. This report documents for the first time that DEI combined with CT and using a synchrotron radiation source can generate more detailed images of intact, growing joints than is currently available from conventional imaging modalities. The development of this high resolution imaging system, which provides excellent contrast for both hard and soft tissues, fills an important gap in the suite of imaging modalities available for joint research, particularly during growth.

ACKNOWLEDGEMENTS

Research described in this thesis was performed at the CLS, which is supported by the Natural Sciences and Engineering Research Council of Canada (NSERC), the National Research Council Canada, the Canadian Institutes of Health Research (CIHR), the Province of Saskatchewan, Western Economic Diversification Canada, and the University of Saskatchewan. The authors also acknowledge the support of the CIHR STIHR training grant, Training in Health Research Using Synchrotron Techniques (GR), the NSERC Discovery grant program (DC), and the Canadian Arthritis Network (AR).

Humbly dedicated to the masterful Creator of this great universe, who has blessed my work immensely.

CONTENTS

LIST OF FIGURES

LIST OF ABBREVIATIONS

2D	Two-dimensional
3D	Three-dimensional
BMIT	BioMedical Imaging and Therapy beamline
CCD	Charge-coupled device
CLS	Canadian Light Source
CMOS	Complementary metal–oxide–semiconductor
CNR	Contrast to noise ratio
CT	Computed tomography
DEI	Diffraction enhanced imaging
JIA	Juvenile idiopathic arthritis
MIR	Multiple image radiography
MRI	Magnetic resonance imaging
SNR	Signal-to-noise ratio

CHAPTER 1: IMAGING GROWING JOINTS; ADDRESSING AN UNMET NEED

Introduction

This research was inspired by a need to discover and develop new and more refined imaging technologies to facilitate research in childhood arthritis, which is among the most common chronic conditions of childhood. The imaging modalities described herein, however, are not necessarily specific to childhood arthritis, but offer opportunities for many areas of joint research. It was hypothesized that DEI is capable of providing better visualization of joint tissues than conventional modalities, providing for more effective arthritis research.

Arthritis is a painful disease that is both chronic and debilitating, affecting more than 4.6 million Canadians (Bombardier, Hawker, & Mosher, 2011) and over 27 million Americans (Arthritis Foundation, 2013). Arthritis can have a substantial adverse effect on quality of life and productivity. According to Canadian research data from 2007-2008, arthritis affects 16% of individuals over the age of 15, and this number is expected to rise to 20% in 2031 (7 million affected), due to an aging population (PHAC, 2011). Typically viewed as a disease of the elderly, it is actually among *the most common chronic childhood diseases* (PHAC, 2010).

While juvenile idiopathic arthritis (JIA) provided the initial impetus for this research, joint research in general stands to benefit from an enhanced imaging suite for diagnosis and research. This work focused on the development of an imaging system suited to high resolution imaging of growing joints. The etiology and pathophysiology of chronic

inflammatory and degenerative joint diseases, such as adult rheumatoid arthritis, osteoarthritis, and JIA, are not well understood (Stanich, Carter, & Whittum-Hudson, 2009; Wilson, Mc Walter, & Johnston, 2009). This thesis describes the development and testing of DEI combined with CT for the imaging of growing joints, exploring their ability to detect and detail joint structures that may form the basis of research into the etiology and pathophysiology of chronic inflammatory joint diseases, particularly those that occur during growth.

Research shows that juvenile arthritis has notable differences from adult onset arthritis (Wilson-Gerwing, Pratt, Cooper, Silver, & Rosenberg, 2013). However, undertaking research relating to juvenile arthritis is limited to some extent by the challenges of doing research in children; the requirement for large-scale, multi-centre trials to ensure adequate subject numbers and the clinical and underlying pathogenic heterogeneity among groups of children with arthritis (Petty et al., 2004). Utilizing animal models for studying arthritis during growth, as in this project, can help advance and translate knowledge to the human clinical setting.

Literary Review

A notable limitation to studying joint diseases, especially in children, is the lack of refined imaging tools suited to the specific needs of joint imaging. Without an effective way to non-invasively visualize all relevant joint structures in detail, research to study disease progression and response to treatment interventions is limited. Longitudinal studies can provide insight into pathogenic effects over time, if there is a way to monitor the pathogenic process without altering the process. Unfortunately, the current suite of non-invasive imaging

modalities each has shortcomings for joint research. Invasive visualization, through arthroscopy, is sometimes still required as an investigative tool in chronic arthritis, but is not an acceptable research tool, particularly in children (McKeon, Bono, & Richmond, 2009).

Radiography, CT, magnetic resonance imaging (MRI), and ultrasound are the most common joint imaging techniques. This discussion focuses on x-ray based techniques and MRI.

Conventional X-ray

Traditional, single projection, x-ray imaging is capable of producing a high-resolution 2D image of bone structure. While this involves ionizing radiation, absorbed doses are low, especially compared to CT imaging. While these radiographs are capable of high resolution, they do not produce highly detailed joint images compared to other modalities. Attenuation is not quantifiable, radiographs are insensitive to soft tissues such as cartilage and ligament, and represent a 2D superimposition of the few joint structures that are visible based on x-ray attenuation, including cortical and trabecular structure within the bone. A common way of using x-ray images to determine joint issues is to monitor the change in the space between the bones (Oen et al., 2003). As this space is reduced, it can be inferred that cartilage is degrading.

Since radiographs provide poor soft tissue contrast, cartilage condition may only be assessed indirectly, and the researcher is left with little information on the mode of degeneration or disease development. Additionally, any visible structures are superimposed over one another in a 2D image. While radiography offers a low-dose, non-invasive imaging technique, it has limitations for joint research and diagnosis.

Computed Tomography

CT offers another option for joint visualization, as it does provide high resolution, 3D, quantifiable images. This allows visualization of the skeletal structure in detail and from any angle. Despite micron-level spatial resolution (Burghardt, Link, & Majumdar, 2011), however, CT still has limited soft tissue contrast (contrast resolution). This is because the attenuation coefficients of soft tissues vary little, on the range of about 5% for x-rays in the imaging regimen. Since the difference in attenuation between the tissues is minimal, x-rays are attenuated at nearly the same rate by cartilage, muscles, and ligaments. CT gives excellent resolution of the bone structure, but the rest of the joint is often better visualized with MRI, despite its spatial resolution limitations (see "Magnetic Resonance Imaging" section) (Hegenscheid, Puls, & Rosenberg, 2012). CT's value is also offset by its radiation exposure costs (Frush, 2008). CT scans are the worst common form of joint imaging when it comes to absorbed radiation dose to the sample (Fazel et al., 2009). This is of special concern for studies involving children. While CT has given much insight into bone growth mechanisms and deterioration phenomena, it provides only limited information about the condition of the rest of the joint, specifically the cartilage. The principles of CT are considered in depth in Chapter 3.

Magnetic Resonance Imaging

MRI is a common and valuable tool for joint visualization. It is considered the gold standard in imaging articular cartilage (Gold, Chen, Koo, Hargreaves, & Bangerter, 2009). It provides much better soft tissue contrast than clinical x-ray imaging options (Lee et al., 2005;

Thakkar, Flammang, Chhabra, Padua, & Carrino, 2012) with no requirement for ionizing radiation. However, resolution is still a major limitation of MRI (Vande Berg et al., 2002). While "micro-MRI" has been performed with high field machines or overnight scans using clinical scanners (Schoth et al., 2008; Theysohn et al., 2013), MRI does not match the resolution available with x-ray based systems (Zwanenburg, van der Kolk, & Luijten, 2013). This is due largely to the principle of operation of MRI. The imaging contrast in MRI relies directly on signal from a set of coil antennae. It, therefore, has not benefited from developments in charge-coupled device (CCD) and complementary metal–oxide–semiconductor (CMOS) technology, as have x-ray imaging systems (Björn, 2010; Knoll, 1989). While advancing technologies are resulting in improved MRI imaging of joint structures, limitations in the detail and depth of cartilage damage imaged by MRI remain (Duyn, 2012; Pakin et al., 2006). Detail of cartilage and bone deterioration is still not visible.

MRI creates an image by exciting atoms with a strong magnetic field and detecting the radio frequency signal emitted by those atoms as they are excited and then return to the relaxed state (Rinck, 2015). MRI with 1.5T scanners has been shown to be more effective at detecting bone erosion in JIA than conventional radiography and ultrasound (Malattia et al., 2008). Besides this increased effectiveness at detecting bone erosion, MRI provides the added benefit over conventional radiography of soft tissue visualization. While this is apparent in 1.5T machines, 3.0T MRI scanners significantly increase the detection of cartilage damage over 1.5T models (Masi et al., 2005). The ability to visualize hard and soft tissues makes MRI an exceptionally valuable tool for joint research.

Diagnosis of JIA as early as 2 months from the onset of symptoms has been demonstrated using MRI (Johnson, Wittkop, Haigh, Ryder, & Gardner-Medwin, 2002), and distinction between different types of recent-onset arthritis may be possible using MRI (Kirkhus, Flato, Riise, Reiseter, & Smith, 2011). MRI has the capacity to give information regarding the orientation and hydration of cartilage collagen fibers (Carballido-Gamio, Joseph, Lynch, Link, & Majumdar, 2011; Thakkar et al., 2012).

MRI, along with ultrasound, is now seen as a safer and more effective tool for evaluating JIA than conventional radiography (Johnson & Gardner-Medwin, 2002). As such, it is appropriate to compare and contrast the results of this research with the current abilities of MRI.

Resolution is the greatest limitation of MRI for research on joint pathology. MRI systems obtain image contrast from radio frequency signals – a much different source of contrast from x-ray imaging systems (Reicher et al., 1985). As a result, MRI has not benefited from the advances in CCD and CMOS technology, the way that x-ray imaging systems have. If MRI were used alongside a high resolution imaging system visualizing bone and cartilage, joint assessment could be much more in-depth than with MRI alone.

Discussion

It is clear that the array of imaging techniques available to the medical researcher has limitations when applied to joint research. What is required is a safe, high resolution imaging system with good contrast for all joint structures, and that yields quantifiable information

about the joint structures. Whether available clinically or confined to arthritis research, this type of imaging system would provide a valuable tool. The research described by this thesis centers on the development and demonstration of DEI-CT with regard to these requirements of joint research.

Conclusion

Currently available modalities for imaging joints, particularly during growth, have limitations. This thesis describes a new imaging modality, DEI-CT, that offers an innovative approach to generating more detailed and refined images of bone and soft tissue in growing joints.

Organization of Thesis

Chapter 2 lays out the basic principles of x-ray production, interaction with matter, and diffraction from crystals. Chapter 3 describes the planar DEI research, the objective of which was to test DEI's ability to detect cartilage and soft tissue detail in an intact joint in a single projection. Chapter 4 describes the DEI-CT research, the objective of which was to develop a DEI-CT system at the CLS, and test DEI-CT's ability to detail cartilage and soft tissue detail, as well as its ability to detect simulated damage. Chapter 5 describes the novel control system developed for the implementation of DEI-CT. Chapter 6 is a final conclusion, summarizing the findings of this research and commenting on further research.

CHAPTER 2: DIFFRACTION ENHANCED IMAGING

Introduction

DEI is a form of analyzer-based imaging that uses two images along with an algorithm to produce images with contrast from x-ray refraction, extinction (an extreme form of scatter rejection) and absorption which is common to conventional radiography (Bravin, Coan, & Suortti, 2013; Oltulu, Zhong, Hasnah, Wernick, & Chapman, 2003). In this thesis, the term "DEI" will be used to refer to imaging that utilizes an analyzer crystal and monochromatic beam to obtain refraction information. The ability to add to an image's contrast from the refraction of x-rays, rather than that solely from absorption, generates more detailed visualization of soft tissue and of interfaces between tissues. Additionally, refraction-based imaging allows reduction of absorbed radiation dose by the sample tissue.

Background

DEI came out of a research program designed to explore a monoenergetic line scan system for radiography of thick absorbing objects (Johnston et al., 1996). That original experimental setup included a crystal monochromator, which selected a narrow energy bandwidth of an x-ray beam. That monochromatic beam intercepted the sample being imaged. It was found that an analyzer crystal, of similar type as the monochromator, placed in the beam transmitted from the sample, allowed not only for extreme scatter rejection, but was also

sensitive to refraction of the transmitted beam. This imaging setup produced images of contrast from absorption and refraction. It was also found that when two images were acquired, an algorithm might be applied to separate the refraction and absorption components of the contrast (Chapman et al., 1997). Refraction contrast has proven valuable on many fronts, including, but not limited to: detection of cancer lesions (Pisano et al., 2000; Shtern, 1992); diagnosis of hepatic fibrosis (Li et al., 2009) and emphysema (Dong et al., 2014); visualization of tissue scaffolds (Chapman, Chen, Cooper, Schreyer, & Zhu, 2011), trabecular architecture (Cooper, Bewer, Wiebe, Wysokinski, & Chapman, 2011), cartilage detail (Mollenhauer et al., 2002; Muehleman et al., 2003), and even anatomical structures of plant seeds (Young, Parham, Zhong, Chapman, & Reaney, 2007).

Non-synchrotron X-ray Production

X-rays are produced by accelerating charged particles. X-ray tubes produce radiation by linearly accelerating particles shown schematically in Figure 1. In this production technique, a current is run through a small filament, which forms the cathode of an evacuated tube. A high voltage potential between the filament and the anode of the tube induces a beam of electrons between the two as the electrons are drawn from the vicinity of the hot filament. These electrons accelerate linearly

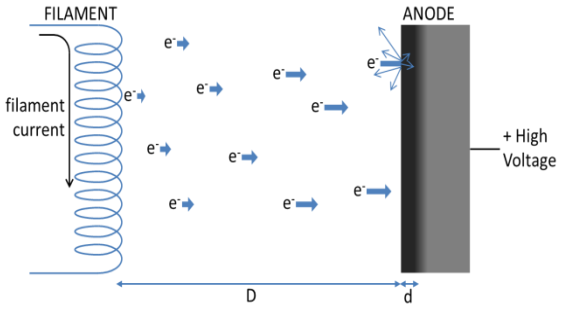

Figure 1: Tube current producing bremsstrahlung upon impact with the anode of the x-ray tube.

through the filament-anode gap, producing a small amount of radiation. However, upon impact with the anode, these electrons experience a much greater (negative) acceleration, producing an amount of radiation several orders of magnitude larger than that produced by the initial acceleration through the gap (Haug & Nakel, 2004). This is because the reduction of velocity upon impact takes place over a much smaller distance than the positive acceleration through the filament-anode gap. The radiation produced by this collision is known as bremsstrahlung, and is the common source of non-synchrotron x-ray radiation.

X-ray tubes are relatively cheap and simple, which is ideal. The use of an evacuated tube, filament, and anode in what was considered to be the first successful source of x-rays was developed by W. D. Coolidge at General Electric (Coolidge, 1916). A Coolidge tube is shown in Figure 2.

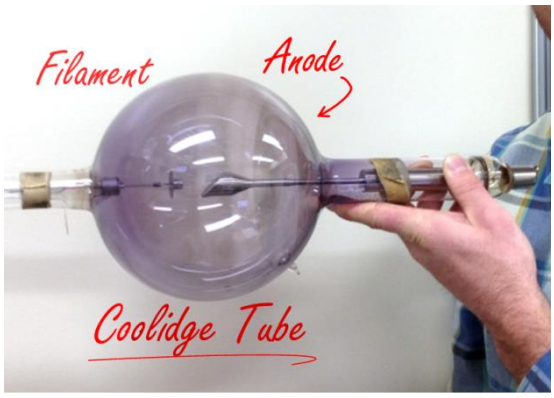

Figure 2: An x-ray tube known as the Coolidge tube, with the cathode on the left and an angled anode on the right. X-rays are showered upward.

X-ray tubes have several characteristics that should be considered. Firstly, radiation from the electron impact with the anode is showered in all directions. Radiation emitted perpendicular to the face of the anode is the most intense, as this radiation is the least shielded by the portion of the anode through which it must travel back out after the electron comes to a stop. Radiation traveling deeper into the anode or parallel to its surface will be more highly absorbed by the anode material. In addition, viewing the electron beam spot on the anode at an angle will reduce the effective size of the x-ray source. For these reasons, most anodes are angled with respect to the incoming beam, so

that the radiation is emitted primarily out of the side of the tube. This very general "focusing" of the beam, however, is not enough for the vast majority of imaging setups, and the beam must be collimated to produce a beam with which to scan a sample and intercept a detector. The angled face of the anode also allows a greater surface over which the energy of the incoming electrons is dispersed.

Secondly, while the energy spectrum from an x-ray tube is overall well-approximated by a smooth curve, in reality it contains spikes, depending on the material of the anode. Emission lines characteristic of the anode material are produced at specific energies (CLS, 2015; Zschornack, 2007). This can be a disadvantage of x-ray tubes, or, in other cases, of great advantage, such as when a large flux is needed at a specific energy. Tube-based DEI systems are under development that exploit the high intensity emission lines of x-ray tubes at very specific energies (Muehleman et al., 2010; Parham et al., 2009). Because only a specific bandwidth of energy interrogates the sample in DEI, the flux spikes characteristic of x-ray tube spectrums lend themselves to use in DEI, as most of the energy spectrum is filtered out by the monochromator. If the energy of an emission line is chosen as the imaging energy, flux is greatly increased over other points in the energy spectrum. Exploitation of these emission lines seems key in using x-ray tubes for DEI as will be explained further in the section "Diffraction Enhanced Imaging".

Synchrotron Radiation

In contrast to x-ray tubes, synchrotrons produce radiation by *centripetally* accelerating charges (i.e. moving them through a curve) using magnetic fields (Wiedemann, 2003). At the CLS, an electron gun produces an electron beam which is accelerated in bunches by radio frequency waves in the linear accelerator (CLS, 2015). Once these electrons have been accelerated through the length of the linear accelerator to an energy of 300MeV, they are fed into the booster ring, which is the inner ring at the CLS. In this booster ring, each electron bunch is brought up to its final speed through use of a large radio frequency cavity (from 300MeV to 2.9GeV or 2900MeV), and directed and focused using several sets of magnets placed through the ring. In this ring, the energy of the electron bunches is "ramped" synchronously with the magnetic field strength of the bending magnets to maintain the same orbit through the ramping procedures. This synchronous ramping type of accelerator is termed a synchrotron. After reaching final speed, the electrons are finally injected into the storage ring, where they continue to orbit, directed by magnetic fields, their speed maintained by yet another radio frequency cavity within the storage ring. At each bend in the storage ring, the electrons are centripetally accelerated by a very strong magnetic field (1.354 T). This acceleration of the electrons produces a shower of radiation (Figure 3). However, unlike the bremsstrahlung of x-ray tubes, this radiation comes out within a very small vertical angle, and is spread horizontally through the angle of the curve; at the CLS each bend magnet of the 24 magnet sets sweeps the beam horizontally through 15^{o} of arc. The strength of the magnetic field and the electron beam energy define a characteristic broad banded spectrum that typically peaks in intensity in the x-ray range. A metric of the spectrum is the critical energy which

defines the half-power point in the energy spectrum; one-half of the radiated power is below this energy and one-half is above. It also is close to the spectral peak of the radiation. At the CLS, the combination of the 2.9GeV ring energy and 1.354T bend magnet field sets the critical energy at 7. 57keV (Christensen, Chapman, & Sidhu, 2005). The research described in this thesis was performed at the BioMedical Imaging and Therapy beamline of the CLS, on the bending magnet line (05B1-1). Experimentation on this line focuses on skeletal imaging, much of which is performed using DEI (Cooper et al., 2011).

A section of this beam is selected (typically a few milliradians of angle horizontally) and directed down a series of optical elements where it is prepared and finally used in experimentation. These optical elements (filters, apertures, windows, monochromators, shutters and ancillary equipment) in combination with shielding enclosures (hutches) form what is called a "beamline". In the case described with a bend magnet as a source of synchrotron radiation, the beamline would be called a "bend magnet beamline".

This type of radiation production has several benefits. Synchrotron radiation is:

- brighter than tube sources (~10^6 times)
- continuously tunable from infrared to hard x-rays
- naturally collimated or directed
- polarized
- pulsed

Third generation synchrotrons such as the CLS also produce highly directed radiation beams using insertion devices such as wigglers and undulators placed between the ring's bend

magnets (Figures 3 and 4). Each insertion device involves a series of magnets with alternating

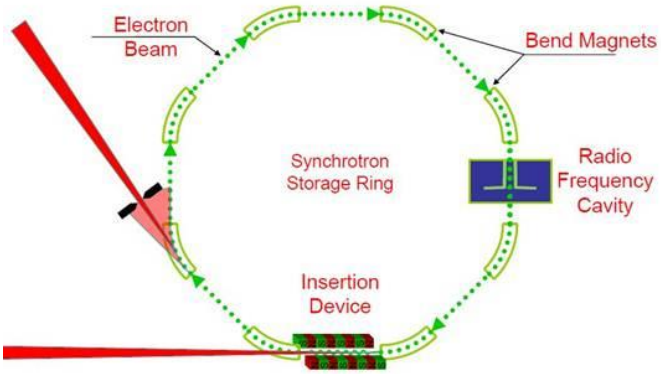

Figure 3: Overhead view of a third generation synchrotron. Courtesy L. Dean Chapman

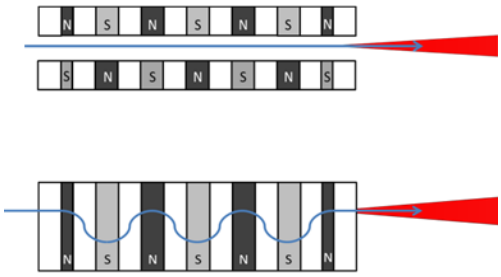

Figure 4: Side and top views of an insertion device.

fields which cause the electron beam to 'wiggle' or spiral through the magnetic field, exiting the insertion device along their original direction of travel. This series of intense accelerations produces a relatively focused beam of radiation with greater brilliance than a single bend magnet is capable of producing (Figure 5).

Synchrotron radiation has been crucial in the development of multiple image radiography (MIR) techniques such as DEI. MIR techniques use multiple images created by the same x-ray beam to capture more information about the sample than can be obtained by a single

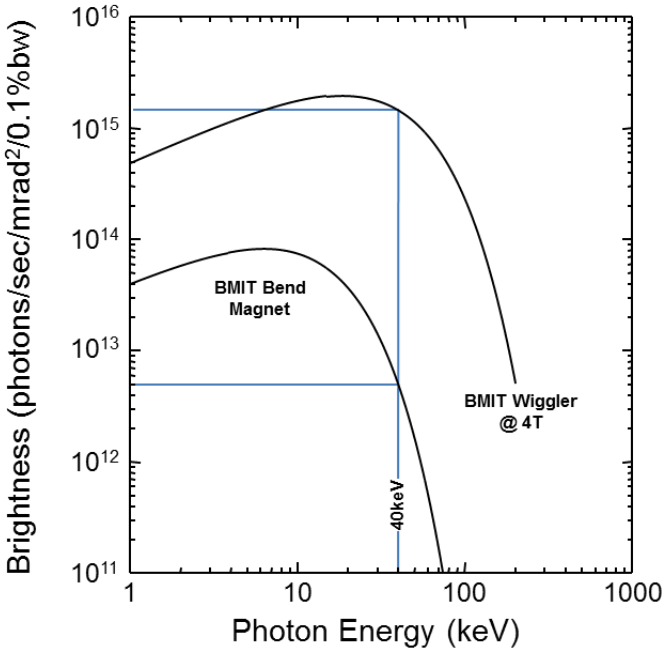

Figure 5: Comparison of the spectrum from a synchrotron bend magnet and wiggler. Note: brightness is in log scale

image (Wernick et al., 2003). DEI uses an analyzer crystal to produce two images. The refraction component of the contrast in one image is inverted compared to the other, such that processing yields both absorption and refraction information. These imaging techniques require a high level of monochromatization of the beam. The brightness and continuous tunability of the synchrotron's radiation beams tolerates this filtration of the beam much better than a tube-based system (Connor et al., 2011). Additionally, synchrotron radiation is naturally collimated, whereas much of the intensity from a tube-based system is rejected in collimating to produce a beam.

X-ray interaction with matter

Traditionally, contrast is produced through x-ray absorption by the sample. As a beam travels a distance x through a sample, intensity (I) is lost as the sample absorbs (and scatters) some of the radiation (Podgorsak, 2006). The absorption of x-rays is dependent on the linear attenuation coefficient (μ) of the sample and is described by equation 2.1

$$I(x) = I_0 e^{-\mu x}, \qquad [2.1]$$

$$where\ I = intensity, I_0 = initial\ intensity,$$
$$x = \ distance\ traveled\ through\ the\ material$$

To form an image of the attenuation of an embedded object, the contrast in attenuation of that object, i.e. the relative difference between the intensity of the beam having passed through that embedded object and that of the intensity of a portion of the beam passing only through the surrounding tissue (see Figure 6) is assessed.

$$I_b = I_0 e^{-\mu_b t_b} \quad \text{(surrounding tissue)} \qquad [2.2]$$

$$I_f = I_0 e^{-\mu_b (t_b - t_f)} e^{-\mu_f t_f} = I_0 e^{-\mu_b t_b} e^{-(\mu_f - \mu_b) t_f} \quad \text{(embedded object)} \qquad [2.3]$$

The relative difference between these two intensities is the contrast (C),

$$C = \frac{I_b - I_f}{I_b} = 1 - e^{-(\mu_f - \mu_b) t_f}, \qquad [2.4]$$

While the thickness of the embedded object is fixed, equations 2.2-2.4 show that the attenuation coefficient is energy dependent, meaning it can be adjusted by changing the imaging energy (see Figure 7). The weak contrast limit of equation 2.4 (where contrast increase is most needed),

$(\mu_f - \mu_b) t_f \ll 1$, is,

$$C \cong (\mu_f - \mu_b) t_f \, . \qquad [2.5]$$

To maximize contrast by absorption, energies should be selected that maximize the difference in attenuation coefficients, but still provide enough transmitted intensity to produce a good contrast-to-noise ratio (CNR). Since contrast relies on the attenuation coefficient of the sample material, materials with much

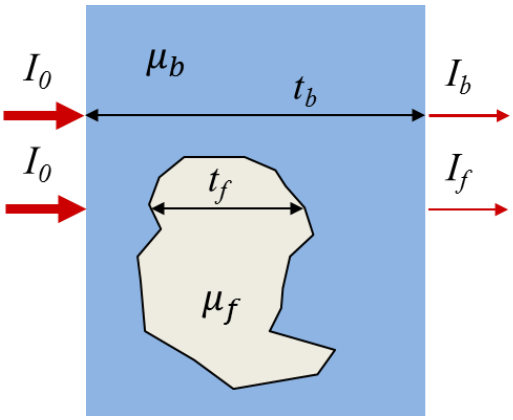

Figure 6: Two portions of a beam, one passing through tissue of constant attenuation, and one passing through an embedded object in that tissue. Courtesy L. Dean Chapman

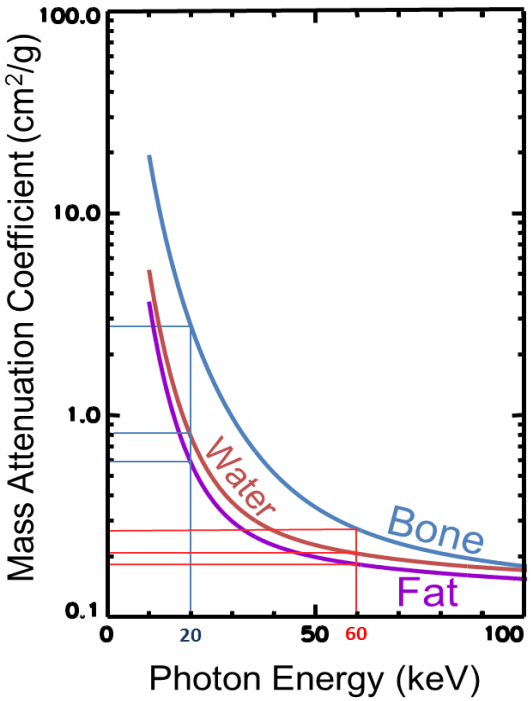

Figure 7: Attenuation of x-rays by various biological substances, relative to energy of photons.

different attenuation coefficients (e.g. bone and soft tissue) provide high contrast; however, if two materials have similar attenuation coefficients (e.g. cartilage, ligaments, muscle, skin, water, bodily fluids), contrast will be much lower. Another drawback to using x-ray absorption to produce contrast is that it inevitably ties visibility of contrast to absorbed dose by the sample. Contrast to noise is increased by increasing absorbed dose; decreasing absorbed dose compromises contrast.

X-ray attenuation in matter in the x-ray diagnostic energy regime (~20keV to 100keV) is dominated by three fundamental x-ray loss mechanisms: photo-electric absorption, coherent scattering and Compton scattering. Photo-electric absorption results in a complete absorption of a photon and subsequent ejection of a bound electron. Coherent scattering is an elastic process where a photon interacting with an electron is scattered into another direction with the same energy; this is the basis of the diffraction process in crystals described later. Compton scattering is an in-elastic scattering process where a photon is scattered by an electron and the scatter photon is at a lower energy than the incoming photon and the electron carries away some of the energy. As seen in Figure 8, these interactions are labeled as the components making up the "imaginary" part of the refractive index. Refraction is the

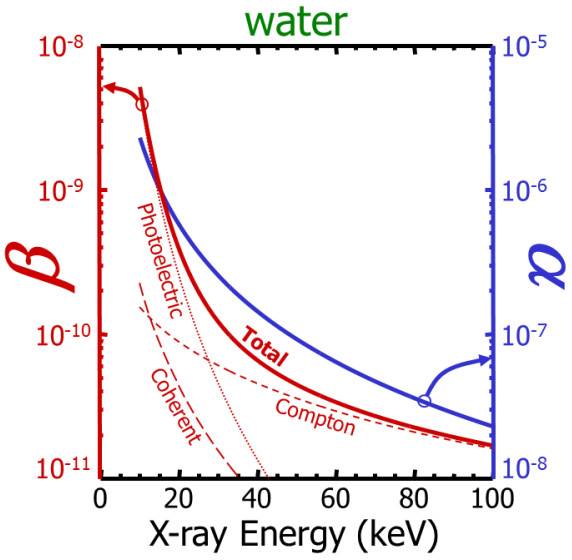

Figure 8: Real (refraction) and imaginary (absorption) parts of the refractive index, n, relative to x-ray energy. Note scales of α and β; α is three orders of magnitude larger than β.

"real" part of the index and absorption makes up the "imaginary" part.

For most materials making up biological tissues, the photo-electric absorption and Compton scattering dominate the attenuation process. For soft tissue at energies below ~30keV photo-electric absorption will dominate and for energies above, Compton scattering will dominate. The fact that Compton scattering results in a number of photons with widely varying angles creates a problem for most x-ray diagnostic imaging procedures since these photons no longer carry projection position information. They create a background "fog" in a conventional absorption image and results in the need for anti-scatter grids used pervasively in all clinical x-ray imaging procedures.

X-rays can also interact with matter by refraction. Refraction is the 'bending' of x-rays as they pass between two materials with different refractive indices, n. Refraction is dependent on these refractive indices, as well as the angle of incidence of the x-ray beam, θ, according to Snell's law:

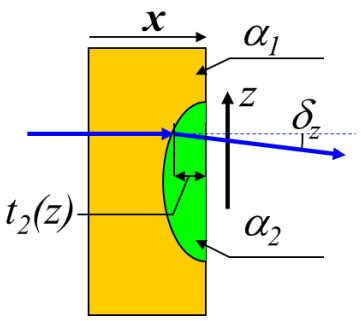

Figure 9: X-ray refraction from an embedded object. The feature is of lower density than the background material.

$$\frac{\sin\theta_1}{\sin\theta_2} = \frac{n_2}{n_1} = \frac{1-\alpha_2}{1-\alpha_1} \qquad [2.6]$$

where the angles, θ_1 and θ_2, are measured with respect to the surface normal in the two media, respectively (Figure 9). For x-rays the difference between the two angles, θ_1 and θ_2, is very small since both n_1 and n_2 are very close to 1, typically differing from 1 by 10^{-6} or smaller. The deviation angle, $\delta_z = \theta_2 - \theta_1$, can be shown to be approximately,

$$\delta_z = (\alpha_1 - \alpha_2)\frac{\partial t_2(z)}{\partial z} \qquad [2.7]$$

$$where\ \alpha_i = \frac{r_e \lambda^2 F_{0i}}{2\pi V_c} \approx \frac{r_e \lambda^2}{4\pi u} \rho_i\ , \qquad [2.8]$$

where $\frac{\partial t_2(z)}{\partial z}$ is the thickness gradient along a direction of an embedded feature in the object being imaged, α_1 and α_2 are the real part of the refractive index corrections (see below) for the two materials (material 1 is the matrix or background material and material 2 is the embedded material), r_e is the classical electron radius (2.82x10^{-15}m), λ is the x-ray wavelength, ρ_i is the mass density of the material, u is the nucleon mass (1.67x10^{-27}kg), F_{0i} is the forward scattering factor (closely approximated by the atomic Z or electron number) and V_c is the volume in which F_{0i} is measured (the ratio of F_{0i}/V_c is the electronic density of the material). The direction, z, that appears here, is in the "diffraction" plane of the monochromator – analyzer system, perpendicular to the beam as it traverses the object. It should be noted that the x-ray wavelength, λ, and the photon quanta energy or just the photon energy, E, are related by Planck's constant, h, and the speed of light, c, via,

$$E = \frac{hc}{\lambda}, or, in\ practical\ units, E[keV] = \frac{1.24keV \cdot nm}{\lambda[nm]} \qquad [2.9]$$

Scattering and specifically, Compton scattering tends to blur an absorption based image – a problem that has led to the use of scatter rejection devices such as gratings and crystals. It was exploring the use of crystal diffraction for scatter rejection that led to the development of DEI originally[1].

Absorption and refraction can be related to each other through the refractive index, n. Specifically the refraction is the "real" part of the index and the absorption is the "imaginary" part,

[1] Personal communication, L. Dean Chapman, 2013

$$n = 1 - \alpha - i\beta. \quad \text{(see Figure 8)} \qquad [2.10]$$

The real part of the refractive index correction, α, is given by equation 2.8 and was used earlier to describe the refraction with x-rays. The absorption is characterized by β in [2.10 which is related to the linear attenuation coefficient, μ, by

$$\mu = \frac{4\pi}{\lambda}\beta. \qquad [2.11]$$

X-ray absorption contrast has been used for medical imaging since shortly after the discovery of x-rays. Equation 2.4, examined earlier, captures the contrast mechanism exploited. Highly absorbing materials such as bone and metals provided good contrast, and the basic principles of this type of imaging have continued to be the primary tool for imaging bone.

X-ray Diffraction

The x-ray interaction with crystals is dominated by diffraction. Reflection of x-rays off crystal lattice planes causes constructive interference, producing a very high reflected intensity when certain conditions are met, and negligible intensity otherwise (Friedrich, Knipping, & Laue, 1912). Any beam not satisfying these conditions passes through the crystal or is absorbed thereby. Bragg's Law (Bragg & Bragg, 1913) gives the conditions for diffraction:

$$n\lambda = p_1 + p_2\,, \qquad or$$

$$\lambda = 2d_{hkl}\sin\theta \qquad [2.12], \text{ see Figure 10}$$

where p is the difference in distance traveled by rays intercepting two lattice planes, λ is the wavelength of the rays, d_{hkl} is the lattice spacing and θ is the angle of incidence with the lattice planes. *n* is an integer.

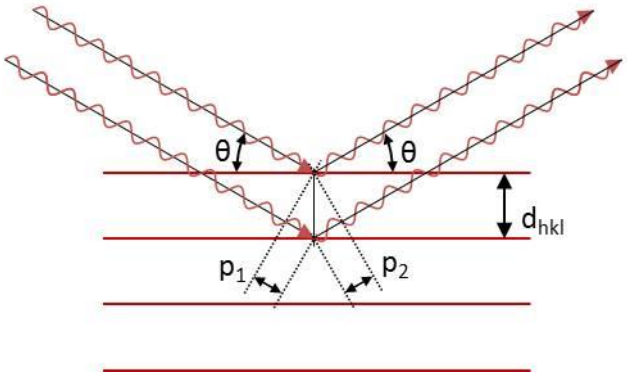

Figure 10: Diagram of two rays satisfying the conditions of Bragg's Law.

Diffraction is commonly used to select a spectral portion of the beam. Bragg's Law ties wavelength (λ), and, therefore, energy, to incident angle. That means the energy that is diffracted by the crystal can be changed simply by adjusting the incident angle of the beam (θ), i.e. rotating the crystal. The connection between wavelength and angle in Bragg's law is shown in Figure 11. Filtering the beam in this way is called monochromatization, and produces a near rectangular range of energies or wavelengths. The energy bandwidth can be predicted for the types of crystals used for the monochromators and analyzers for imaging, especially at a synchrotron. The crystals that are used are highly perfect with no dislocations or faults. These types of crystals are now common based on the needs of the semiconductor industry. Single crystal silicon is readily available and is the material of choice for many synchrotron applications due to its good thermal,

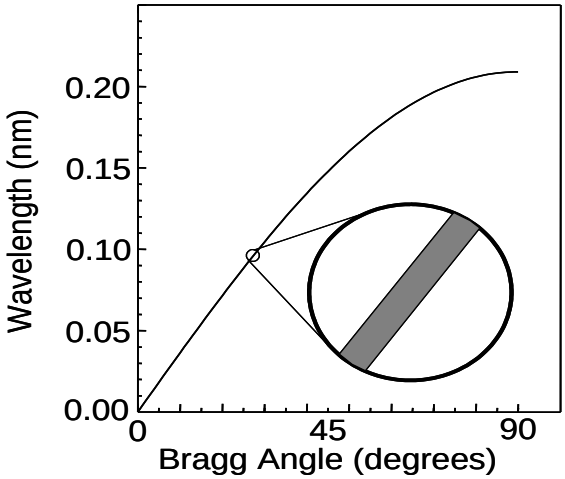

Figure 11: Wavelength versus angle for a crystal defined by Bragg's Law. The inset shows a magnified section of the curve. The curve shown is for the Si (3,3,3) reflection.

mechanical and crystal perfection properties (Cullity & Stock, 2001; Hammond, 2009).

The x-ray diffraction properties of a perfect crystal are described by the "dynamical theory" of diffraction. This approach accounts fully for the interference of the incident x-ray beam with the diffracted beam(s) within the crystal. One approach is to calculate the interaction of an incident plane wave on a crystal represented as a periodic array of polarizable material (Authier, 2004; Zachariasen, 1945). The result is a prediction of the reflectivity of the plane wave as the Bragg condition is traversed in angle. An example of this reflectivity curve is shown in Figure 12.

At the BioMedical Imaging and Therapy beamline (BMIT), a double crystal monochromator is used in which the beam is diffracted by two very near parallel crystals, such that both crystals select essentially the same energy bandwidths.

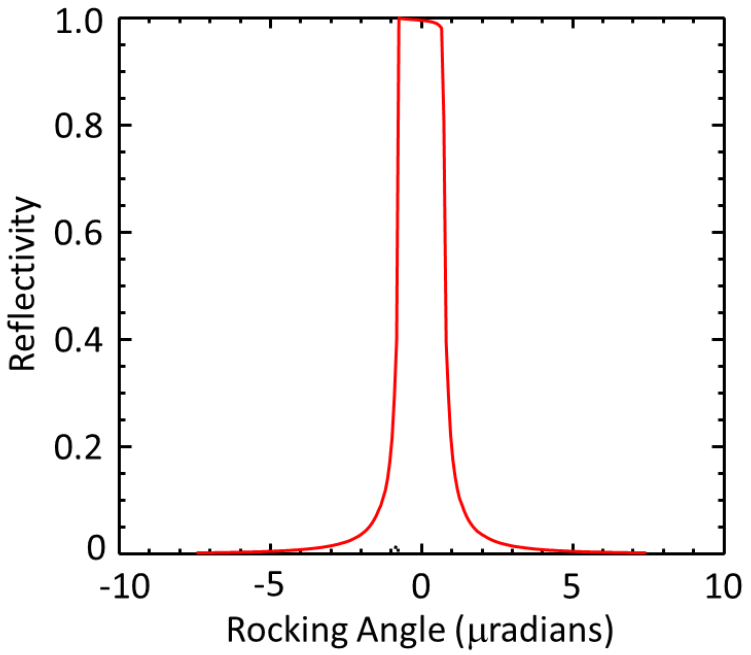

Figure 12: Plane wave reflectivity curve for the silicon (4,4,0) type reflection at 40keV.

Diffraction Enhanced Imaging

While conventional x-ray radiography relies on the attenuation of x-rays by the sample to produce contrast, DEI exploits both the absorption of x-rays by the sample, as well as the

amount of refraction experienced by x-rays as they pass through the sample (Chapman et al., 1997). DEI provides secondary extinction and refraction information through the use of a Bragg analyzer crystal placed between the sample and the detector to reflect a narrow bandwidth of the sample-filtered beam onto the detector. In a synchrotron facility, a monochromatic beam is created by passing the white beam through a double crystal monochromator, selecting a narrow energy bandwidth. This filtered beam interrogates the sample, and then is reflected through what is effectively another monochromator, a single crystal monochromator, called a Bragg analyzer crystal, or, simply, analyzer crystal (Figure 13). Any scatter by the sample changes the beam's angle of incidence with the analyzer crystal. If this angle change is great enough to place the angle of incidence outside of the crystal reflectivity width, it is not

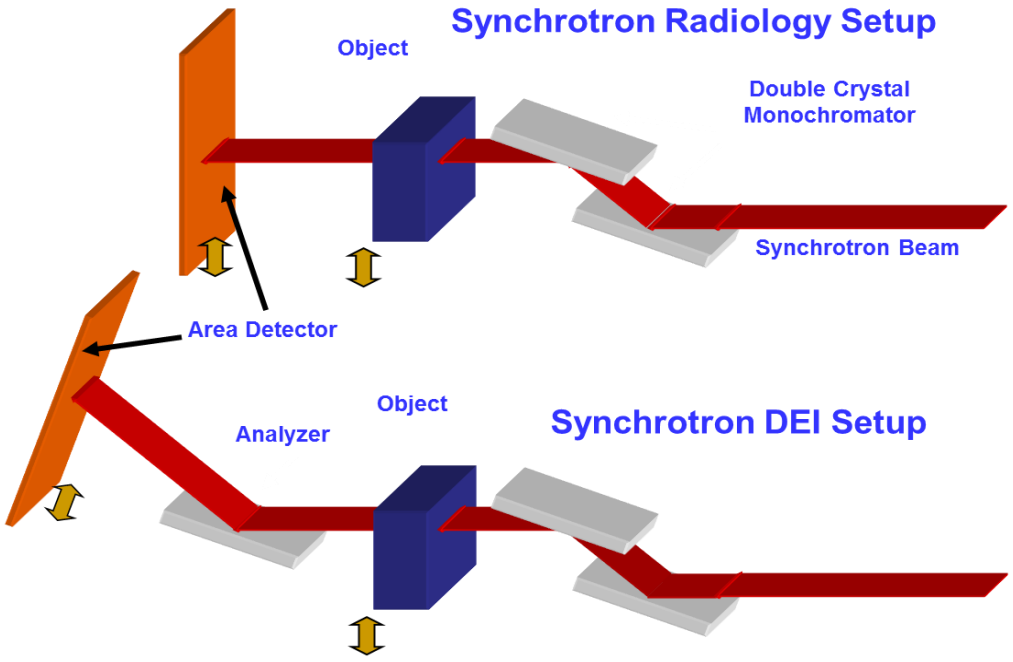

Figure 13: Schematic setup of the radiology (upper figure) and DEI as implemented at a synchrotron. The beam is prepared by a double crystal monochromator, and passed through the object. In the radiology setup it is detected, however in the DEI setup, the beam is then reflected by an analyser crystal prior to detection.

reflected by the analyzer onto the detector. Therefore, this setup provides a form of scatter rejection that is as sensitive as the energy bandwidth of the crystal reflection being exploited, viz. secondary extinction contrast. Additionally, as the angle of the analyzer crystal is adjusted, the reflectivities of the monochromator crystals are convolved with that of the analyzer crystal with respect to angle. The angular overlap between the double crystal monochromator and the analyzer crystal creates an intensity 'spike' as the angle of the analyzer crystal matches that of the monochromator. This 'spike' is basically the angular convolution of two near-rectangular reflectivity functions, forming a triangular "rocking curve" (Zhong, Thomlinson, Chapman, & Sayers, 2000). This effect is shown in Figure 14. The angular width of these rectangular reflectivity curves is a "Darwin width" (Als-Nielsen & McMorrow, 2011). Because of the wings of the crystal reflection we are exploiting, this 'triangular' rocking curve actually has a rounded peak at maximum reflectivity and 'tails' as it approaches zero reflectivity (Figure 15). It has an idealized full width of the sum of the Darwin width of the monochromator crystal and the

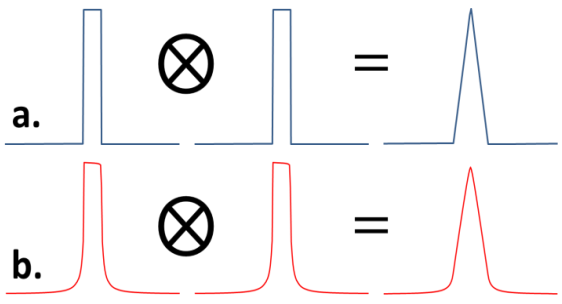

Figure 14: Convolution of two reflectivity curves to give the rocking curve observed when two crystals are "rocked" against one another. Figure a shows the idealized case of two rectangular reflectivity curves give a triangular rocking curve. Figure b shows the actual rocking curve for Si (4,4,0) at 40keV.

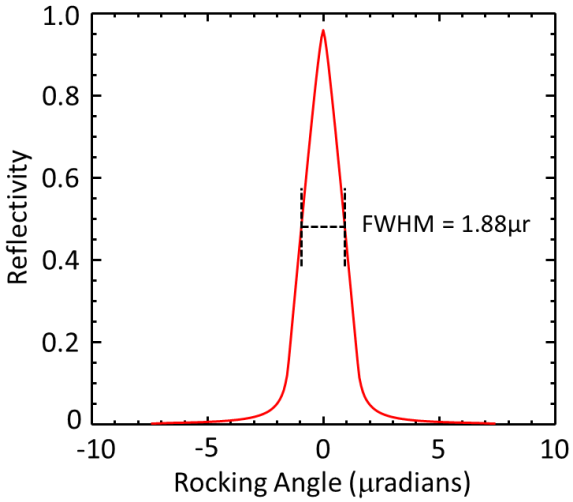

Figure 15: Rocking curve for Si (4,4,0) at 40keV. The full width at half maximum is shown as 1.88 microradians, the Darwin width is 1.49 microradians.

analyzer crystal at the imaging energy, and an ideal maximum reflectivity of 1. By adjusting the orientation of the analyzer crystal imaging can be performed at any point along this curve. If analyzer crystal orientation is adjusted to the peak of the rocking curve and an image of the sample is taken, that image will provide absorption information, but any x-rays scattered by the sample by more than the width of the rocking curve will be filtered out by the analyzer crystal, i.e. secondary extinction contrast. In addition, parts of the beam that experience refraction will meet the analyzer crystal at an altered angle, moving to one side or the other of the rocking curve peak, and dropping in intensity. At the peak, then, a single image with both absorption and refraction information exists.

However, if the orientation of the analyzer crystal is adjusted such that it sits on the side of the rocking curve, at, say, 50% reflectivity, the image obtained will still contain absorption information with secondary extinction, but will now show refraction in one direction as a brighter spot on the image, and refraction in the other direction as a darker spot on the image, i.e., refraction in one direction moves up the rocking curve (greater reflectivity) and refraction in the other direction moves down the rocking curve (lower reflectivity), as can be seen in Figure 16. This effect is highlighted in the magnified images of the bubbles below each of the images. Setting the analyzer crystal to the same reflectivity on the opposite side of the rocking curve yields an image with exactly the same absorption information as before, but with exactly the opposite refraction component, i.e. the refraction that caused bright spots on the original side of the rocking curve will now produce a region of lower intensity and vice versa. Pixel-by-

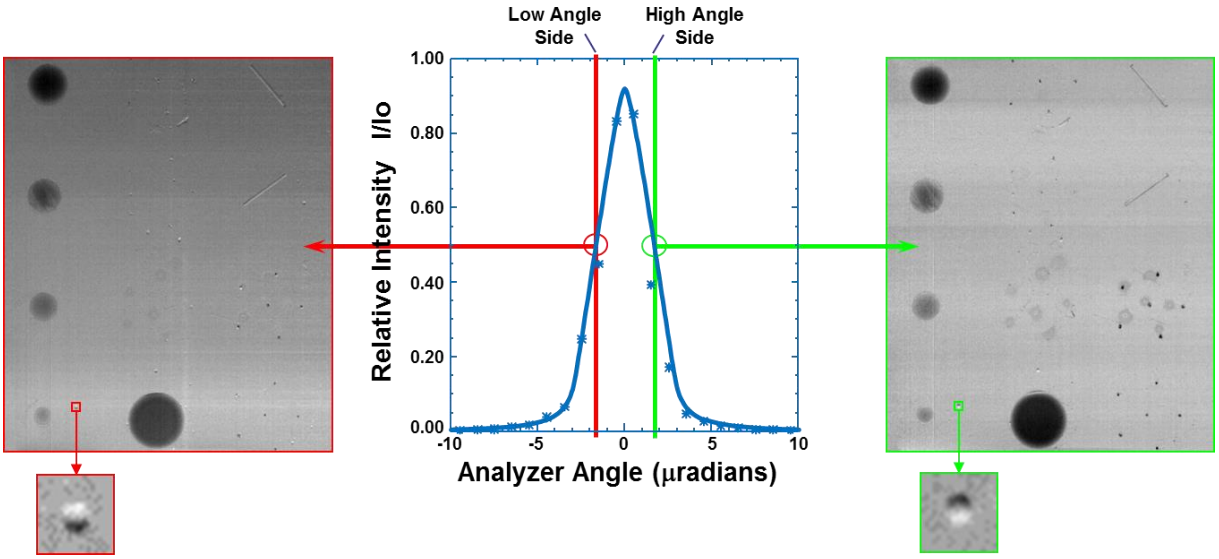

Figure 16: Showing the rocking curve produced by convolution of the energy bandwidths of the double crystal monochromator and the analyzer crystal. The images acquired at either side of the rocking curve are also shown. Courtesy L. Dean Chapman

pixel arithmetic of these images provides only the absorption or only the refraction component (Figure 17). To obtain an absorption image, the images from opposite sides of the curve are added; the refraction components cancel one another, and the absorption components constructively combine. To obtain a refraction image, the two images are subtracted; the absorption components destructively combine to eliminate all absorption information, and the refraction components constructively combine. A pure absorption image (with extreme scatter

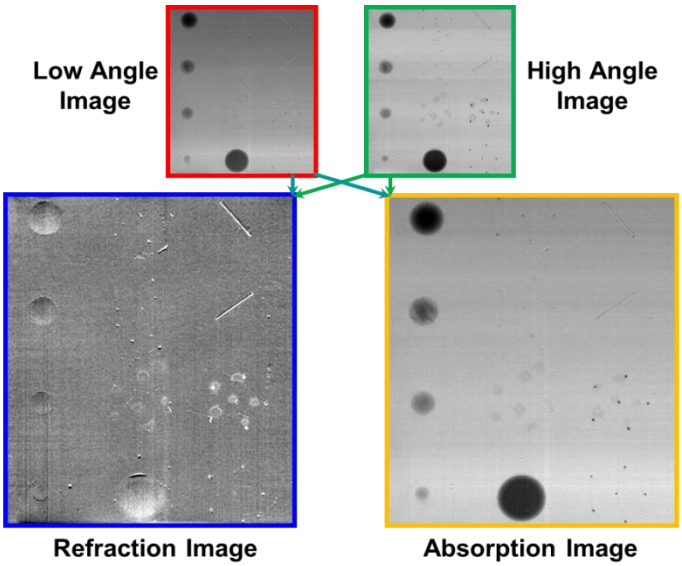

Figure 17: Pixel-by-pixel arithmetic of the images from either side of the rocking curve yield a refraction image (left) and an absorption image with secondary extinction contrast (right). Courtesy L. Dean Chapman

rejection) and a pure refraction image (Figure 17) are then created (Chapman et al., 1997). The absorption image provides more detail than available with conventional radiography because any part of the beam scattered through an angle greater than about one Darwin width (a few microradians in this case) by the sample is not reflected on to the detector by the analyzer crystal. The increase in contrast over conventional radiographs by DEI absorption images is shown in Figure 18.

Figure 18: Conventional x-ray image of a mouse (left) and DEI absorption image (right) showing increased contrast from secondary extinction contrast. Courtesy L. Dean Chapman

Refraction contrast depends upon the difference in density, ρ_i, between two tissues and the angle between the incident beam and that interface, θ, according to equation 2.13 (Chapman et al., 1996)

$$\delta_z = (\alpha_1 - \alpha_2)\frac{\partial t_2(z)}{\partial z} \qquad [2.13]$$

$$where\ \alpha_i = \frac{r_e \lambda^2 F_{0i}}{2\pi V_c} \approx \frac{r_e \lambda^2}{4\pi u}\rho_i\ .$$

Where $\frac{\partial t_2(z)}{\partial z}$ is the thickness gradient along a direction of an embedded feature in the object being imaged, α_1 and α_2 are the real part of the refractive index corrections for the two

materials, r_e is the classical electron radius, λ is the x-ray wavelength, u is the nucleon mass, F_{0i} is the forward scattering factor and V_c is the volume in which F_{0i} is measured (the ratio of F_{0i}/V_c is the electronic density of the material). The direction, z, that appears here, is in the "diffraction" plane of the monochromator – analyzer system, perpendicular to the beam as it traverses the object. The dependence of refraction on density allows visualization of the interfaces between tissues of very similar attenuation properties, but different densities.

Secondly, absorption imaging depends directly on absorbed dose for contrast, requiring that imaging be done at energies where absorbed dose to the sample is high, for the best contrast. Refraction contrast, on the other hand, measures the deviation in the direction of the *transmitted* beam. This refraction is relatively unaffected by beam energy, allowing imaging at higher energies, and, therefore, lower absorbed dose, without significantly decreased contrast (Bravin, Fiedler, & Thomlinson, 2002). Now, equation 2.13 above indicates that refraction of the beam has a λ^2 dependence, meaning increased beam energy yields reduced refraction. However, the Darwin width of the reflected beam is approximately linearly dependent on wavelength, yielding a narrower rocking curve with increased beam energy. This translates to an increase in refraction sensitivity approximately proportional to λ or $1/E$. The combination of these phenomena makes refraction images significantly less adversely affected by an increase in imaging energy than absorption images (Hasnah et al., 2005). Thirdly, this freedom in choosing the imaging energy allows imaging of thicker samples more efficiently than was previously possible. Using higher energy x-rays provides more penetration through the sample, yielding greater relative beam intensity (I/I_0) (Parham et al., 2009). Less intensity is lost due to absorption,

$$I(x) = I_0 e^{-\mu x}, where\ \mu = \frac{4\pi}{\lambda}\beta, \quad [2.14]$$

because the energy has increased (wavelength has decreased), yielding a smaller attenuation coefficient (μ). This combination of advantages is summarized in Figure 19, showing drastically increased soft tissue contrast with around 35 times less exposure compared with conventional absorption imaging. Decreased dose is due largely to higher imaging energy.

Perhaps the greatest limitation to DEI is the narrow energy bandwidth of x-rays used. The brightness of synchrotron light provides sufficient flux even when the beam is heavily filtered by monochromatization. However, synchrotron facilities are large and expensive, on a scale that practically prohibits their use for clinical imaging. Using x-ray tubes as a source for DEI is key for its clinical application, but their brightness is much lower than that of synchrotron sources. The spectrum of x-ray tubes contain spikes at certain energies called emission lines, which reflect the material of the anode. These emission lines of x-ray tubes offer increased brightness at set energies. If these are aligned with imaging energies in such a way as to exploit the increased brightness, tubes become a viable source for DEI. Non-synchrotron systems have been tested which may allow clinical use of this technology (Faulconer et al., 2009; Faulconer, Pisano, & UNC Biomed. Eng., 2009; Fogarty, Reinhart, Tzvetkov, Nesch, & Williams, 2011; Nesch et al., 2009).

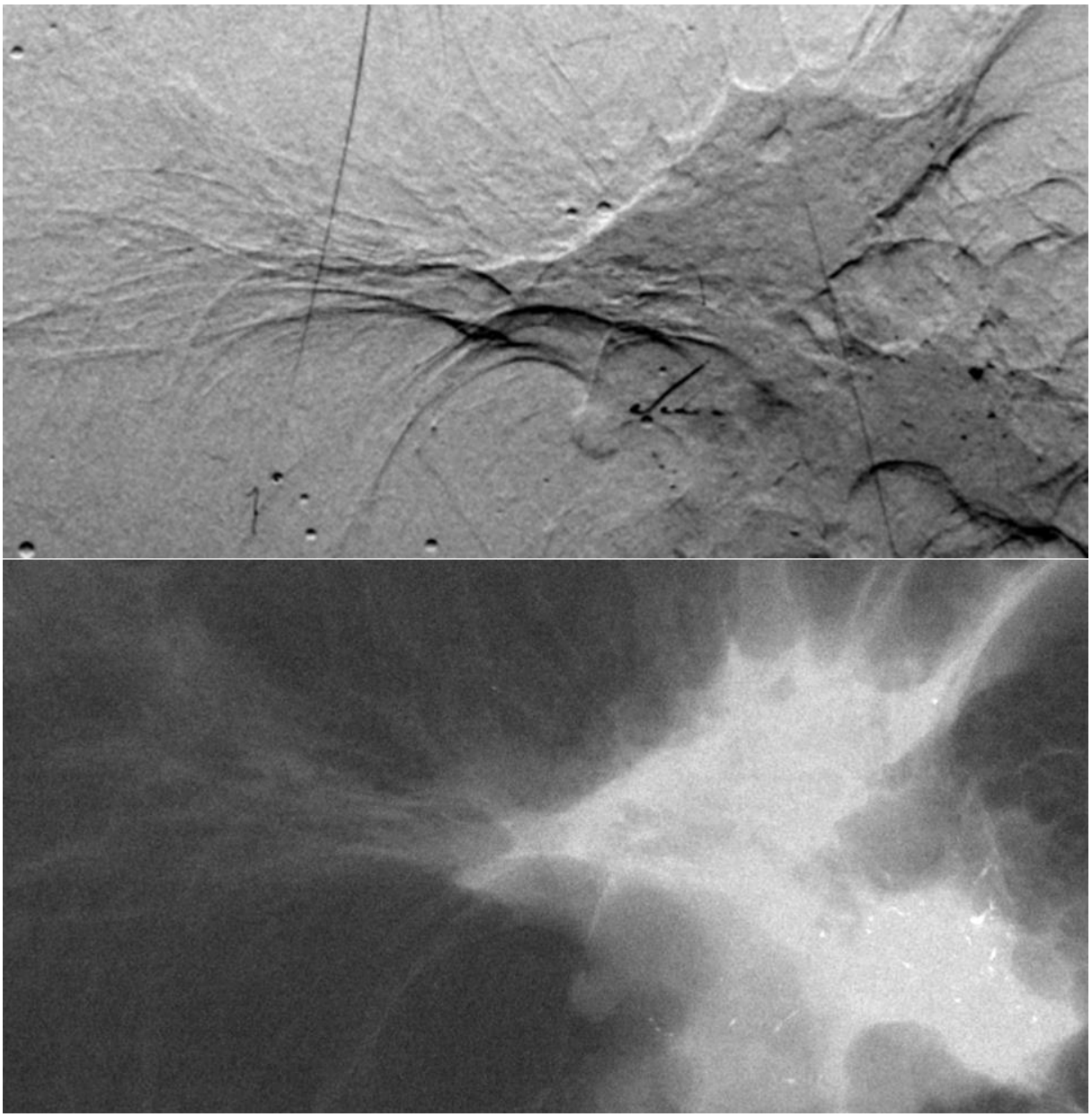

Figure 19: DEI refraction image of excised breast tissue tumor (top) taken at 40 keV and 20 mrad, and conventional absorption image (bottom) of the same portion of tissue taken at 18keV and 700mrad. Courtesy L. Dean Chapman

CHAPTER 3: PLANAR DIFFRACTION ENHANCED IMAGING FOR JOINTS

Introduction

DEI is sensitive to soft tissues, providing images of both high resolution and cartilage contrast. The objective of the planar DEI experiments was to determine if DEI could effectively visualize soft tissues in an intact joint, and the level of interference caused by superimposition of features outside the joint space.

Diffraction of x-rays by a perfect crystal lattice allows refraction of a monochromatic beam by the sample to be calculated at each pixel. This does require two scans. However, DEI is still able to be performed at a lower dose than conventional radiography due to higher imaging energies, resulting in lower absorbed dose by the sample (Chapman et al., 1997). A pure refraction image *and* a pure absorption image (with extreme scatter rejection) are created with the same two scans.

Literary Review

As mentioned earlier, a common way of using x-ray absorption images to determine soft tissues within joints is to monitor the change in the space between the bones. As this space is reduced, it can be inferred that cartilage is degrading, thereby allowing a rough assessment of soft tissue condition using contrast derived from the bones. This provides some information about cartilage condition, but it is quite limited for investigating the mechanisms of cartilage

degeneration. While soft tissue is somewhat visible in traditional x-ray images, the contrast is far too low to analyze cartilage details or monitor cartilage condition directly. Typically, the onset of arthritis comes long before x-ray absorption images show any irregularities, which limits the usefulness of absorption radiography for diagnosis.

While soft tissues provide less contrast, x-ray absorption imaging still provides enough contrast in some soft tissues to be valuable. Investigation of conditions including cardiac disease, pneumonia, tuberculosis and other lung diseases rely heavily on chest radiographs, although diagnosis of diseases often requires other techniques (Cecil, 2012). In joints, radiography is generally used to visualize bone structures directly and the condition of other structures within the joints are inferred from the condition and position of the bone.

DEI presents a great advantage in the imaging of cartilage. Single lesions within cartilage have been visualized within intact joints (Muehleman et al., 2003; Muehleman, Li, & Zhong, 2006) which promises a much earlier diagnosis of joint diseases, as well as greatly improved insight into disease onset, progression, and remission after treatment. This represents a great improvement over diagnosis by x-ray absorption which requires serious loss of cartilage, and monitoring of cartilage condition which is done indirectly.

Further to this, the structural orientation in human articular cartilage has also been demonstrated with DEI (Muehleman et al., 2004). Not only is cartilage edge detail now perceptible with x-rays, but cartilage structures may be visualized. The research of Muehleman and colleagues represents the first detection of cartilage structure using radiography and the diffraction enhanced images confirmed previous models of collagen fiber bundle arrangements. It has also been shown that ligaments and tendons may be visualized in high contrast using DEI

(Li et al., 2004), which, while not directly applicable to research into cartilage degeneration, underscore the value of DEI for general joint condition diagnosis. Patient diagnosis by DEI is largely dependent on the development of clinical DEI systems. Synchrotron sources are practically cost prohibitive for patient diagnosis, and principally reserved for research use. Recently the development of non-synchrotron DEI systems has been researched.

In-laboratory DEI systems (independent of synchrotron sources) have been explored, specifically for detecting cartilage damage *ex vivo*, and shown to be effective for visualization of early stages of cartilage degeneration (Muehleman et al., 2010). These systems represent the possibility of implementing DEI for joint imaging in a clinical setting, and have already been used for imaging cadaveric human joints (Muehleman et al., 2009). Joints imaged included normal and degenerated human tali, knee, and thumb. The results showed that DEI, fed by an x-ray tube source, is capable of visualizing cartilage degeneration. Tendons and other soft tissues of the thumb were also visualized with the laboratory DEI system.

One principle limitation that research with DEI has presented is the issue of superimposition of features. While superimposition has always presented a challenge to radiography, much of the tissue through which the x-rays were passing through produced little contrast. Bone over bone provided the largest contrast superimposition. However, in DEI, soft tissues provide significant contrast, leading to greater superimposition issues. Fatty tissue, nails, muscles, tendons, ligaments, cartilage and bone are all visible, but superimposed in DEI. Even skin and hair produce refraction that may significantly affect the image. Despite this superimposition, soft tissue detail is greatly improved using DEI over conventional radiography.

The amplification of the superimposition issue with DEI is explored further in the "Results" section.

Materials and Methods

DEI methods were applied to imaging fully intact joints of young piglets. A porcine model was chosen because porcine stifle joints are anatomically similar to human knees, and because pigs grow quickly, reaching skeletal maturity in six months, allowing for the study of normal growth patterns in this amount of time. Additionally, lameness in pigs is common due to pathologies including osteochondritis dessicans and infectious arthritis, which provides naturally occurring models of joint disease (Jackson & Cockcroft, 2007). Also, growing porcine stifle joints have diameters on the same scale as human children, providing a clinically relevant model, in terms of size (a major consideration in terms of resolution and imaging time). Image joints were obtained from 4 week old piglets as the growth plate at this stage of development has not fused, but ossification centers have developed to the point that the full joint space and some trabecular bone within the ossification centers still fit in the vertical beam size, i.e. once transferred to DEI-CT technology, one CT dataset allows visualization of joint structures including trabecular and cortical bone, epiphyseal cartilage, and ligaments, as well as surrounding muscle and soft tissue. Additionally, 4 week old samples were an ideal size for the field of view of the 18.7 μm pixel size Photonic Science detector (model: VDI VHR-90, GSO scintillator) which previous DEI experiments had proven an excellent detector for these kinds of experiments. Ethics approval was obtained from the University of Saskatchewan. Samples were generally prepared by the following process: a healthy piglet was selected based on age

by the Vaccine and Infectious Disease Organization, University of Saskatchewan, and euthanized a few hours prior to the beginning of the imaging experiments. Rear legs were excised at the hip. Samples were transported to BMIT, at the CLS, in plastic bags, and shaven. They were then mounted in a holder for DEI, and scanned. Afterwards samples were generally frozen, preserved for later reference and additional information if needed.

Setup for DEI involves standard preparation of the beam through monochromatization, collimation, and filtration; placement and alignment of the analyzer crystal/detector setup; and preparation and placement of the sample for imaging.

Preparation of the beam was the same for each of the DEI and DEI-CT experiments (described next chapter). Si (2,2,0) reflection was used for the monochromator. The monochromator was set to 20 keV, according to Bragg's Law (equation 2.12). Selecting the 20 keV energy also allows its harmonics to pass through the monochromator. These include 40 keV, 60 keV, etc. in decreasing intensities. Use of a 0.221mm aluminum filter and a 0.276mm copper filter removed most of the 20keV beam leaving the higher order harmonics, primarily a 40 keV beam. A slight detuning of the monochromator eliminated much of the harmonics above 40 keV.

Placement and alignment of the analyzer and detector was performed with the use of a small screen which fluoresces under x-ray exposure (viz. fluorescent screen). A camera focused on the fluorescent screen allowed visualization of the beam from outside of the imaging hutch. In DEI imaging setups at BMIT, the analyzer crystal is placed in the beam downstream from the sample, mounted atop a granite stand to reduce vibrations, and set to approximately the same angle as the monochromator crystals. Orientation of the analyzer is refined with piezoelectric

controls. As the angular orientation of the analyzer matches that of the monochromator, a bright streak is seen on the fluorescent screen. The detector is placed in line with this image of the beam on the fluorescent screen. If the horizontal alignment of the crystal is off, the streak will seem to flash from left to right, or right to left across the screen. Once horizontal alignment is obtained, the image of the beam will appear and disappear uniformly across the beam dimensions as the analyzer crystal crosses the angular orientation of the monochromators. After this angular orientation and horizontal alignment is performed, the analyzer setup is complete, and the screen is removed. The imaging detector is used for all future analyzer orientation.

After performing the routine alignment, the analyzer was swept completely through the rocking curve, establishing the peak intensity, and then adjusted to the desired points along the curve for imaging. Imaging system layout and sample positioning system is shown in Figure 20.

Sample preparation was minimal, as a focus of these imaging experiments is clinical relevance. The sample was imaged with all surrounding tissues intact, excised at the hip, shaven, and strapped above and below the joint to a simple aluminum stand to the side of the sample as viewed from the perspective of the incoming beam (Note: Figure 20 displays the joint as positioned in the mount for DEI-CT experiments; the sample stand for projection DEI was a simple angle bracket that stood to the side of the sample.) This stand was bolted to the imaging stage, which was remotely controlled by computer program for adjustments horizontally (moving sample in and out of beam) and vertically (alignment of sample and line scan mode imaging). Additional controls such as saddle adjustments and rotation are possible on the

same imaging stage (which were later utilized for CT imaging); these are capable of fine adjustment and controlled remotely as well.

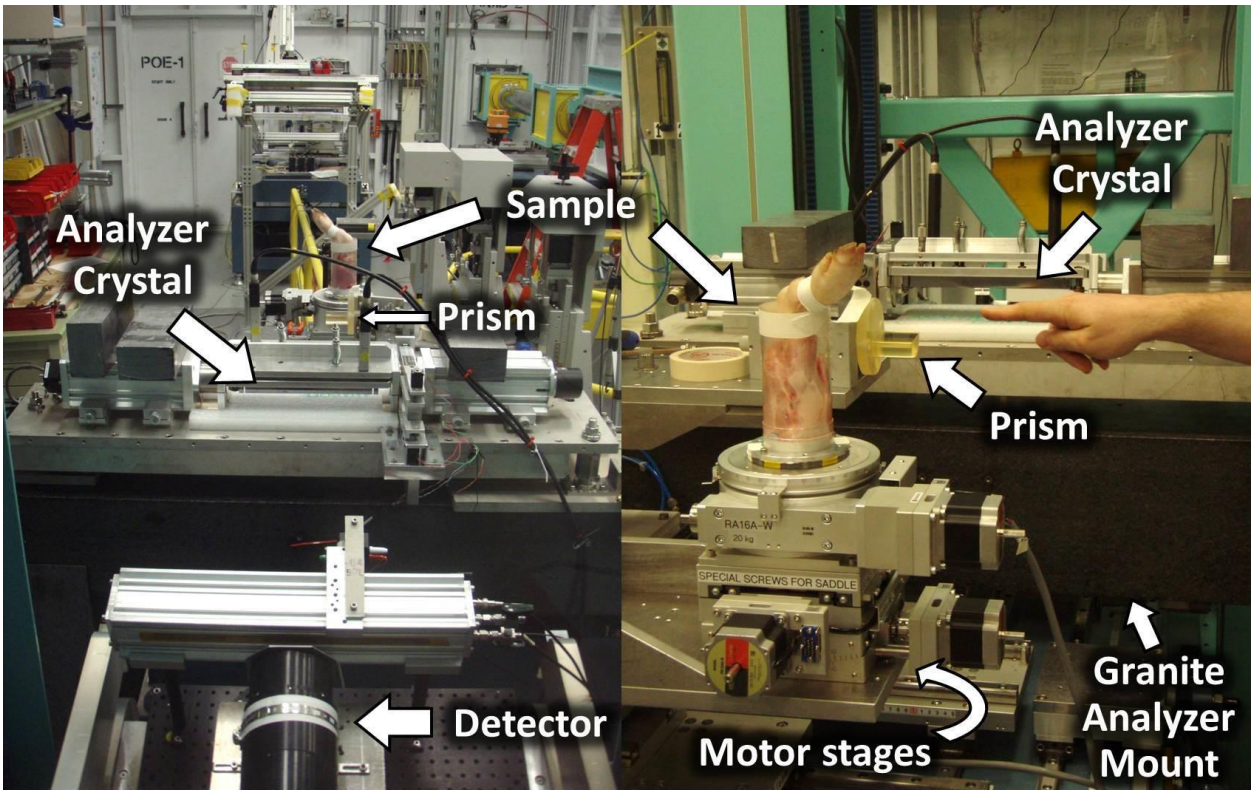

Figure 20: Two photos of the imaging setup inside the imaging hutch. Photo on left is looking upstream from the detector towards the incoming beam. Right photo is a view quartering downstream toward the analyzer crystal and detector (hidden by analyzer mount). Note: sample holder shown here is for DEI-CT experiments, not planar DEI.

Results

Images were taken at 25%, 50% and 100% reflectivity along the rocking curve. 25% and 50% images were taken on both high and low angle sides of the rocking curve, as necessary for production of refraction and absorption images. Figure 21 shows each image, and the point of the rocking curve at which it was taken. We found that soft tissue contrast was best in the refraction images from 25% of the peak intensity. Figure 22 displays the level of detail visible

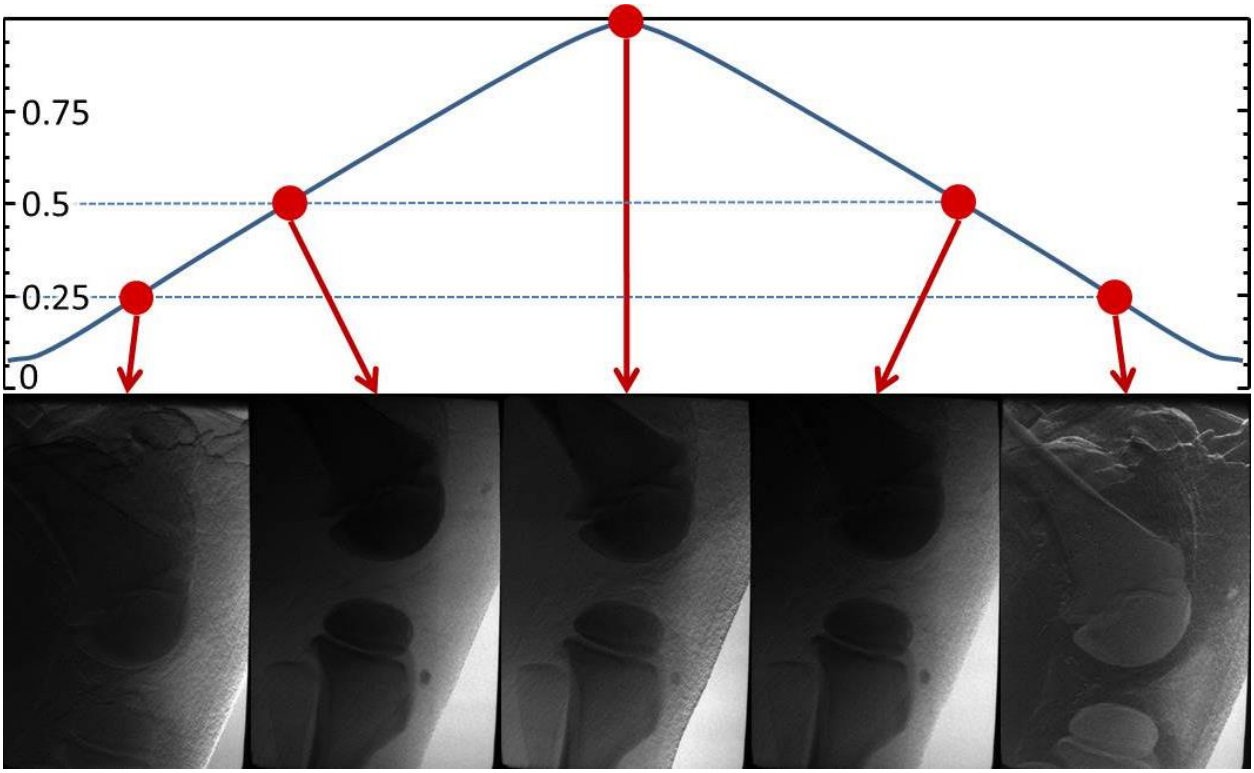

Figure 21: Images of a healthy 4 week porcine stifle joint taken at several points on the rocking curve, viz. at 25%, 50% and 100% of the peak intensity of the curve.

after image arithmetic to produce a pure refraction image compared with a traditional absorption radiograph. Cartilage edges in the refraction image are obviously producing contrast; however, nearly the entire image is overlaid with at least two contrast patterns which only serve to obscure features of interest: one from the texture of the skin surface, as the density difference between skin and air is quite high, lending itself to refraction contrast, and another from the linear nature of muscle fibers surrounding the joint. Submersing the joint in a liquid or wrapping it tightly with a smooth material might reduce the contrast from skin texture, but for fully intact imaging, there is no foreseeable way to completely eliminate these patterns in a 2D image.

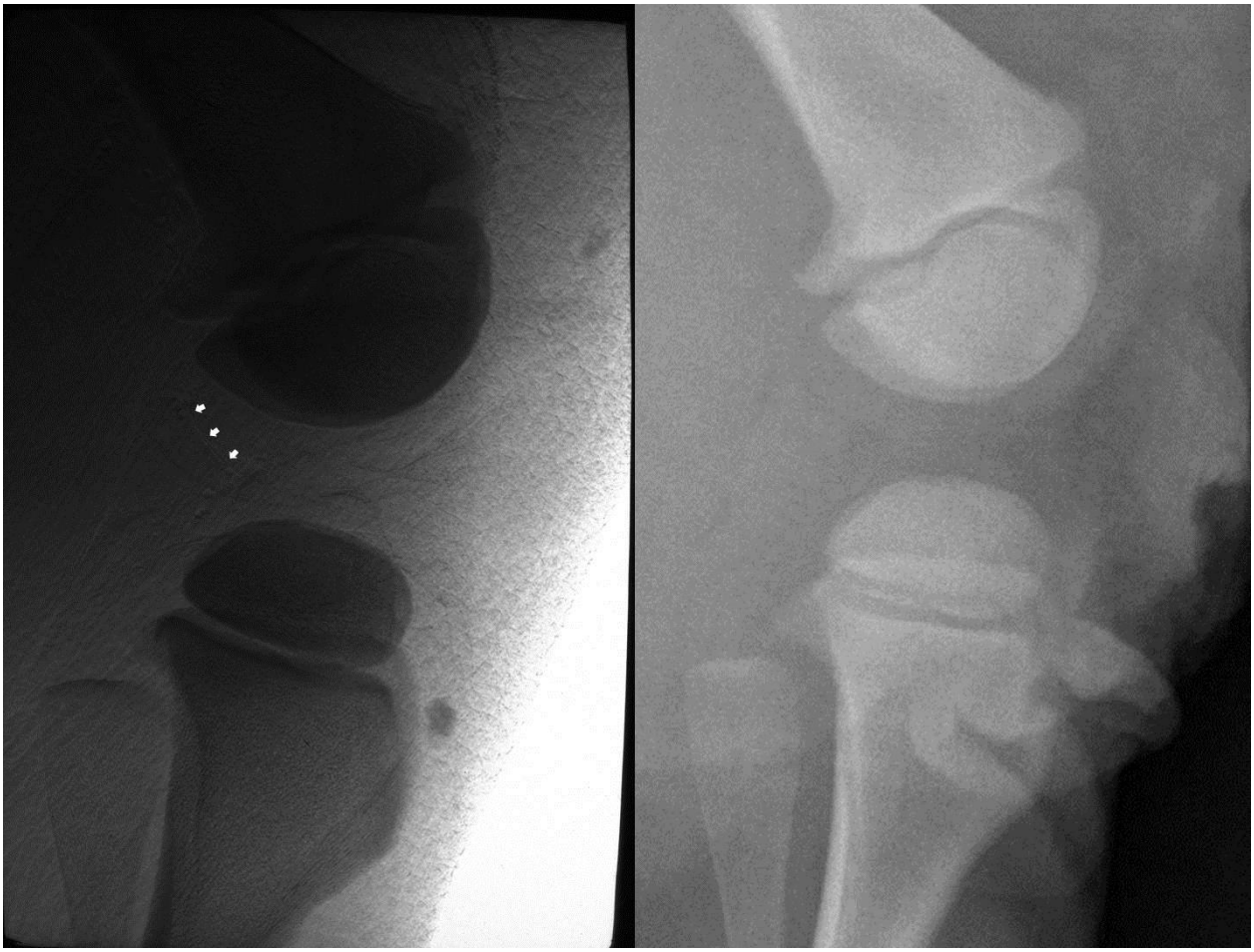

Figure 22: Sagittal DEI refraction projection (left) at 50% reflectivity of a healthy 4 week porcine stifle joint. Clinical (absorption) radiograph (right) of the same joint taken shortly after. Cartilage edge is denoted by arrows. Patella is visible anterior (right) of the tibia.

Discussion

A consideration of the imaging setup and the principles of refraction contrast may evoke a few questions concerning image interpretation. Firstly, the scale of x-ray refraction relative to pixel size is worthy of note. If x-ray refraction angles were on the same scale as visible light refraction angles, there would be serious repercussions to image interpretation. Fortunately, x-

ray refraction is orders of magnitude smaller than that of visible light. Were this not the case, a portion of the beam experiencing refraction by the sample would be moved across the detector by several pixels, such that a bright or dark spot in one part of the image would actually be the result of refraction produced by a feature in another portion of the image. As it is, x-ray refraction angles are typically on the order of nanoradians, which means that for a 1m sample-to-detector distance along the path of the beam, the refracted beam will only move in position by a few nanometers, an insignificant amount even for pixels on the micron scale.

Secondly, it may be noticed that in the setup shown (Figure 13), the analyzer crystal refracts the beam in the vertical direction, and therefore, only *vertical* refraction of the beam is converted to a change in intensity. The analyzer angle, or rocking angle, is measured vertically from the beam to the crystal plane. The result of this is that the images are sensitive to refraction only in the vertical direction. An investigation of Figures 16, 17 and 19 will reveal that the top and bottom edges of features in the sample are the ones that produce the greatest contrast, while horizontal density gradients are not reflected in the image. Figure 23 plots the reflectivity of the beam by the analyzer crystal with respect to diffraction both in (vertical) and out (horizontal) of the plane of analyzer diffraction.

Were the monochromator and analyzer crystal rotated 90° around the direction of the incoming beam, the system would be sensitive to horizontal density gradients rather than vertical (the same effect would be produced by rotating the sample about the direction of the incoming beam). This directionality of refraction images is an important consideration in image interpretation. Textures of surfaces may seem seriously distorted between images of the same sample if its position in the beam is changed dramatically. Directional features such as bone

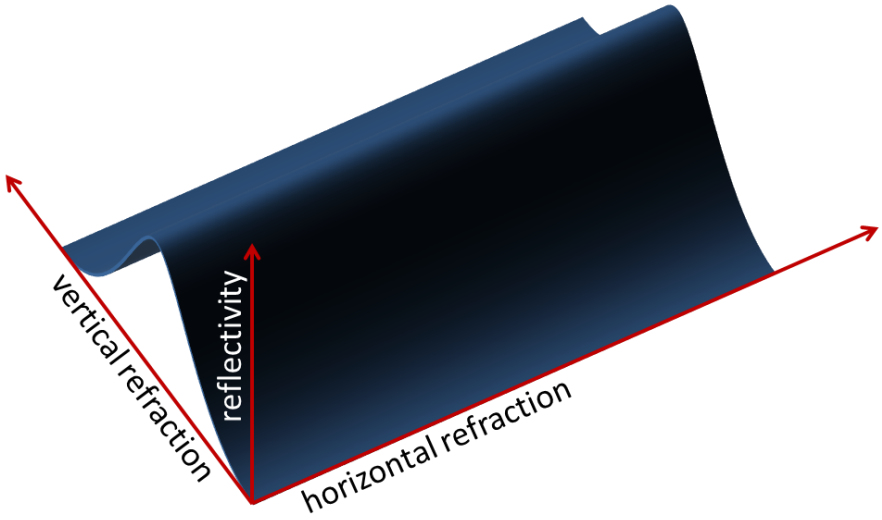

Figure 23: Plot of the analyzer crystal rocking curve for refraction in the vertical (sensitive) direction, and horizontal (nonsensitive) direction. Vertical refraction moves us up or down the curve, resulting in increased or decreased image intensity corresponding to amount of refraction in that direction. Horizontal refraction, however, with the described setup, moves us along an isoreflective surface, i.e. image intensity is not changed by horizontal refraction of the beam.

trabecularization and ligament fibers can go from the most striking features of an image to features of low contrast depending on the orientation of the sample.

Another consideration relating to the mode of production of refraction-based images is that the direction of refraction may be positive or negative along the plane of diffraction. The images reflect this as either a bright spot or a dark spot. It is the variation from the background intensity of a pixel in a refraction image that gives the amount of refraction experienced by that portion of the beam. The absolute intensity of the pixel does not correspond to the level of refraction experienced. Consider the refraction image of a model sheep, shown in part a of Figure 24. When the defocusing effect of the relatively high density plastic on the x-rays passing through it is considered, it is evident that upward refraction should occur along the top edge of the object, and downward refraction should occur along the bottom edge of the object. The amount of refraction experienced is close to the same, but in opposite directions. Because

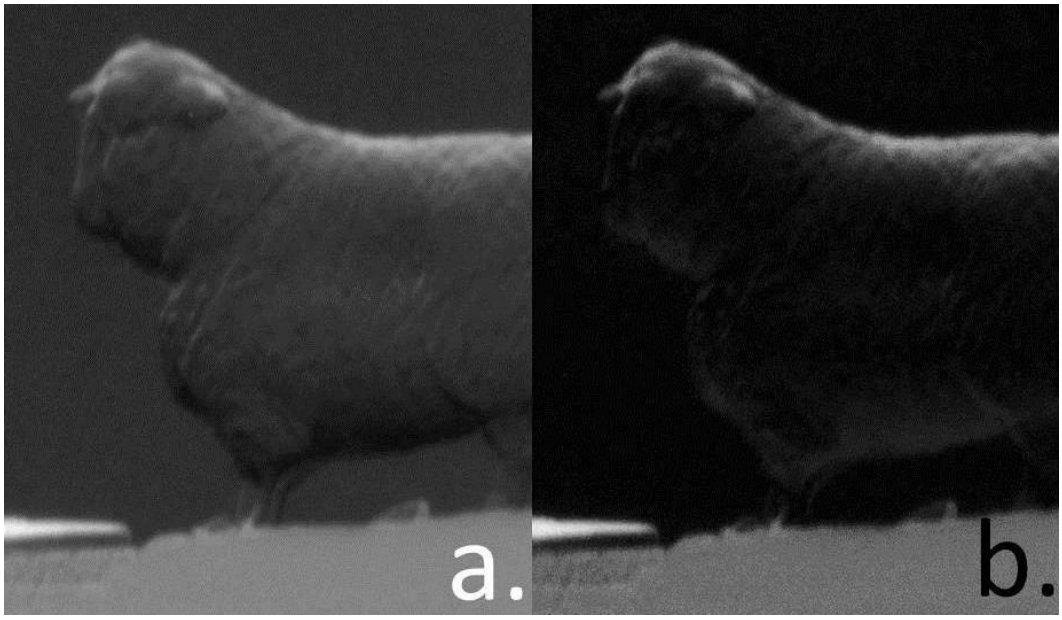

Figure 24: DEI refraction image of a sheep figurine (plastic). a. shows the lighting effect of the object, as upward refraction from the top of the object creates a region of high intensity and downward refraction from the bottom of the object creates a region of low intensity. b. shows the same image displayed as a map of absolute value of refraction, with brightness and contrast adjusted for ease of viewing. *Courtesy Chun Huang*

the intensity of a pixel depends on both the amount of refraction *and* its direction, though, the pixels on the top edge and bottom edge of the object have starkly different intensities. Should the images need to be viewed as a map of the absolute value of refraction experienced by the portion of the beam corresponding to each pixel, they may simply be plotted such that the value of each pixel in the image viewed is the absolute value of the difference between that pixel's original value and that of the image's background intensity (intensity of a part of the beam experiencing no refraction, such as outside the sample). In so doing, information is lost about the density of features (the viewer cannot know if it is greater or less than the surrounding tissue, only that it is different), but perhaps images become closer to what clinical radiologists are accustomed to viewing.

In consideration of linking the techniques of DEI and CT, the direction of refraction sensitivity will again demand consideration.

Lastly, one of the more striking findings during these imaging experiments is that refraction contrast is more notable when imaging at 25% of the peak intensity than at the other points used (50% and 100%). The increased contrast is, at first glance, contrary to intuition, because this point has the lowest signal (lowest photon flux at the detector) of the three. While the same dose is being received by the sample, only one quarter of the incident beam is actually passing beyond the analyzer crystal to become part of the signal at the detector. This lower signal means higher noise in the image *relative to signal*. In attenuation imaging, e.g. traditional x-ray imaging, reducing the signal reduces the contrast. Refraction contrast, however, is determined only by the amount of refraction and the *slope* of the rocking curve at the imaging point. It is independent of the amount of signal (Figure 25). When an image is viewed, though, the visibility of features is due to the ratio of that feature's contrast to the background signal. This ratio does not change in *absorption* images with signal. The ratio which changes is the signal-to-noise (SNR), and hence CNR, since absorption contrast is proportional to the signal; SNR is reduced because the signal decreases while the noise remains unchanged.

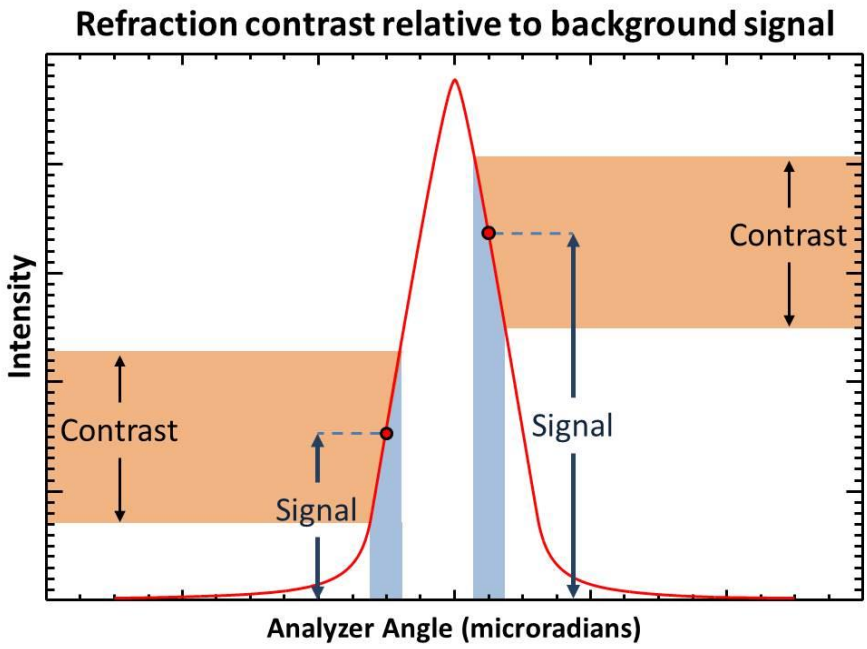

Figure 25: Figure displaying the ratio of refraction contrast to background signal at a point high on the rocking curve vs. a point low on the rocking curve, for refraction of half a microradian in either direction (curve shown is for Si (3,3,3) at 40keV). Note that the contrast due to refraction remains basically the same over the straight portion of the rocking curve, while signal decreases as one moves down the curve. The result is that contrast-to-signal ratio is much higher when imaging near the bottom of the curve than when imaging near the peak.

On the other hand, in a refraction image, when moving down the rocking curve, signal is reduced, but contrast remains the same (so long as slope does not change significantly). Hence, the SNR decreases, but the contrast-to-signal ratio increases (contrast remains the same, signal decreases), while the CNR remains the same. Since the visibility of features is dependent both on the CNR and the contrast-to-signal ratio, imaging at a point low on the rocking curve provides better visibility of soft tissue features (higher contrast-to-signal, unchanged CNR), as can be seen in Figure 26. This is true until the imaging point becomes low enough on the curve that the slope significantly decreases, at which point the contrast is reduced by moving further from the peak. The consideration then, is "how far may one image from the peak", without

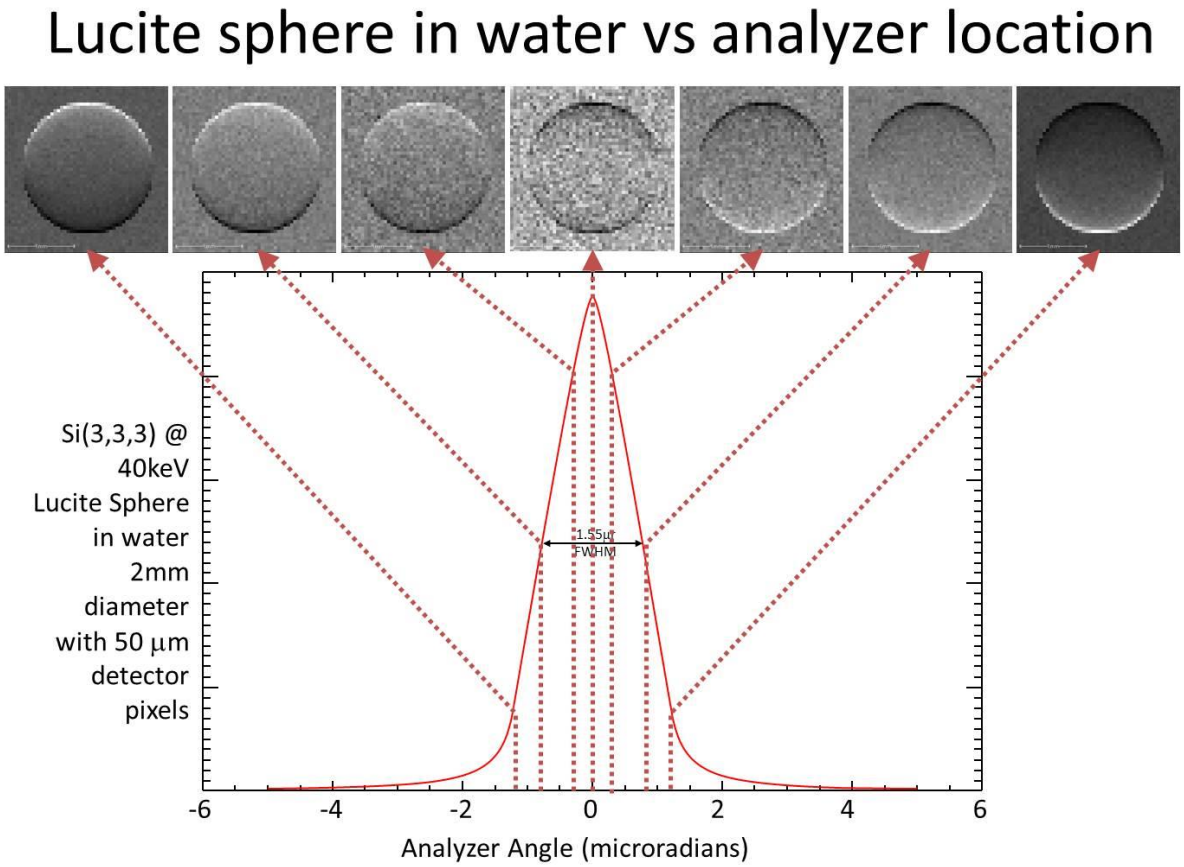

Figure 26: Model of contrast-to-noise ratio of a Lucite sphere in water at different points along the rocking curve. Courtesy L. Dean Chapman

compromising the slope of the curve in the region of refraction by the sample. If imaging is taking place too far down the curve, highly refracted portions of the beam will end up in the tails of the curve, and no longer can intensity change be assumed to linearly relate to amount of refraction experienced. Additionally, imaging lower on the curve produces better contrast to signal in the refraction images, but at the cost of CNR in the absorption images. The balance of CNR and contrast-to-signal ratios in both the absorption and refraction images is one that must be based on the goals of the imager, and the types of samples being imaged. Research that values the absorption images may wish to image at points higher on the rocking curve, while focus on the refraction element calls for imaging in the lower regions of the curve. While

it is quite easy to obtain images at several points on the curve for a given sample, when it comes to considerations of using DEI with CT scans, the point at which imaging will occur needs to be decided upon from the beginning, as additional scans are much more costly in terms of imaging time and absorbed dose.

Conclusion

The basic conclusion of the single projection DEI experiments is that the visibility of soft tissue structures is quite limited, and detail at the level desired is not visible. It is apparent that part of the problem is the overlying contrast from tissue interfaces at different depths than the joint. A way of separating contrast based on depth is needed to gain an understanding of how effectively soft tissues within the joint can actually be visualized using DEI. 2D superimposition is clearly a much larger issue in refraction images which captures contrast from soft tissues than in traditional absorption x-ray imaging, in which most of the tissues at different depths (e.g. skin, muscle, and connective tissue) produces little to no perceptible contrast in the image.

The logical next step was to explore the implementation of CT in combination with DEI. Several considerations were necessary before beginning experiments. These will be outlined in the following sections.

CHAPTER 4: COMPUTED TOMOGRAPHY USING DIFFRACTION ENHANCED IMAGING

Background

Godfrey Hounsfield, the developer of CT, described the novel technique in his famous Nobel Lecture of 1979 (Hounsfield, 1980):

> "When we consider the capabilities of conventional X-ray methods, three main limitations become obvious. Firstly, it is impossible to display within the framework of a two-dimensional X-ray picture all the information contained in the three-dimensional scene under view. Objects situated in depth, i. e. in the third dimension, superimpose, causing confusion to the viewer. Secondly, conventional X-rays cannot distinguish between soft tissues. In general, a radiogram differentiates only between bone and air, as in the lungs. Variations in soft tissues such as the liver and pancreas are not discernible at all and certain other organs may be rendered visible only through the use of radio-opaque dyes. Thirdly, when conventional X-ray methods are used, it is not possible to measure in a quantitative way the separate densities of the individual substances through which the X-ray has passed. The radiogram records the mean absorption by all the various tissues which the X-ray has penetrated. This is of little use for quantitative measurement. Computed tomography, on the other hand, measures the attenuation of X-ray beams passing through sections of the body from hundreds of different angles, and then, from the evidence of these measurements, a computer is able to reconstruct pictures of the body's interior."

After image reconstruction, CT allows a three-dimensional representation of the sample, such that contrast from features at different depths are no longer superimposed on one another, but able to be separated and viewed as independent structures. While this advantage is very valuable in traditional absorption imaging, the additional features providing contrast in a

refraction-based image makes the value of CT that much greater. The combination of technology capable of imaging soft tissue detail with an imaging technique allowing the sorting out of the obtained contrast truly does overcome the first two limitations of conventional x-ray imaging outlined by Hounsfield. Additionally, by identifying the depth from which contrast is originating, the density of any part of the sample can be quantified (the third limitation).

Literary Review

DEI-CT is a very new technology. It has been implemented at the Photon Factory, KEK, Japan, and used for micro-CT of a microvessel of hepatic fibrosis in rats (Duan, Hu, Luo, Zhao, & Wang, 2013) and study of microvascular proliferation in a mouse model (Seo et al., 2012). Mapping of breast tissue samples has been demonstrated with DEI-CT at the European Synchrotron Radiation Facility (Bravin et al., 2007; Keyriläinen et al., 2008). DEI-CT has been implemented at the National Synchrotron Light Source, USA (Brankov et al., 2006), and used for Alzheimer's research in a mouse model (Connor et al., 2009). DEI-CT has been used for imaging of human cadaveric knee joints, also at the National Synchrotron Light Source (Li, Zhong, Connor, Mollenhauer, & Muehleman, 2009). The results in each case to date have shown DEI-CT to be effective for high-resolution imaging of samples of soft tissues. The research described in this thesis represents the first implementation of DEI-CT in Canada.

Materials and Methods

DEI-CT methods were applied to imaging intact joints of young piglets. A porcine model was chosen, as in the DEI experiments. Image joints were obtained from 4 week old piglets, once again, as the growth plate at this stage of development has not fused, but ossification centers have developed to the point that the full joint space and some trabecular bone within the ossification centers still fit in the vertical beam size. Additionally, 4 week old samples were an ideal size for the field of view of the 18.7 µm pixel size Photonic Science detector for comparison with planar DEI experiments. Samples were prepared as in the DEI experiments. Rear legs were excised at the hip. Samples were transported to BMIT in plastic bags, and skinned (1st two experiments) or shaven (2nd two experiments). Soft tissues were left intact. Samples were then mounted in the cylindrical holder for imaging, and scanned (see Figure 27). The DEI-CT holder was an acrylic cylinder made of threaded sections which could be arranged to give a clear view of the joint space. A threaded aluminum base provided mounting holes matching those on the stage at BMIT. The holder was made to specification by RMD engineering, Saskatoon, SK, Canada. Outside diameter was 70mm for the initial scans (200µm voxel size); diameter was reduced to 68mm for the higher resolution scans, allowing unfiltered beam to pass onto the detector on both sides for

Figure 27: Fresh porcine stifle sample, mounted in holder and ready for imaging.

calibration during reconstruction. Afterwards samples were generally frozen, preserved for later reference and additional information if needed.

The first DEI-CT scans to be taken at the CLS were performed at 200µm voxel size with a Hamamatsu flat pane (model: C9252DK-14), on an intact, fresh stifle joint from a healthy 4 week old piglet with the skin removed. The imaging procedure involved several scans at the top of the rocking curve, as well as several sets on either side of the curve at approximately the half peak of the curve. Exposure time for each projection was 33ms; the dataset included 1188 projections. Imaging energy was 40 keV (harmonic of Si (2,2,0)). Since initially the setup for DEI-CT was quite time-consuming, and image acquisition times for these relatively low resolution scans was quite fast, we chose to take a series of CT scans, beginning inferior to the joint, and moving proximally with each scan, such that the datasets might later be "stitched" together, forming an 3D dataset with a much greater field of view than the few millimeters of beam height at BMIT. While crystal stability was not much of an issue during the scans at the top of the rocking curve, crystal drift proved to be quite detrimental to scans lower down the curve. While images from these datasets demonstrate some soft tissue structure, further experiments were required to understand the DEI-CT's potential.

High Resolution DEI-CT

After initial success imaging at 200µm voxel size, we moved to DEI-CT imaging at 37.4 µm voxel size using the Photonic Science detector and a modified joint holder customized thereto. The Photonic Science detector has a pixel size of 18.7µm. In interest of scanning time,

2x2 pixel binning was applied (see note in next paragraph). Holder modification was simply a 2mm reduction to the outside diameter of the acrylic tube in which the joint is secured for scans. This reduced the diameter to 68mm, such that beam unfiltered by the sample is included in the images on either side of the sample. This "unfiltered" beam is important for normalization of each projection in the dataset.

The Photonic Science detector actually has a pixel size of 18.7µm. Using 2x2 pixel binning on the detector allowed a 37.4µm pixel size for projections. This 2-fold increase in voxel size provides at minimum an 8-fold reduction in dose and imaging time required for a dataset, based on voxel SNR of the images. At 37.4µm pixel size, scan times were around 2 hours for each side of the rocking curve, which seemed reasonable for pilot high resolution scans. Dose under these conditions was estimated by Zohreh Izadifar[2] as 3.4 Gy. There are ways such as reduction in number of projections, binning of projections pixels, and region of interest imaging, that may reduce dose to acceptable levels in the range of several mGy, but reduction of dose was outside the scope of this research.

Images were acquired at the top of the rocking curve, as well as at 50% of the peak intensity on either side. A novel control system was developed to stabilize the analyzer crystal orientation during scans. This control system is described in the following chapter and was used in acquisition of these images.

Further high resolution DEI-CT imaging was performed on similar, fresh, healthy stifle joints from 4 week piglets. Skin was shaven and left intact in these samples. The scans included two samples that were artificially damaged post-mortem, using a scalpel and needle.

[2] Personal communication, 2015

In the first instance, upon dissection after scanning, it was found that damage occurred inferior to the field of view of the scans. For the next scans, damage was induced using two acupuncture needles (~290 µm diameter, solid core). The sample was then scanned with the needles in place, and immediately scanned again upon removing the needles. Position and posture of the sample in the holder were minimally affected by removing the needles, giving us a good indication of exactly where the damage should be found.

In the final imaging experiment performed using DEI-CT during the course of research pertaining to the Master of Science degree, injection of radiocontrast agent into the artery of the leg was attempted in order to trace the flow of blood through the joint, and to establish how well injected contrast agents might be used for further research of the cartilage vasculature system. Radiocontrast agents are a contrast medium for *absorption* contrast. They are generally "radiopaque", meaning they highly absorb x-rays. However, typically the concern is primarily with the refraction images of the dataset, as they contain the most information about the cartilage. Radiocontrast agents are not designed to maximize refraction, as this is not a source of contrast in clinical scans. One benefit of DEI, though, is that both an absorption and a refraction dataset can be obtained from the same set of scans. The radiocontrast agent might be used to map out vasculature in the absorption dataset, and this overlaid on the refraction dataset, which would be used for further examination of the joint.

Results

Figure 28 and Figure 29 show images from the top of the rocking curve. Imaging at the

peak produces an image where refraction and absorption contrast are both represented, but cannot be separated.

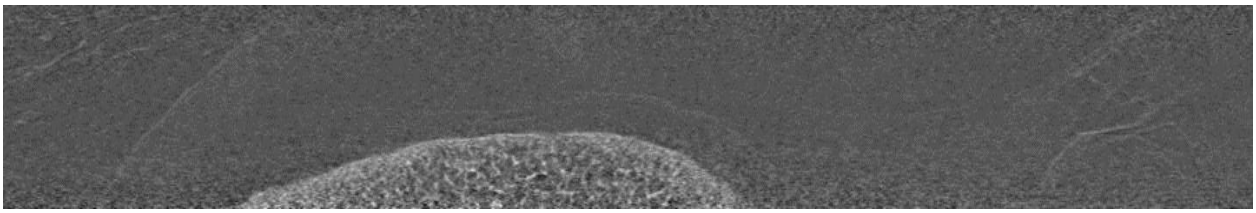

Figure 28: Sagittal view from the dataset taken at the top of the rocking curve.

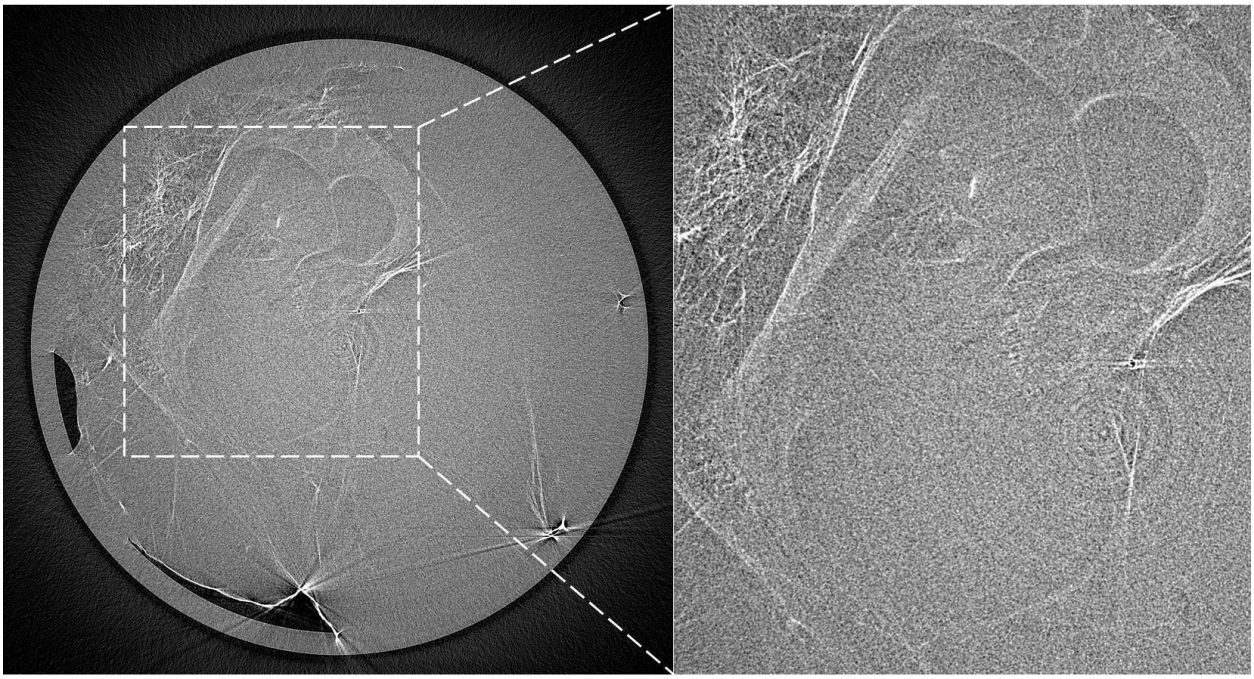

Figure 29: Slice through femoral and tibial cartilage from dataset taken at the top of the rocking curve.

Refraction images were of the most interest, as they demonstrate the greatest cartilage and soft tissue detail. The following images shown in this section are each from the reconstructed 3D refraction dataset. Cartilage detail is certainly visible, and the images indicate a tremendous increase in perceptible details over single projection refraction images of 18.7µm pixel size. Cartilage edges are very clear, and the cartilage-bone interface can be easily

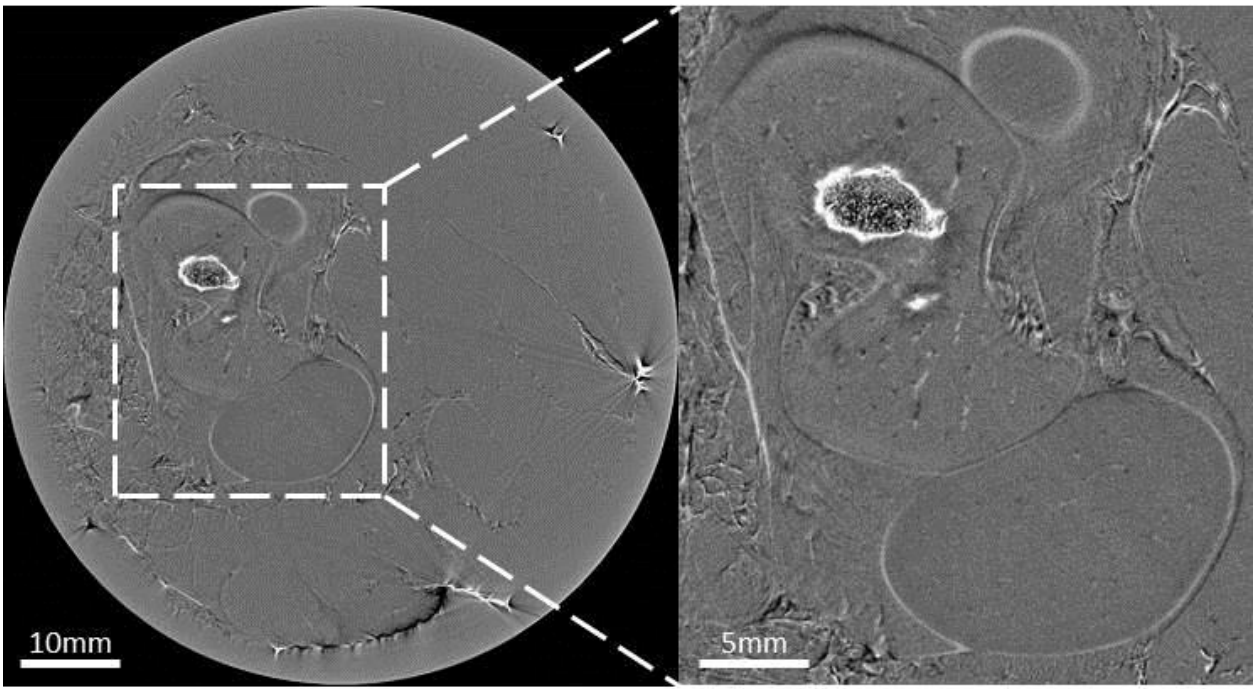

Figure 30: Slices from the first DEI-CT dataset taken with the novel feedback control system described in the next chapter. Voxel size is 37.4 μm. Slice is through the proximal end of the tibial ossification center, displaying trabecular and cortical bone, tibial and femoral epiphyseal cartilage.

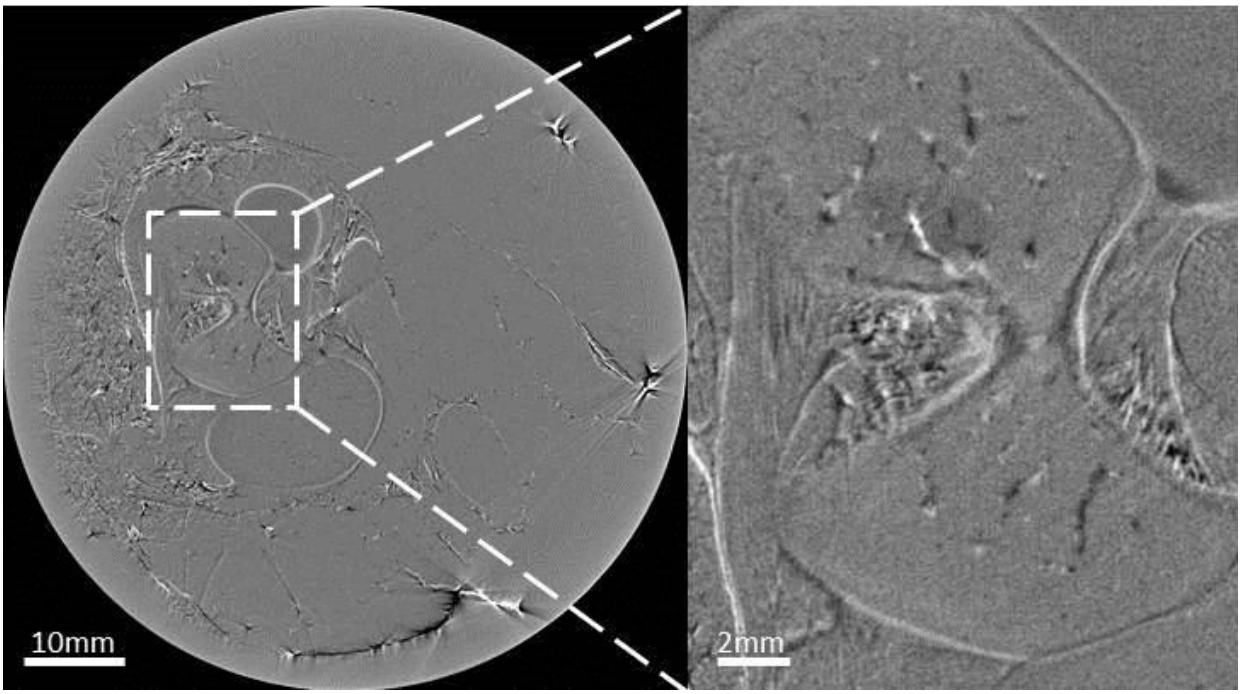

Figure 31: Another slice from the first DEI-CT dataset using the feedback system. This slice is through the center of the joint, such that it intersects the epiphyseal cartilage of both the femur and the tibia. Vasculature within the epiphyseal cartilage is clearly visible, as are some of the ligaments.

investigated. Additionally, the cortical shell and trabecular structure of the bone are still notably well relayed by the refraction images. Further, the images display the ligaments within the joint surprisingly well. CT technology combined with DEI has proven very capable of separating the complex interplay of both hard and soft tissues within the joint.

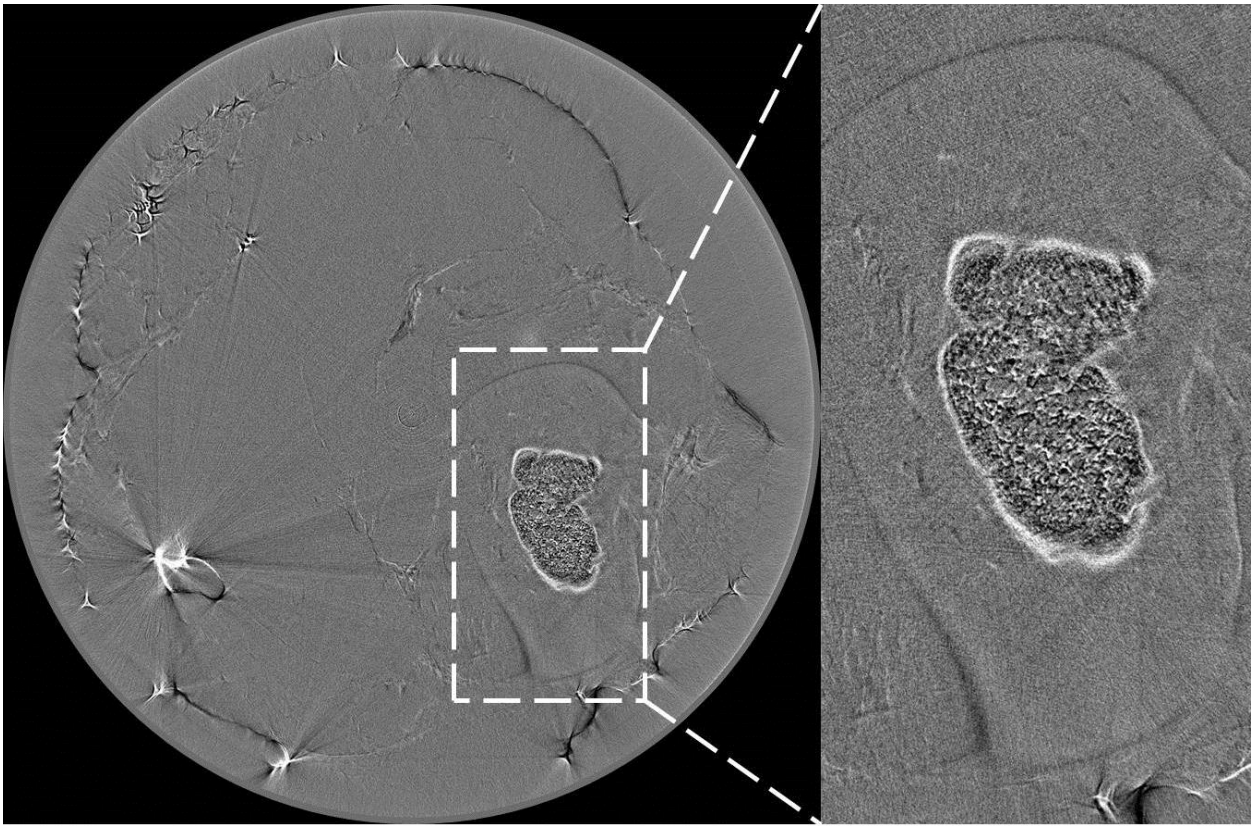

Figure 32: DEI-CT slice through tibial ossification center at 37.4µmvoxel size.

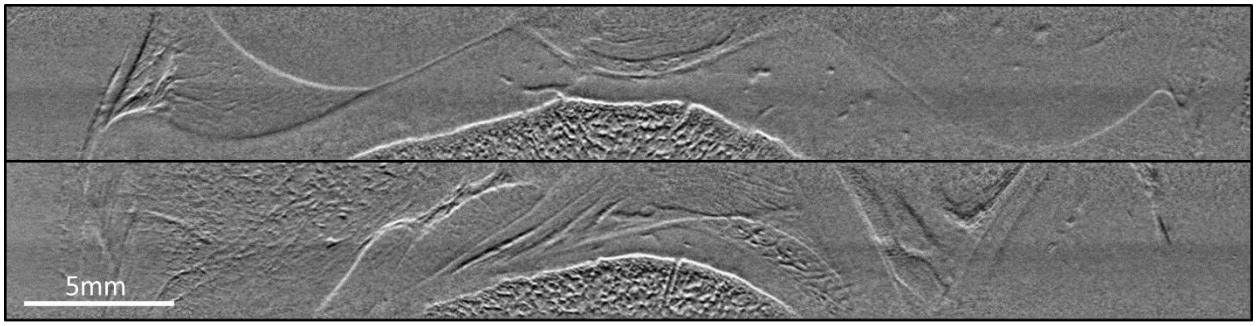

Figure 33: Coronal (top) and sagittal (bottom) sections approximately mid-joint of the original DEI-CT scans with the novel feedback system. The tibial ossification center is visible in the bottom of each image. Vasculature is visible within the cartilage in the coronal image and cruciate ligaments are demonstrated by the sagittal image.

However, the most striking finding in these images was the presence of vasculature within the cartilage. Initially the markings in the cartilage were baffling, and interference or noise of some kind producing the contrast "splotches" within the cartilage was predicted. Refinement of the reconstruction algorithm's center of rotation showed that the contrast in the cartilage was indeed due to a system of canals. These canals underscored the importance of accurate center of rotation alignment during the reconstruction process. This conclusion was confirmed with alternate methods of visualization, including z-project (see next paragraph) and resampling of the dataset in oblique planes. A close examination of Figure 33 will reveal that canals traverse even the cortical shell and trabecular bone structure. These canals are further highlighted in Figure 34.

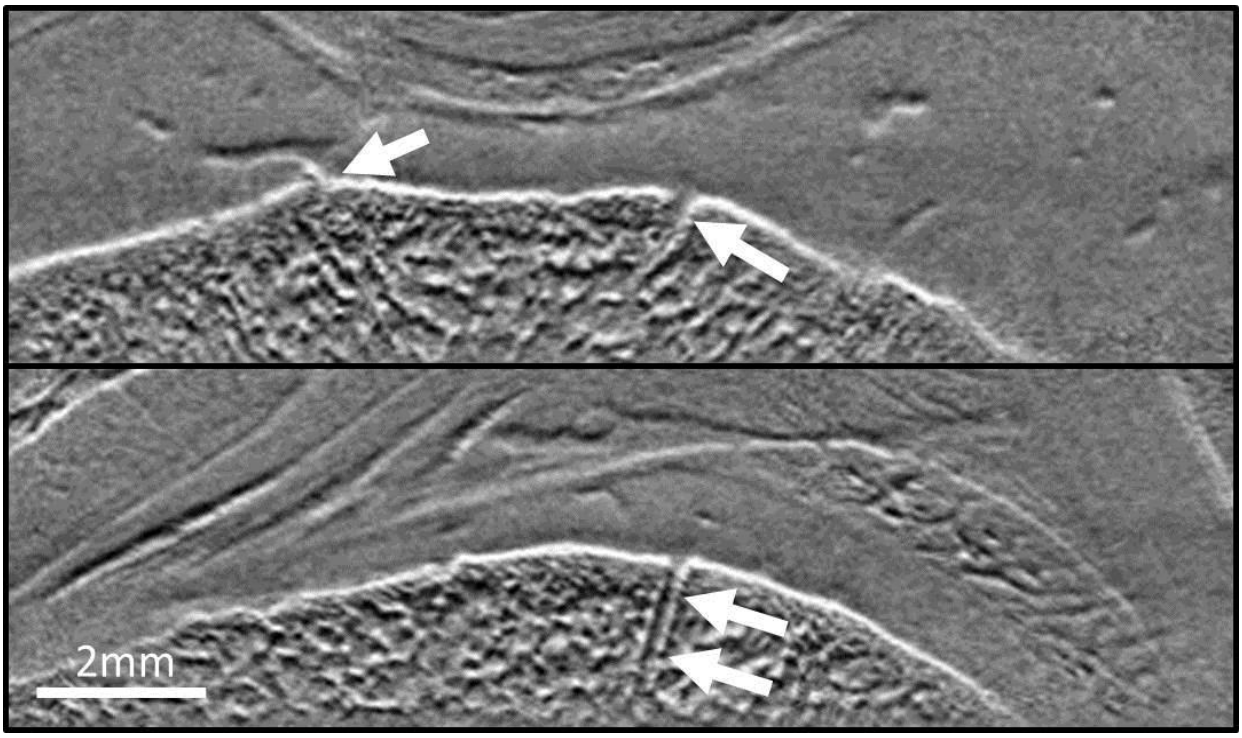

Figure 34: Portions of the DEI-CT dataset highlighting canals traversing the cortical shell and continuing through the trabecular bone structure.

However, the most notable of the visualization methods explored is that known as a "Z-

project". ImageJ software (Rasband, 1997) was used for this visualization of the dataset. A z-projection is an image whose intensity is produced by taking a function of pixel intensities through several slices in the dataset. This method of visualization is particularly well-suited to examining the vasculature in these images. While a single slice tends to give an oblique cross-sectional look at any given canal, a z-projection of the standard deviation through several slices allowed us to more easily map this vasculature's seemingly erratic path through the cartilage. Figure 35 displays a region in the center of the joint using this method.

To my knowledge, the vasculature of cartilage has never before been visualized using x-rays. These canals have been visualized previously in porcine models with ultrasound and MRI (Babyn et al., 1996; Tóth et al., 2013), but the only imaging of this system of canals has been *ex-vivo* in animal models until very recently (Nissi et al., 2014). They are typically imaged using MRI with a contrast agent (Barnewolt, Shapiro, & Jaramillo, 1997; Jaramillo et al., 2004). These canals are a good demonstration of the effectiveness of DEI-CT in visualizing joint detail, and offer an exciting opportunity for the study of joint development.

Not only are these canals an exciting demonstration of the visibility of anatomical substructures within the joint to this imaging method, but they also provide a sort of biological metric by which to grasp the true resolution of the images. The canal highlighted by a double arrow in Figure 34 has an approximate diameter of 230µm. The canal is clearly resolvable, *and* both "walls" of the canal are clearly resolvable, each outlined by the signature dark-bright intensity pattern of an object of high relative density in a refraction-based dataset. Indeed, enlarging these images to the point of pixilation, it is obvious that the true resolution is limited by the 37.4µm pixel size of the detector.

Figure 35: Standard deviation z-projection through approximately 200μm of the dataset. This type of visualization of the dataset is particularly suited to displaying the vasculature within the cartilage.

The further high resolution DEI-CT imaging demonstrated the reproducibility of the technique, confirmed findings from the first sample and dataset, and captured images of artificial damage, as well as the structures visible near the tibial growth plate. Examination of

the second high resolution DEI-CT scans again showed that DEI-CT at 37.4µm voxel size clearly details joint structures of both hard and soft tissue, including trabecular and cortical bone, epiphyseal cartilage and its vasculature in a juvenile joint, ligaments, and surrounding muscle and connective tissue as seen in Figures 36-44.

Z-projection through the epiphyseal cartilage of both the tibia and femur further demonstrate the vasculature within the cartilage (see Figure 38). Cartilage detail, cortical shell, trabecular structure and cruciate ligaments are again visible in the selected coronal and sagittal

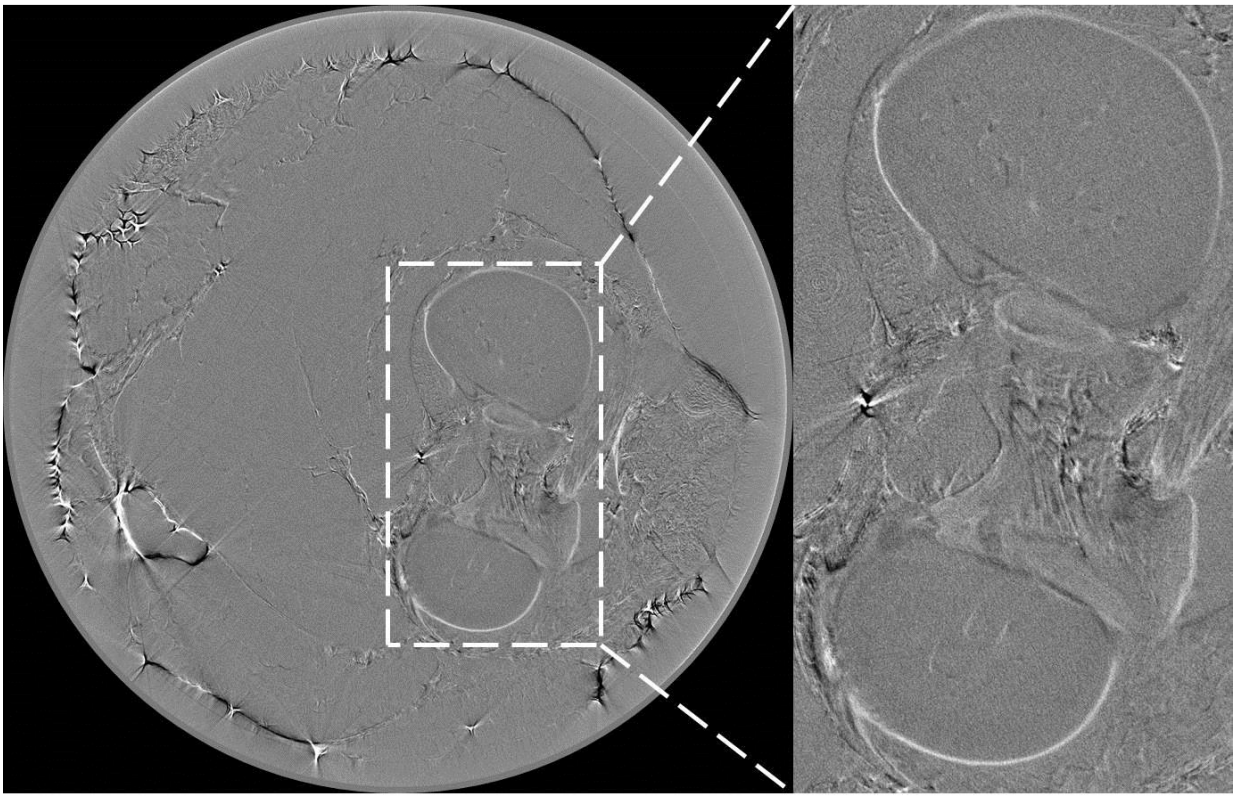

Figure 36: DEI-CT slice through femoral epiphyseal cartilage at 37.4µm voxel size

slices of Figure 39. It should be noted that this sample was artificially damaged post-mortem

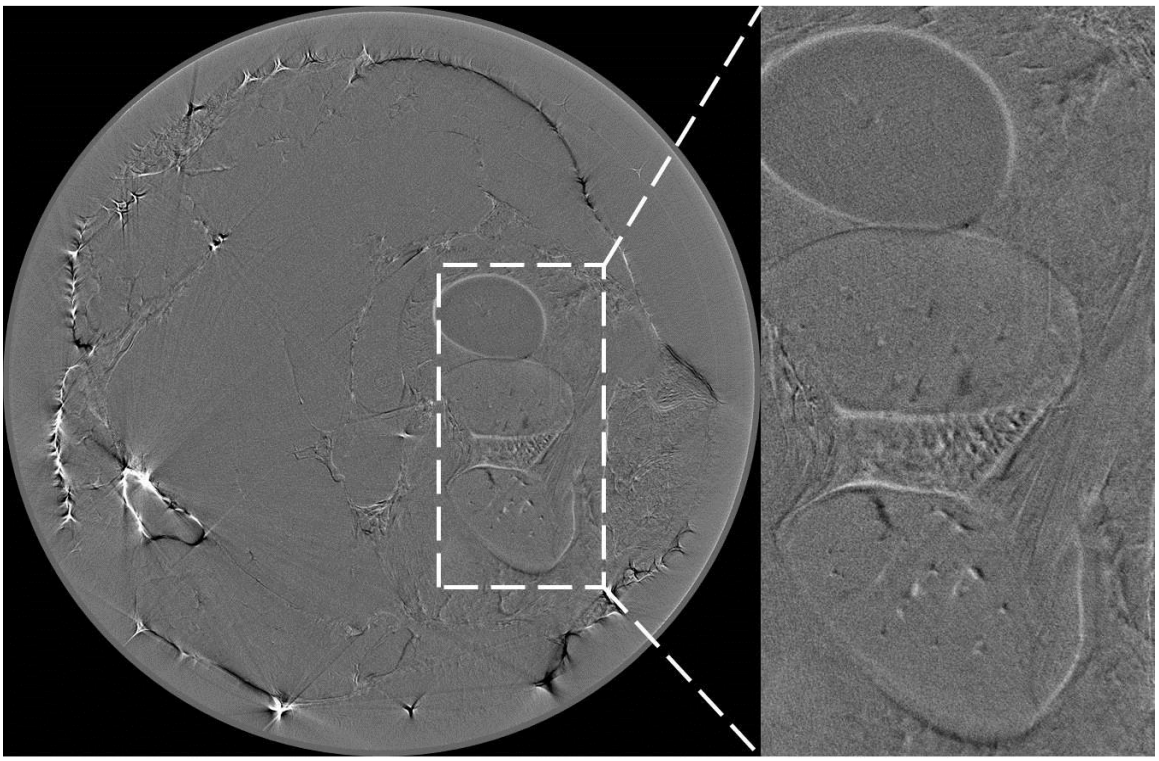

Figure 37: DEI-CT slice through tibial epiphyseal cartilage at 37.4µmvoxel size.

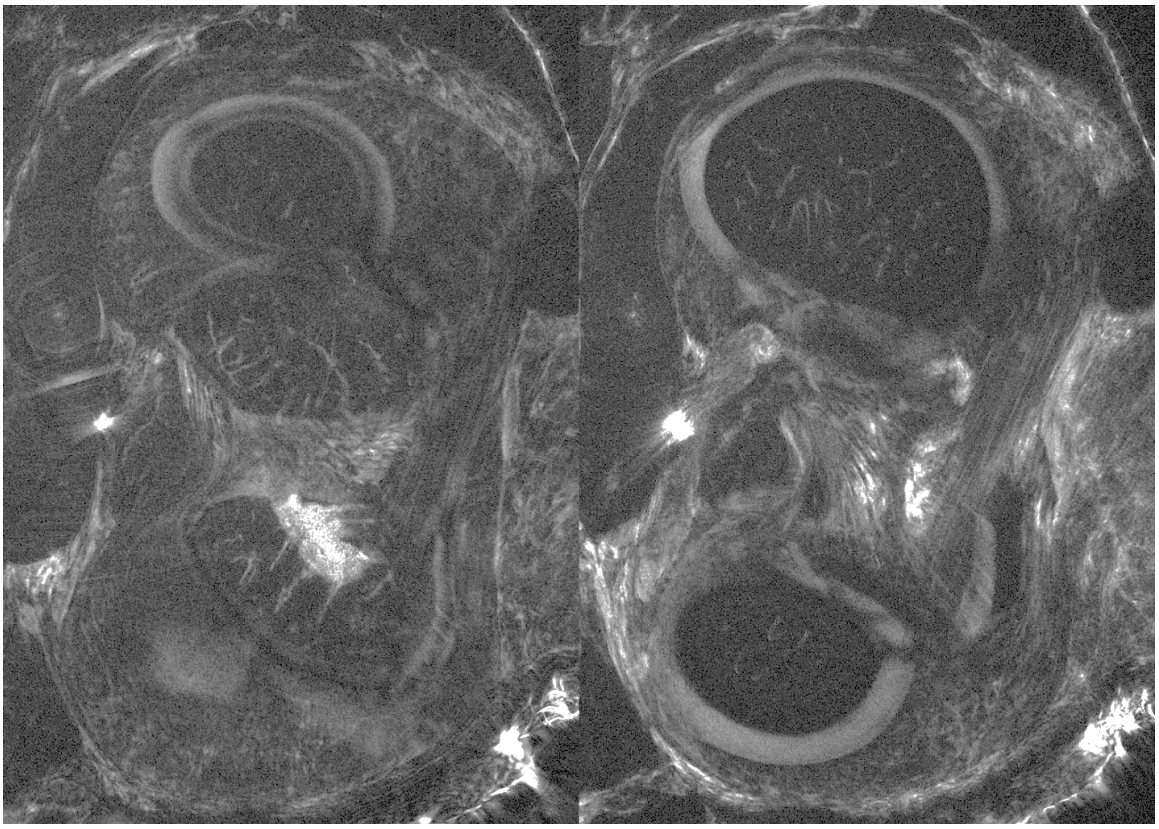

Figure 38: Z-projection through 20 slices in the region of the tibial epiphyseal cartilage (left) and the femoral epiphyseal cartilage (right)

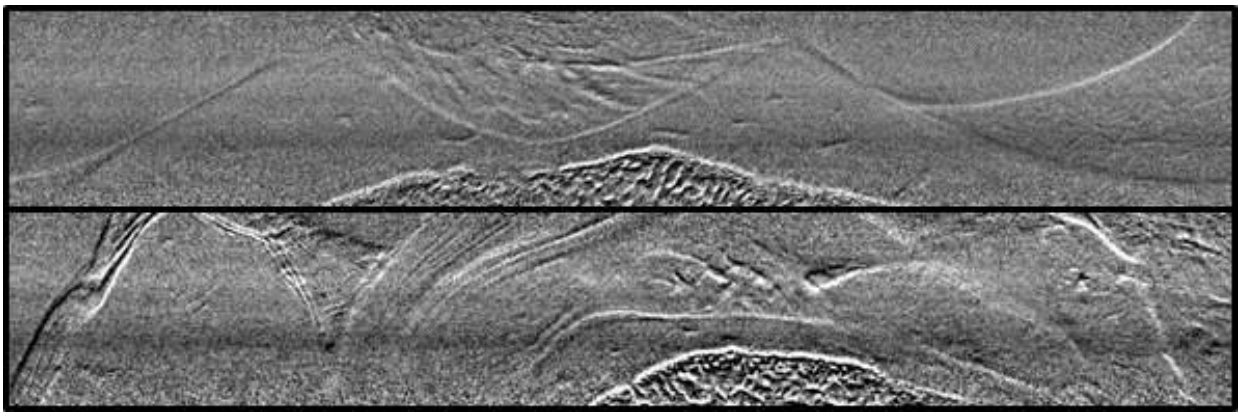

Figure 39: Coronal (top) and Sagittal (bottom) slices through the epiphyseal cartilage and tibial ossification center, displaying cartilage vasculature, cruciate ligament, and cortical and trabecular bone structure.

using a scalpel and needle. Upon dissection after scanning, it was found that damage occurred inferior to the field of view of the scans. Damage was sustained near the tibial growth plate, and only intersected the most distal few slices of the dataset, where signal was so low as to seriously obscure contrast.

To avoid this issue in the next scans, damage was induced using two acupuncture needles (~290 µm diameter, solid core). The sample was then scanned with the needles in place (Figure 40), and immediately scanned again upon removing the needles (Figures 41-42). Position and posture of the sample in the holder were minimally affected by removing the needles, giving a good indication of exactly where the damage should be found. As before, it was found that damage was induced near the tibial growth plate, and the field of view of the DEI-CT scans was adjusted accordingly. This was of two-fold benefit, as it not only captured the damaged area, but also shed light on another interesting portion of a growing joint, viz. the tibial growth plate.

One challenge to detecting artificially induced damage to the cartilage is the viscoelasticity of the cartilage itself. While hard tissues like bone will maintain the effects of the damage indefinitely, the viscoelasticity of cartilage allows it to close around a needle as the needle is removed. It should not then be expected that the needles' trails will be an exact model of the needle's shape or size. The actual characteristics of the needle trail through the cartilage were unknown before the imaging was performed, which made a precise method for locating them within the dataset all the more valuable.

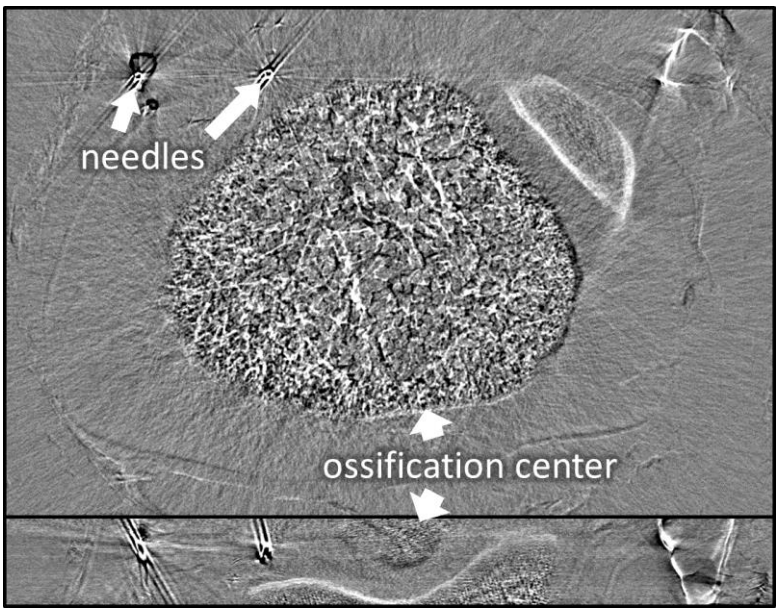

Figure 40: A transverse (top) and approximately coronal (bottom) slice from the DEI-CT scan with the needles in place, showing their positions. Needles are labelled in the transverse slice, and clearly visible directly below in the coronal slice.

Review of the scans after removal of the needles by single slices (Figure 41) clearly shows the damage from the deeper of the two needles in both transverse and coronal views. However, no damage from the other needle was found in the scans. Based on this method of visualization alone, it would seem that the damage is not visible, at least not with the imaging parameters utilized.

However, visualization of the cartilage with a z-projection through the damaged area proved very enlightening. It may be recalled that the acupuncture needles were removed after initial imaging, and imaging was repeated. While movement of the sample was avoided as

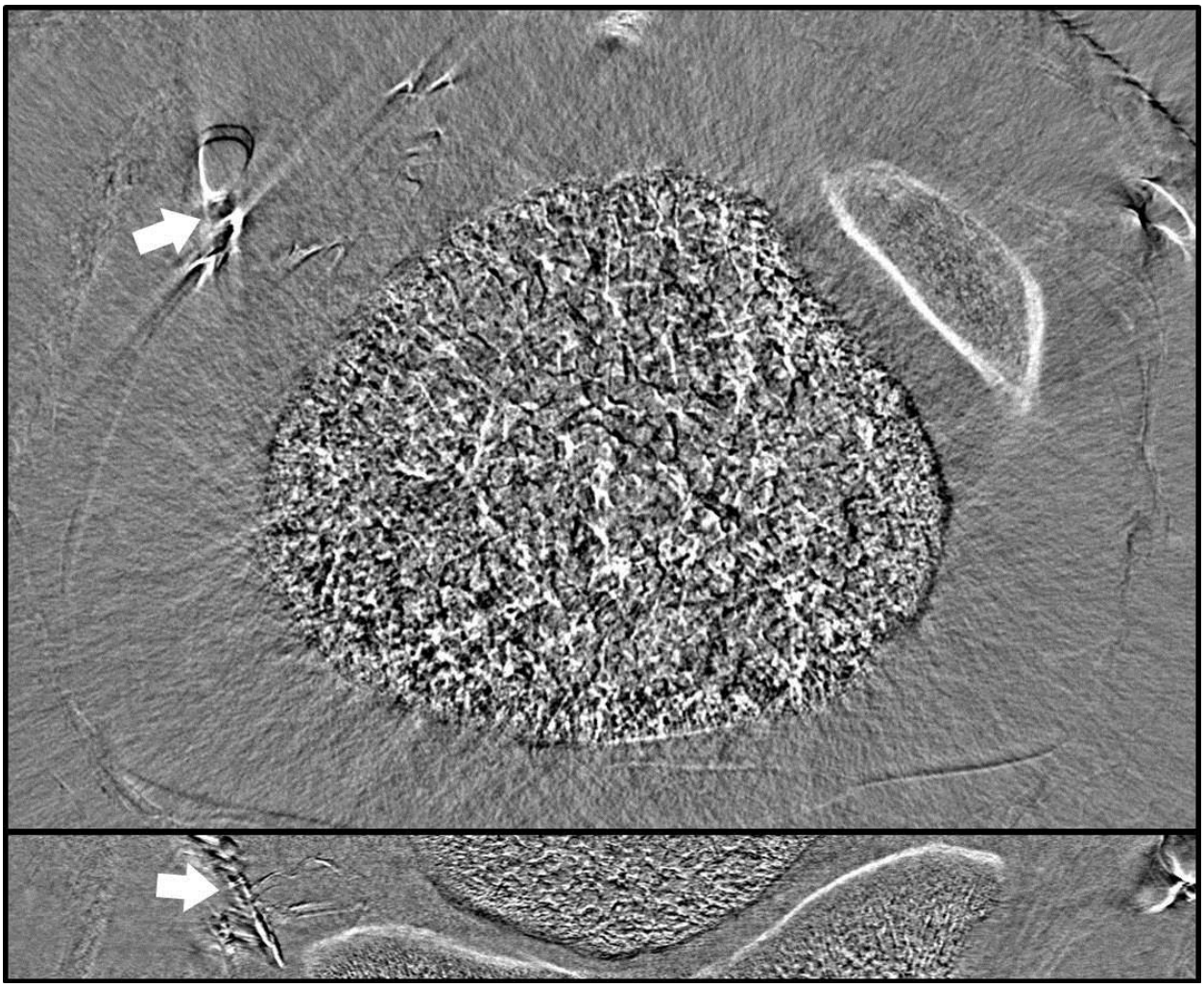

Figure 41: A transverse (top) and approximately coronal (bottom) slice from the DEI-CT scan after removal of the needles. Damage from the leftmost needle is denoted by the arrows in both images.

much as possible, some movement of the sample was inevitable during removal of the needles, as well as in remounting the holder to the stage. Slight rotation of the sample between the two scans can easily change the apparent horizontal position of the needle tracks in the coronal view. Z-projection visualization of the DEI-CT dataset of the joint after needle removal seems to suggest that this was the case. Employing this visualization technique based on both standard deviation through the slices and summation of pixel intensities through the slices, demonstrated the actual damage very pronouncedly (Figure 42).

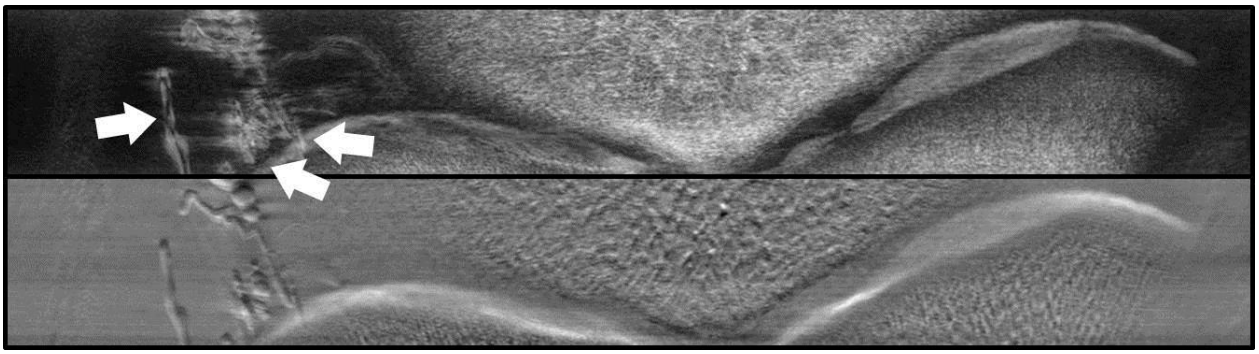

Figure 42: Z-projection of standard deviation (top) and sum (bottom) through the slices in the damaged area. Several needle tracks are visible in both images, labelled in the z-projection.

The cartilage's elasticity and resistance to puncture means that needle placement within the cartilage of the intact joint can be challenging. In this sample, the more proximal needle was pushed in more than once, in an attempt to lodge the delicate needle in the bone itself. From Figure 42 it seems clear that the cartilage was punctured each time, as there are several small tracks converging on the cortical shell of the tibia, while only one track of damage, isolated from the rest, continues out of the field of view. This track placement aligns well with what was predicted by initial scans of needle positions.

This imaging experiment demonstrated the ability to detect small-scale damage to the cartilage using high resolution DEI-CT. It also provided a dataset with known damage that might be used to analyze the effects of decreased resolution and signal. Additionally, the images emphasize the value of implementing visualization techniques outside the obvious option of single slice orthogonal views of the dataset. The need for user-friendly visualization software for refraction-based images is heavily underscored by the great increase in detail visible in these two relatively simple visualization techniques (i.e. z-projection of standard deviation and sum). Lastly, the trabecular structure of the tibia near the growth plate was displayed by the scans. Trabecular structure near this quickly ossifying area is distinctly

different in pattern that that near the outer edges of the bone (Figure 41, Figure 42). The images also demonstrate that this portion of the tibia has a different trabecular structure than that of the ossification center. The ability of DEI-CT to relay information on cartilage damage, cortical shell condition, trabecular pattern relating to bone growth, and surrounding structures such as ligaments places it center stage for joint visualization.

The last experiment involved the injection of radiocontrast agent into the artery of the leg in an attempt to trace the flow of blood through the joint, and to establish how well injected contrast agents might be used for further research of the cartilage vasculature system.

Ioversal, a common clinical iodine contrast agent, obtained from the Royal University Hospital, was injected in the femoral artery. It was here that the first serious challenge was realized. Although the sample was relatively fresh (within a few hours of euthanization), coagulation of the blood had occurred, and displacement of the coagulated blood by the contrast solution was not possible even in the artery itself. Flow of the agent through the smaller vessels was precluded by the issue.

Imaging of the sample injected with Ioversal was, however, continued. While no contrast agent is within the field of view of the images, the images provided some excellent displays of vasculature within the femoral condyles, as well as some excellent visualization of the cruciate ligaments, exhibited by Figure 43.

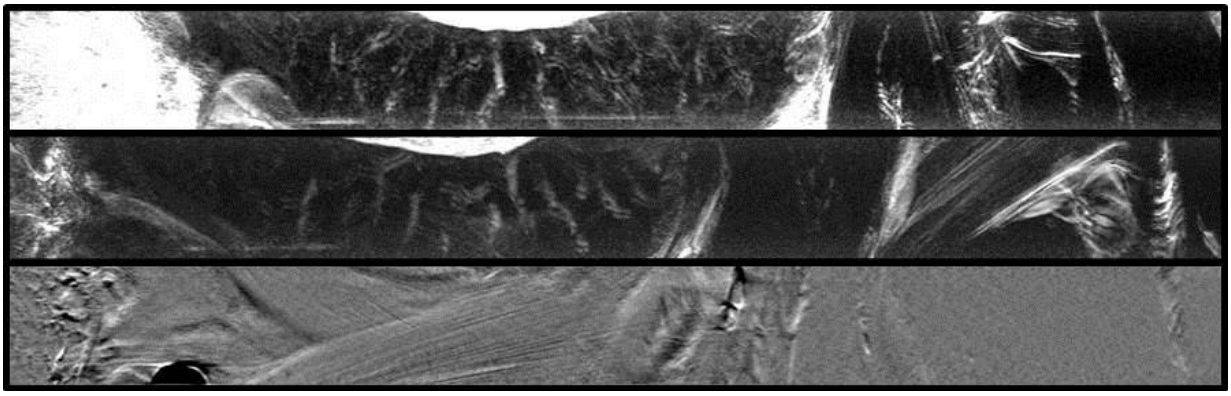

Figure 43: Sagittal z-projection visualizations of fresh, fully intact, 4 week porcine stifle joint at 37.4µm. Standard deviation projections highlight cartilage vasculature in one of the femoral condyles (top), and a ligament (middle). Sum projection highlights both cruciate ligaments near center of joint (bottom).

Discussion

Up to this point, DEI-CT had never been implemented at the CLS or anywhere in Canada. Despite the cost in time and effort of setting up and troubleshooting a new imaging system at the BMIT beamline, we realized the overwhelming value of piloting the technology for the benefit to this project, as well as the benefit of making the technology readily available to other light source users (Webb, Belev, Wysokinski, & Chapman, 2013). This value was quickly realized in another project implementing the exact technology and setup only a few months following our initial scans, this time for tissue engineering research (Izadifar, Chapman, & Chen, 2014).

CT Challenges

Apart from the challenges associated with a different contrast mechanism (refraction) and its directional sensitivity, CT presents a few other challenges to its users. A CT dataset is

typically composed of hundreds of projections taken at different angles. Dose considerations become much more important as well as considerations of image acquisition time. While a single projection image may have an exposure time of only a few seconds, taking a dataset composed of over a thousand of these projections puts the scan times into the realm of a few hours. Dose is raised proportionally. The imaging time consideration proved to be the biggest challenge to implementing DEI-CT. In this research, samples were imaged *ex vivo*, so the requirements in anaesthetization times and absorbed dose were not of immediate concern. However, keeping the imaging system itself stable on the range of nanoradians throughout the scan proved to require a control system. The analyzer crystal, subject to thermal expansion due to beam absorption, regularly drifted in angle by more than a Darwin width over the course of a high resolution DEI-CT scan, leaving us well off the rocking curve by the end of data acquisition. This challenge gave birth to a novel feedback control system, described in the next chapter.

Advantages of DEI-CT over DEI

Superimposition of a three-dimensional structure on to a two-dimensional picture means that contrast from all tissues and interfaces in the sample are placed atop one another. In absorption images, this is basically limited to contrast from overlapping bone structures, but implementing a technique sensitive to soft tissue contrast means that now not only is contrast being superimposed from each layer of bone, but on top of that, contrast from all overlapping cartilage edges, ligaments, muscles, skin surfaces and connective tissues. While there is a lot more contrast to sort through with refraction-based imaging, CT still enables the sorting out of the sources of contrast based on their depth (Wiebe et al., 2013). This advantage is

dramatically shown in the amount of cartilage detail visible in the single projection scans of a porcine stifle joint compared with DEI-CT scans of an identical joint (Figure 44).

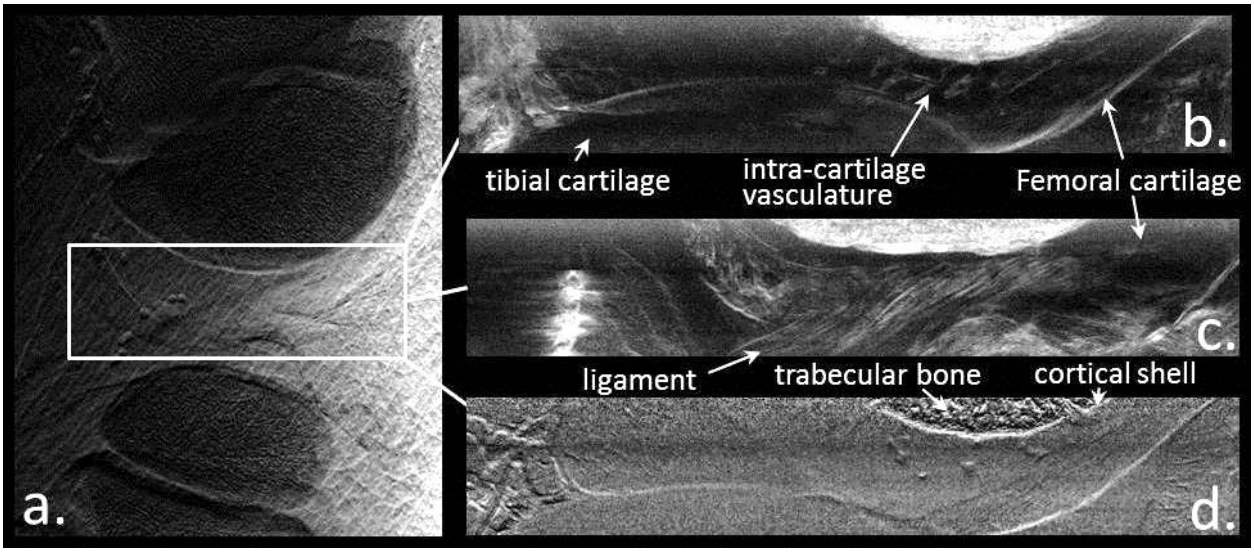

Figure 44: DEI vs. DEI-CT on a 4 week porcine stifle joint a.) single projection DEI scan b.) DEI-CT refraction image at depth of femoral condyle c.) at depth of ligaments and d.) at depth of cartilage, showing bone structure. DEI-CT images are resampled in z-plane.

In reviewing Hounsfield's Nobel Prize speech, projection DEI suffers from the same issues that plague projection radiography with some interesting differences. With projection DEI the first (superposition) and third (quantification) issues with planar radiography still directly apply. Arguably, the contrast is better for soft tissues which mitigates a bit of the second concern (lack of soft tissue contrast). There is another subtle difference in the interrogation of the beam between DEI's refraction images and those based on beam attenuation. Attenuation of a beam is *always* additive through the sample, i.e. each part of the sample interrogated by the beam provides some positive attenuation, adding to the overall beam attenuation. Refraction of the beam, however, may occur in two different directions. It may add or subtract from the cumulative refraction. To illustrate this effect, consider a portion

of the beam as it passes through a cylinder of water as shown in Figure 45. As the beam enters the sample, it is refracted upward, for example, by 5 µrad. As it exits the cylinder, it will then experience a *downward* refraction of 5 µrad, such that the two refraction events completely cancel one another. This cancelling potential of beam refraction means that the overall value of beam refraction through a sample may be very small, even zero, although it experienced a great amount of refraction passing through the sample. This characteristic of refraction underscores the increased value of CT for refraction-based images over attenuation-based images. In certain projections, a cylindrical object will completely disappear from DEI images. Once the CT dataset is reconstructed, however, the other projections will clearly identify this feature, and the intensity of voxels along that object will be quantifiable. It is interesting to note that it is in the projection in which the beam experiences the *greatest* amount of refraction that the cylinder will disappear. Despite this cancellation of the greatest refraction events experienced, the total CT dataset will still recover the full amount of refraction at the point from the other projections, such that the refraction at the interface will still be quantified therein (Dilmanian et al., 2000).

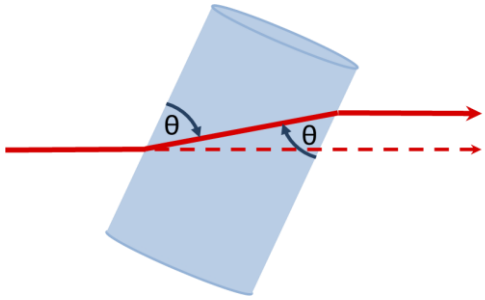

Figure 45: The two refraction events created as the beam travels through a cylinder of water tilted in the direction of the beam cancel one another.

Direction sensitivity and DEI-CT

It must again be considered that refraction images produced with DEI have directional sensitivity in the direction of beam diffraction by the analyzer. In the setup employed (Figure 13), images are sensitive to vertical refraction of the beam by sample features. Rotating the sample about a vertical axis while performing a CT scan will produce a usable dataset, as the density gradients providing contrast are aligned with the axis of rotation, and therefore, while the amount of refraction may vary in each projection, the direction of that refraction will not (Figure 46a). Consider, however, a cylindrical sample placed across the beam, and rotated

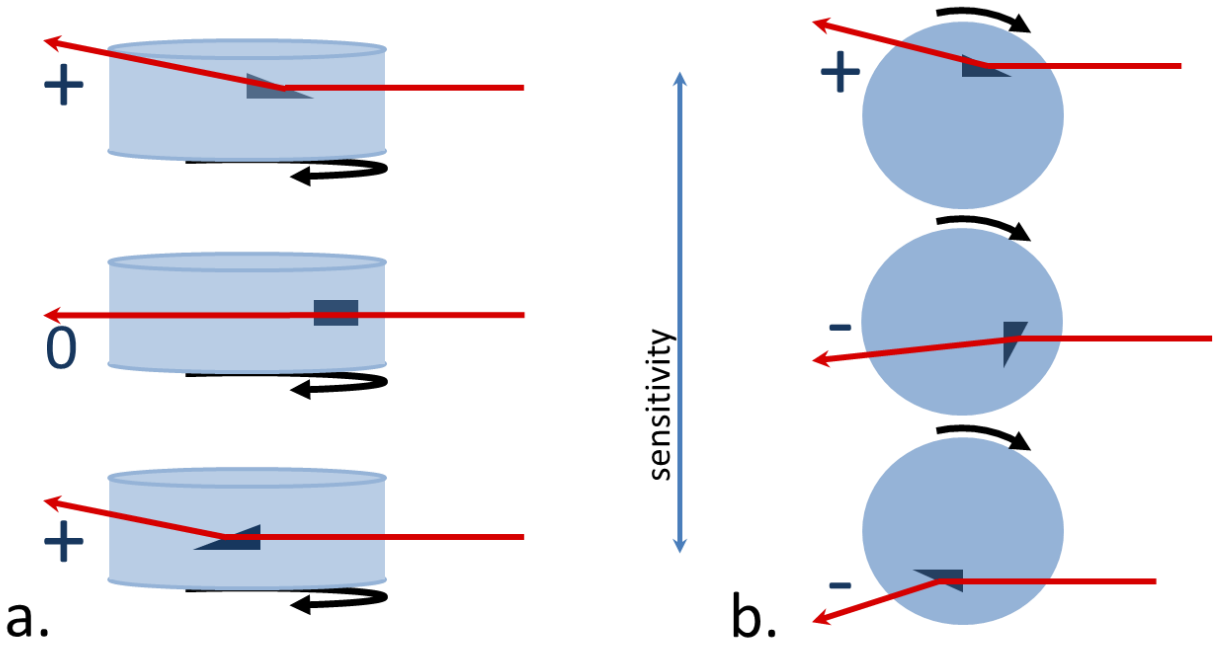

Figure 46: The effect of the direction of axis of rotation with respect to the direction of sensitivity of the imaging setup. Figure a. shows a wedge in the sensitive direction as the sample is rotated about an axis parallel to the direction of sensitivity. The refraction magnitude varies, but the direction does not. Figure b. shows a wedge in the sensitive direction as the sample is rotated about an axis perpendicular to the direction of sensitivity. The refraction will vary in both magnitude and direction as the object is rotated, producing a dataset in which refraction of the beam is non-quantifiable.

about a horizontal axis as it is scanned. The direction of the gradients providing contrast is constantly changing as the object is rotated, so that direction of refraction by a feature in the plane of sensitivity is constantly changing during the scan (Figure 46b).

In conclusion, it is clear that there are several important differences between the information obtained by projection DEI and DEI-CT as foretold by Hounsfield. The key distinction about the DEI refraction image is the somewhat perplexing aspect that the refraction can have plus or minus values that can lead to some confusion and possible misinterpretation in projection images but those issues are addressed by the CT reconstruction. It should be noted that the plus-minus nature of the refraction images is in stark contrast to normal absorption images in which there are no negative values of absorption. However, the power of the CT reconstruction algorithm is that it only requires that the projection images can be represented as the sum of the some property through the object, and refraction certainly meets that criterion in spite of its plus-minus nature.

Reconstruction of DEI-CT datasets

The first challenge addressed is due to the plus-minus nature of refraction imaging concerning reconstruction methods. In absorption imaging, reconstruction of the CT dataset includes taking the negative natural logarithm of the intensity. Recall from equation 2.1 that absorption of x-rays is exponentially related to tissue depth and attenuation coefficient. To make the voxel intensity of the DEI-CT dataset correspond to the attenuation coefficient of the

tissue, the negative natural logarithm of each projection image must be taken over the entire dataset. Equation 2.1 then takes the form

$$-\ln\big(I(x)\big) = \mu x \qquad [4.15]$$

The common filtered backprojection algorithm may then be used to obtain a 3D dataset of the sample. There are many software programs available to perform this reconstruction procedure for absorption images. Implementing DEI-CT to obtain an absorption dataset then is quite simple. The image arithmetic must simply be performed with the two sets of CT data (one set from either side of the rocking curve), to provide a full absorption dataset, and run a routine CT reconstruction algorithm to obtain the 3D dataset.

For refraction images, however, intensity does not correspond exponentially to any property of the tissue being imaged (compare equations 2.7 and 2.15). The intensity of a pixel in a projection is related to the sum of each refraction experienced by that portion of the beam. The relationship is linear, defined by the slope of the rocking curve at the imaging point. This becomes a small, albeit important, consideration in the reconstruction of the *refraction* dataset. Typical CT reconstruction algorithms automatically include a logarithmic calculation to projection intensities before reconstruction. It was therefore important that we obtain a reconstruction program suitable for refraction image reconstruction (one that allowed the logarithmic calculation to be foregone), or write a program for this reconstruction. A few different approaches to reconstruction of DEI-CT datasets can be found in literature (Huang et al., 2006; Huang et al., 2007; M. Wang et al., 2007). The SYRMEP software (Elettra Synchrotron Facility, Italy) was used to reconstruct the datasets from this research.

Comparison of DEI-CT to the current clinical suite

An illustrative comparison of DEI-CT with each of the current clinical suite of imaging tools is as striking a case for the value of this technology for joint research as any description of its advantages in resolution or list of image metrics that might be detailed. The following set of images, Figure 47 to Figure 56, are therefore additionally presented for consideration. Samples were those previously imaged in DEI experiments.

CT images were acquired on a General Electric (GE) Discover CT750 HD 64 multidetector scanner (Waukesha, Wisconsin, USA) in the axial plane (slice thickness 0.625 mm, standard bone and soft tissue and SP filter 2-mm gap and a pitch 0.531:1, 0.4 s rotation time, matrix 512 x 512) with a scan time of 15 seconds. GE software was used to reconstruct sagittal images with a 2mm slice thickness using a bone window (Window Width 200, Window Length 350) and soft tissue window (WW 370, WL 40), with a reconstruction time of less than 5 minutes.

MRI was performed on a Siemens 1.5 Tesla Avanto unit (Siemens Vision, Erlangen, Germany) in the sagittal plane using a 3D DES sequence (Echo Time [TE] 7.28 ms, Repetition time [TR] 19.73 ms; Field of View [FOV] 9.7 x 12. 0 cm; matrix 237 x 320) with a scan time of 5 minutes. Imaging in the coronal plane was also performed using a Proton Density Fat Saturated sequence (Echo Time [TE] 42 ms, Repetition time [TR] 3100 ms; Field of View [FOV] 12.0 x 12. 0 cm; matrix, 224 x 320) with a scan time of 3.5 minutes.

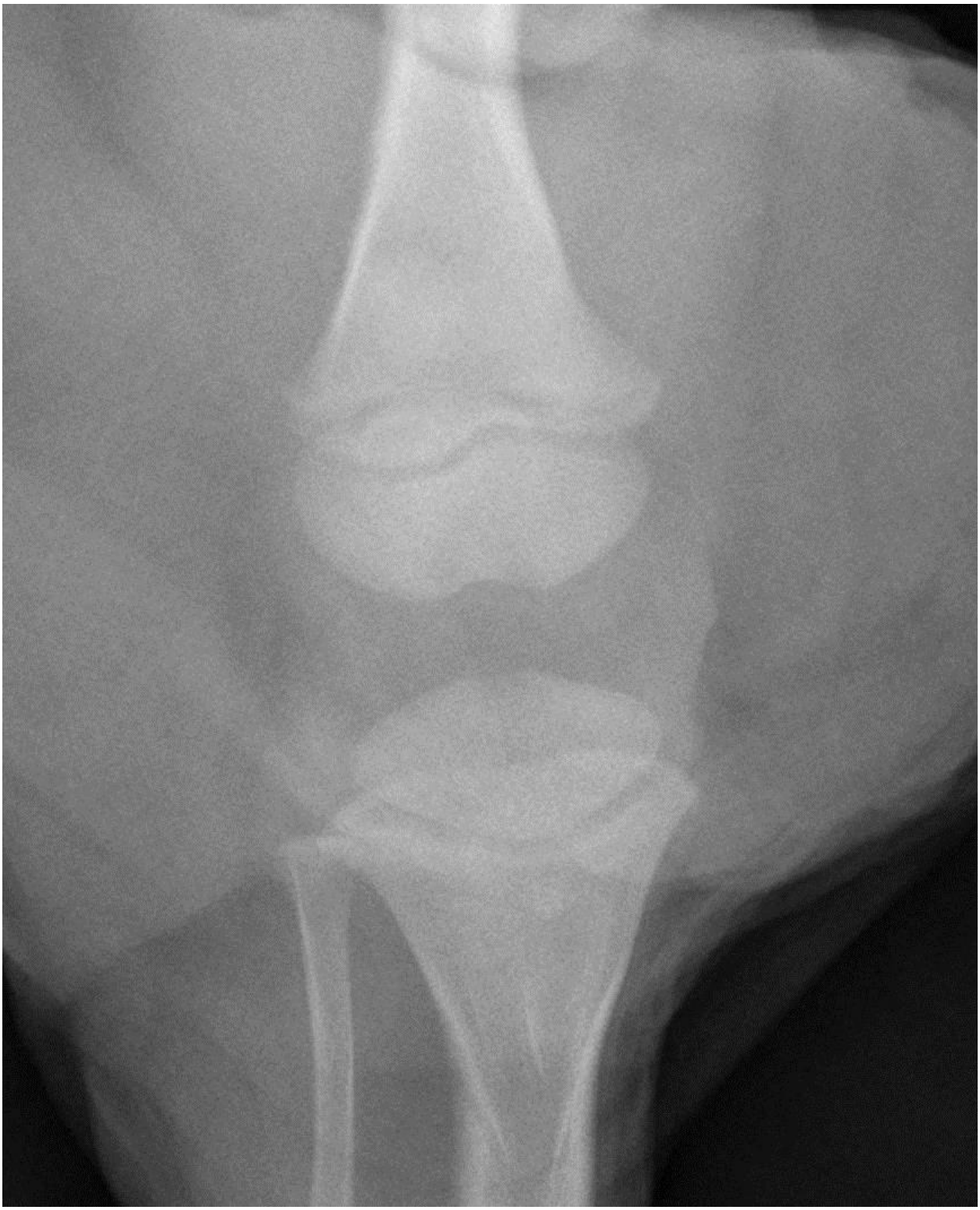

Figure 47: Radiograph of 4 week porcine stifle joint previously imaged at the CLS, coronal view.

Figure 48: Radiograph of 4 week porcine stifle joint previously imaged at the CLS, sagittal view.

Figure 49: CT scan of 4 week porcine stifle joint previously imaged at the CLS, windowed for bone.

Figure 50: CT scan of 4 week porcine stifle joint previously imaged at the CLS, sagittal view windowed for soft tissue.

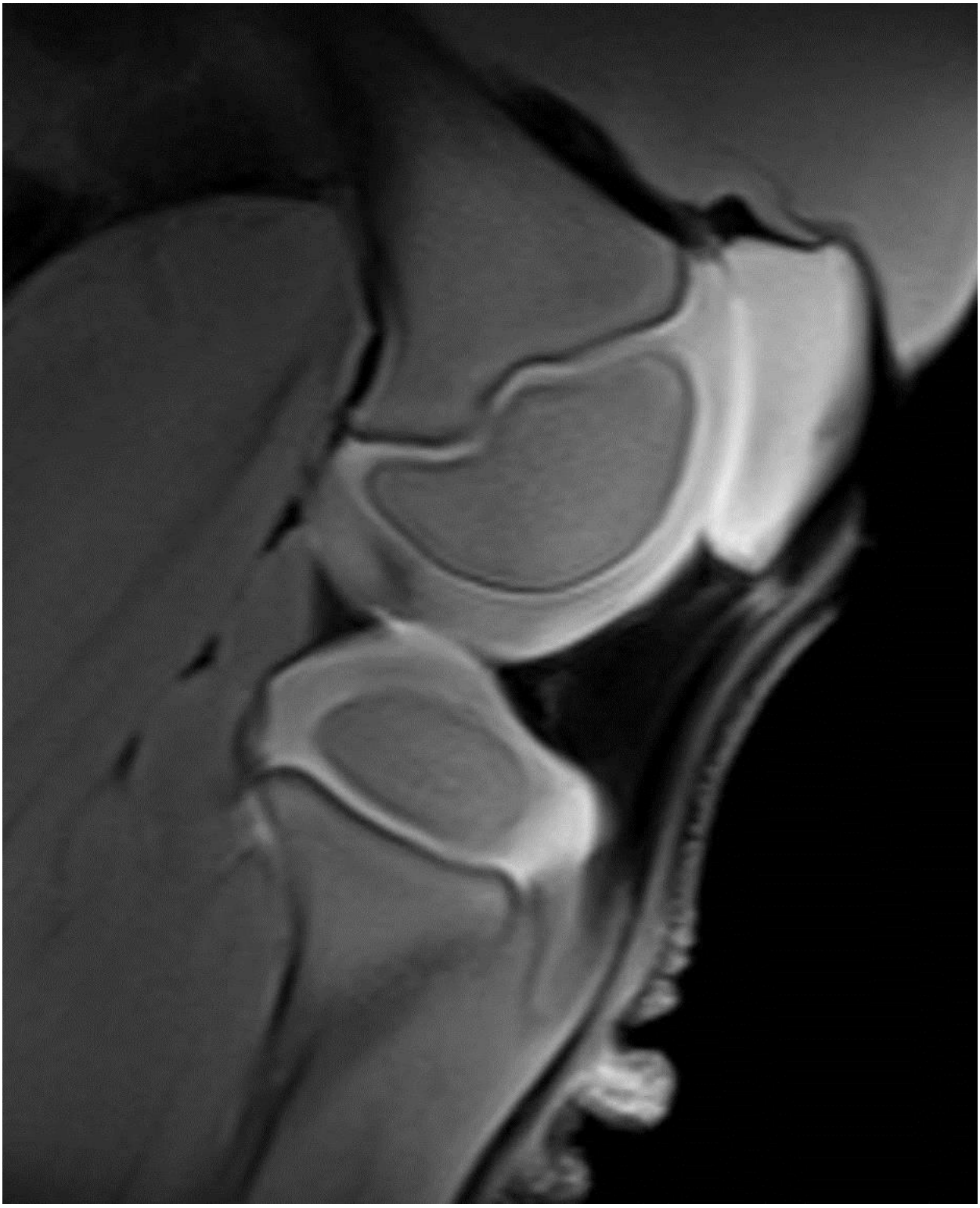

Figure 51: Sagittal MRI image of 4 week porcine stifle joint previously imaged at the CLS.

Figure 52: Coronal view of MRI scan of 4 week porcine stifle joint previously imaged at the CLS.

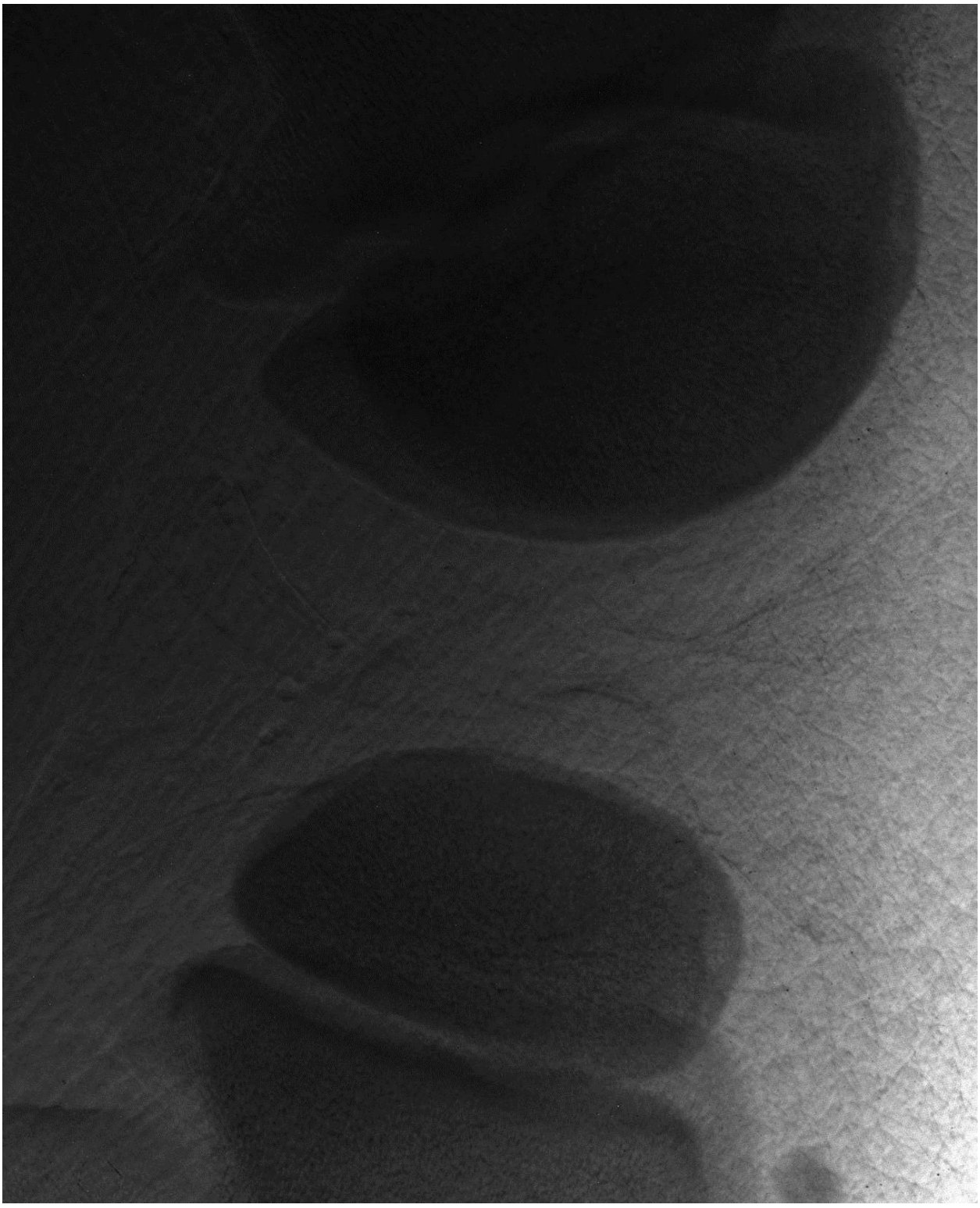

Figure 53: DEI refraction image of 4 week porcine stifle joint, single projection, shown again for convenience of comparison.

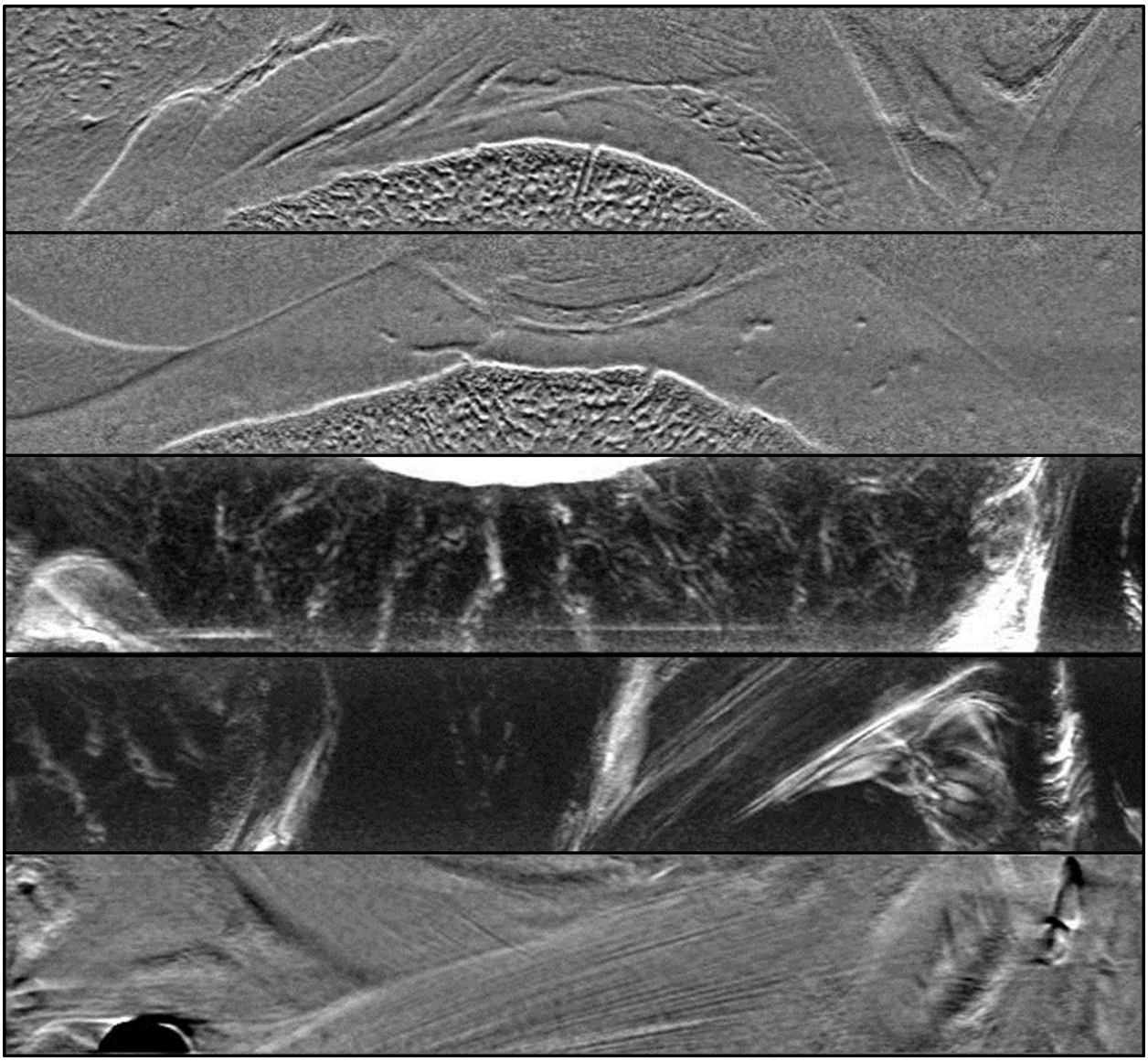

Figure 54: Images from CT DEI refraction datasets, shown again for convenience of comparison. From top to bottom: sagittal slice near the center of the joint; coronal slice displaying the tibial ossification center and femoral and tibial epiphyseal cartilage; standard deviation z-projection through femoral epiphyseal cartilage; standard deviation z-projection through joint ligaments; sum z-projection through cruciate ligaments.

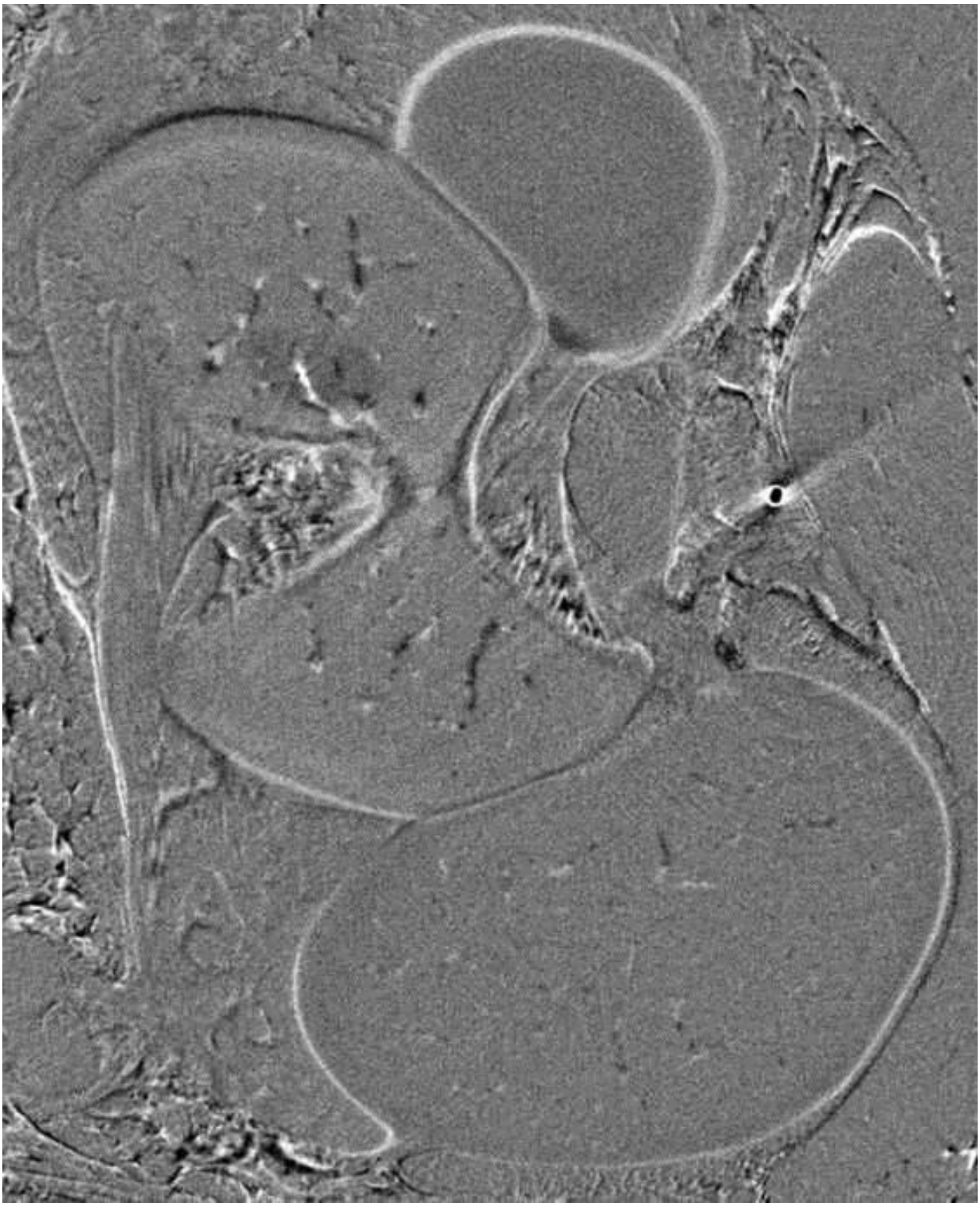

Figure 55: Slice of a CT DEI refraction dataset through the femoral and tibial cartilage, shown again for convenience of comparison.

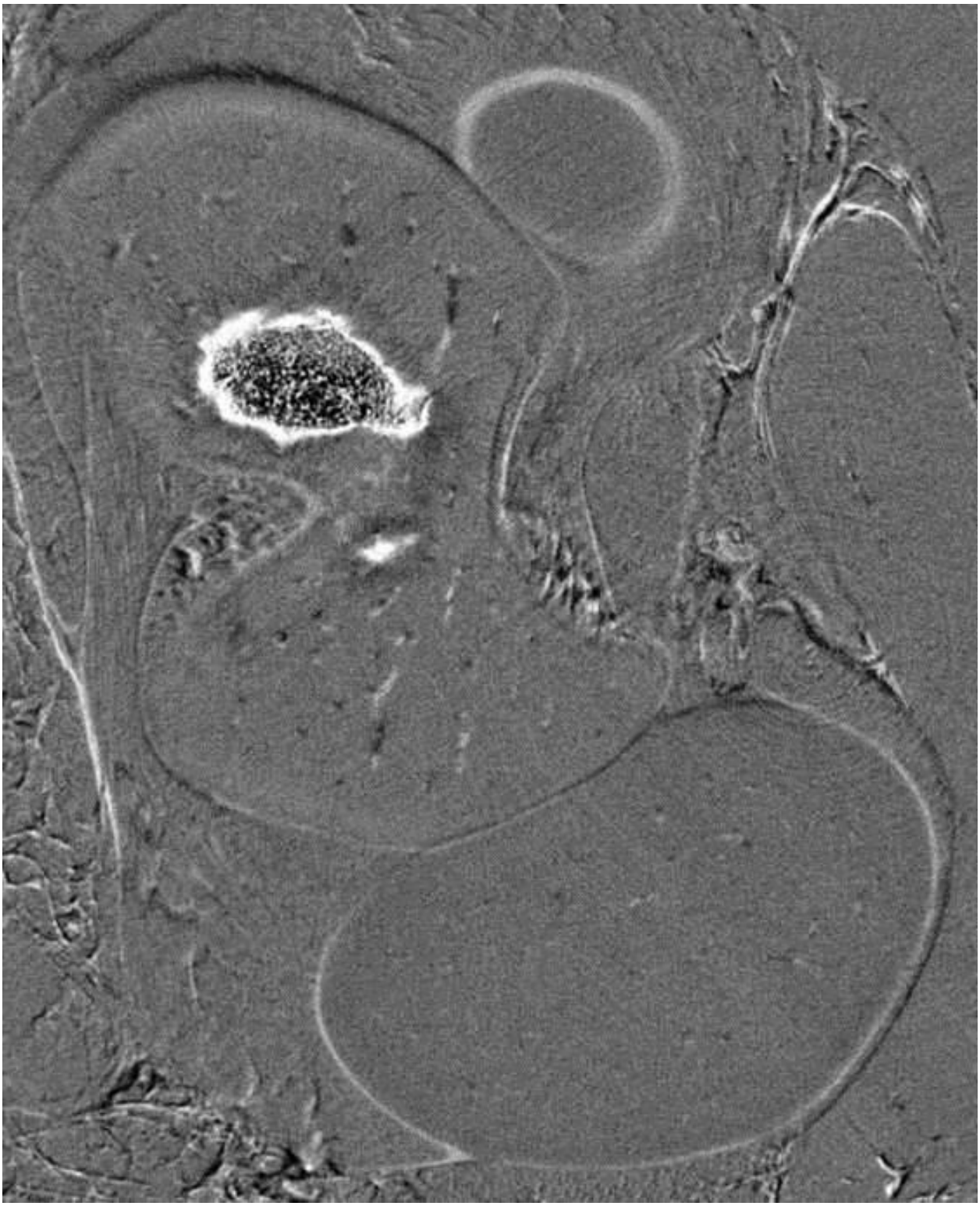

Figure 56: Slice of a CT DEI refraction dataset through the proximal edge of the tibial ossification center, shown again for convenience of comparison.

Conclusion

DEI-CT was successfully implemented for the first time in Canada at the CLS on intact joints at voxel sizes as low as 37.4 µm. Datasets were taken at both the peak and the sides of the rocking curve. 3D Image datasets were reconstructed for refraction images and absorption images. They display high resolution detail of both hard and soft tissues within the joint. Canals were visualized within the growing cartilage and bone structure using the technique.

Future Research

The vasculature visible within this juvenile cartilage provides opportunity for research in exploring how joint disease of juvenile onset affects the cartilage vasculature. Exploration of the relationship of this vasculature to joint maturity may also offer insight into cartilage growth and development, leading to more effective cartilage restoration techniques. It is clear that DEI-CT of growing joints promises new areas of joint research possibilities.

Radiocontrast agents and DEI are another area for future research. They are a contrast medium for *absorption* contrast. They are generally "radiopaque", meaning they highly absorb x-rays. However, typically with DEI-CT the concern is primarily with the refraction images of the dataset, as they contain the most information about the joint. Radiocontrast agents are not designed to maximize refraction, as this is not a source of contrast in clinical scans. One benefit of DEI, though, is that researchers can obtain both an absorption and a refraction dataset from

the same set of scans. It is plausible, then, that a conventional radiocontrast agent might be used to map out vasculature in the absorption dataset, and this overlaid on the refraction dataset, which would be used for further examination of the joint.

If, on the other hand, a *refraction* contrast agent were realized, examination of the vasculature would be straightforward and simple. By the very nature of refraction, this "refraction contrast agent" is not so simple as a radiopaque substance. Since refraction depends upon the density variation *as well as* the angle of interception by the x-rays, it has a shape dependency. Bubbles produce excellent refraction contrast, and certainly any foam solution with small enough bubbles would produce a very high scatter, and consequently, be the equivalent of a "radiopaque" for a refraction image. Micro-bubble solutions are time-dependent, which can be a challenge when either sample preparation or imaging times are long. They are also very low density (by design), which makes it hard to displace a denser fluid with them, such as when injecting the solution through the vasculature of a leg. Vasculature filled with air would also produce excellent contrast, and allow the mapping of the path of vasculature through the joint more easily, particularly through the bone and cartilage.

Information regarding collagen fiber orientation may be obtainable using DEI-CT. Angle sensitive MRI has been used to calculate information on the orientation of collagen fibers within ligaments (Seidel, Hammer, Garnov, Schneider, & Steinke, 2013), and planar DEI has allowed detection of structural orientation within articular cartilage (Muehleman et al., 2004). The inherent directional sensitivity of DEI lends itself to experiments involving fiber orientation. It may be hypothesized that similar, more in-depth information on structural orientation within

cartilage might be obtained from high resolution DEI-CT datasets where the sample is imaged at different angles to the diffraction plane and results compared.

The possibility of performing DEI-CT with a x-ray tube source should also be explored. DEI has been performed with x-ray tubes, utilizing the emission lines of the tubes. One challenge to using x-ray tubes for DEI-CT is that DEI-CT requires many projection scans in a reasonable amount of time. However, it may be possible to produce a usable DEI-CT dataset with fewer and poorer projections than previously thought (Chen, Tang, & Leng, 2008; M. Wang & Yin, 2010). This might allow reasonable scan times even with the greatly reduced flux of an x-ray tube.

Another challenge to tube-based DEI-CT is the stability of the system. For a clinically transferable system (the ultimate goal of a tube-based system), maintaining the orientation of the analyzer crystal to the monochromator angle poses a potential issue. Synchrotron facilities, including the beamline hutches, are carefully designed for maximum mechanical stability. At BMIT, this is reinforced with granite stands for sensitive equipment like the analyzer crystal. Still, mechanical stability alone was not good enough to maintain crystal orientation through DEI-CT scans. However, the feedback control system for analyzer crystal orientation which was implemented shows promise in its performance and robustness (see next chapter). Scans were successfully completed using the control system despite operation of jackhammers by construction crews at CLS roughly 15m away from the analyzer crystal in some of our scans. This system may provide the stability required for scans in a clinical setting.

CHAPTER 5: CONTROL OF THE ANALYZER CRYSTAL ORIENTATION

Introduction

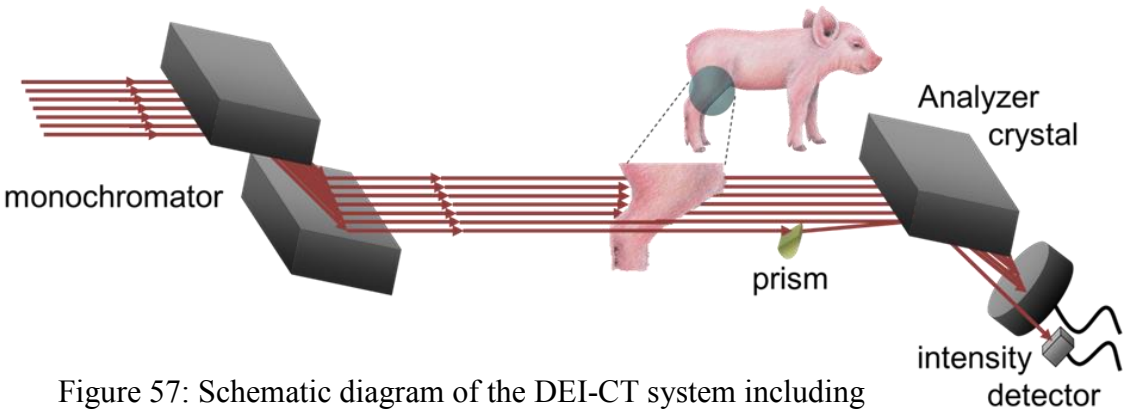

Figure 57: Schematic diagram of the DEI-CT system including the prism and detector used for control of the analyser angle.

This chapter has been adapted from a publication in Journal of Physics: Conference Series (Rhoades, Belev, Rosenberg, & Chapman, 2013).

Apart from typical components of a synchrotron imaging system (source, filters, collimators, detector) DEI usually involves a parallel pair of monochromator crystals and an analyzer crystal, placed downstream from the sample, whose angle is adjusted with respect to the monochromator crystals (Figure 57). The rocking curve produced as the analyzer crystal is rocked in angle with respect to the monochromator crystals forms the basis for DEI (see "Diffraction Enhanced Imaging" section). When an image is taken from one side of this rocking curve, and subtracted from the image taken on the other side of that curve, the result is a completely refraction-based image (no absorption information). Conversely, adding these two

images will produce a completely absorption-based image (no refraction information). Additionally, a single image at the peak of the rocking curve may reveal details that are invisible or obscured in images taken on the sides of the curve. If consistent imaging is desired at each of these points over extended imaging periods, such as is required for high resolution DEI-CT, it must be ensured that the analyzer's angle remains consistent with respect to that of the monochromator over that period. Said another way, one must be able to ensure that we are maintaining the correct position on the rocking curve throughout the imaging period.

CT has proved to be a valuable method with which to use DEI; however, it presents challenges on a completely different scale than does DEI used in projection mode. DEI's dependence on precise crystal orientation means that the stability of both the monochromator and analyzer crystals has a direct and very significant effect on image quality. While this tends to be a somewhat trivial concern for single projection imaging, with sub-minute or even sub-second imaging times, the much longer scan times required for CT imaging dramatize the need for a system that can ensure a stable and accurate crystal orientation for an extended period of time. For example, the experiments described in this thesis, imaging a 4 week piglet stifle joint, fully intact, at 40 microns voxel size require around 2 hours of scan time on each side of the rocking curve. At the CLS synchrotron, the normal storage ring injection schedule would actually allow scan times of up to 12 hours. Researchers wishing to explore the limits of DEI-CT for high resolution studies of larger animals may very well find scan times of this magnitude not only reasonable but necessary in visualizing micron level structures with the relatively large field of view required. At the CLS facility, most of the stability issues are related to long-term drift of the analyzer caused primarily by temperature fluctuations between the monochromator

and analyzer crystals. The fact that the full energy of the unfiltered beam is interacting with the first crystal in the monochromator, while only a very small portion of that beam is incident on the second monochromator crystal, which is further filtered by the sample itself before hitting the analyzer crystal results in significantly different thermal effects on each of these crystals. Despite these differing circumstances, the alignment of these crystals in relation to one another over the full duration of each scan must be maintained. An active feedback system is the natural solution. It is preferable to implement a system such that monitoring and correction of the crystal can occur throughout the scan (rather than stopping the scan at certain increments for correction), without interfering with the imaging taking place.

This type of feedback control system is simply implemented for imaging on the straight sides of the rocking curve. While on the high angle side of the curve, the response is to increase the analyzer crystal's angle if intensity increases, and decrease the angle if the intensity drops, thereby maintaining the system's position on the rocking curve (Krolzig, Materlik, Swars, & Zegenhagen, 1983). When imaging on the low angle side of the curve, response would be the opposite, such that response to a decrease in intensity would be to increase analyzer crystal angle, and vice versa. Because the storage ring current in a synchrotron facility like the CLS is not constant, but steadily decreasing between injections, this system should have a means of adjusting for decrease of the incoming beam flux over time, such that the position on the curve is maintained, rather than simply the beam's absolute intensity. In addition, the intensity measurements should be made from a portion of the beam not interacting with the sample, such that sample movement and rotation during the scan does not affect the feedback system. All of this is quite simply implemented with minimal additional hardware and software. While

this describes a control system adequate for imaging on the sides of the rocking curve, this system breaks down when exploitation of different areas of the curve is desired, particularly the peak and the tails. At the peak of the rocking curve, any change in angle results in a reduction in intensity, and the necessary response of the system cannot be known without additional information. At the tails of the curve, both intensity and slope are approaching zero, limiting feedback responsiveness.

Methods have been previously proposed to deal with this dilemma. One is to put a periodic signal on the angle of the analyzer crystal and look for frequency doubling in the intensity as the peak is crossed from one side to the other (Mills & Pollock, 1980). This system allows the control system to detect in which direction the crystal drift is occurring, and proceed with the appropriate correction. Unfortunately, it does so at the cost of introducing a signal on the rocking curve position, such that there is now some degree of artificial intensity variation in the system. Another control system solution is to respond to intensity drop by adjusting the angle in a "default" direction and check the outcome. The control system will then continue in the same direction if intensity is increased by the angle change, or change the direction of crystal adjustment if the intensity drops due to the original correction. While this system presents a simple and straightforward investigation of the correction need, its process inevitably adds to response delay, and often *increases* crystal misalignment before correcting it. We present a novel method of dealing with the issue that allows the control system to lock on to the optimum portion of the curve for controlling, while imaging at some other point along the curve. This allows the control system to operate on the optimum portion of the curve for feedback, while imaging at practically *any* desired location – the sides, the peak, or the tails. We

chose the “half peak” as the optimum point at which to operate the control system. The half peak is the point on either side of the rocking curve that has half of the peak’s maximum intensity.

This method utilizes a half-round prism (Figure 58, Figure 59) to refract a portion of the beam (hereafter referred to as the control beam), which is then diffracted by the analyzer and

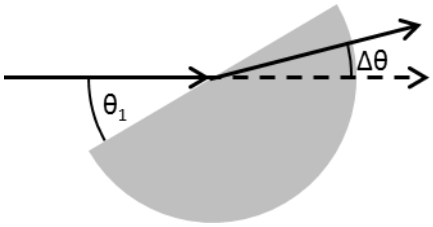

Figure 58: Schematic of the “refractor” used to angularly displace a horizontal segment of the beam to form the control beam.

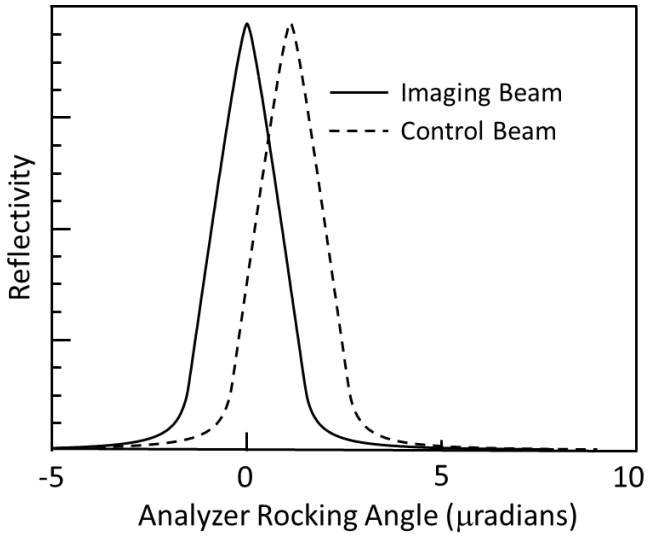

Figure 59: Rocking curve showing the angular shift between the imaging beam with no object and the “refracted” control beam.

recorded by a simple intensity detector (refer to Figure 57). By adjusting the angle of the prism with respect to the incoming beam, operators can adjust how much the control beam peak is “kicked off” the imaging beam (Bewer & Chapman, 2010; Zhong et al., 2002). The prism is adjusted such that one of the half peaks of the control beam is aligned with the desired point of imaging on the imaging beam curve.

Methods

Using an angle point close to the peak of the rocking curve to control the feedback system makes it susceptible to crystal drift over the peak, which the system would respond to by driving crystal orientation in the wrong direction. However, the lower the control point is, the less intensity there is for the control detector, and eventually, the less slope there is for it to respond to. The straight portions of the curve near the half peaks are therefore optimum from a control standpoint.

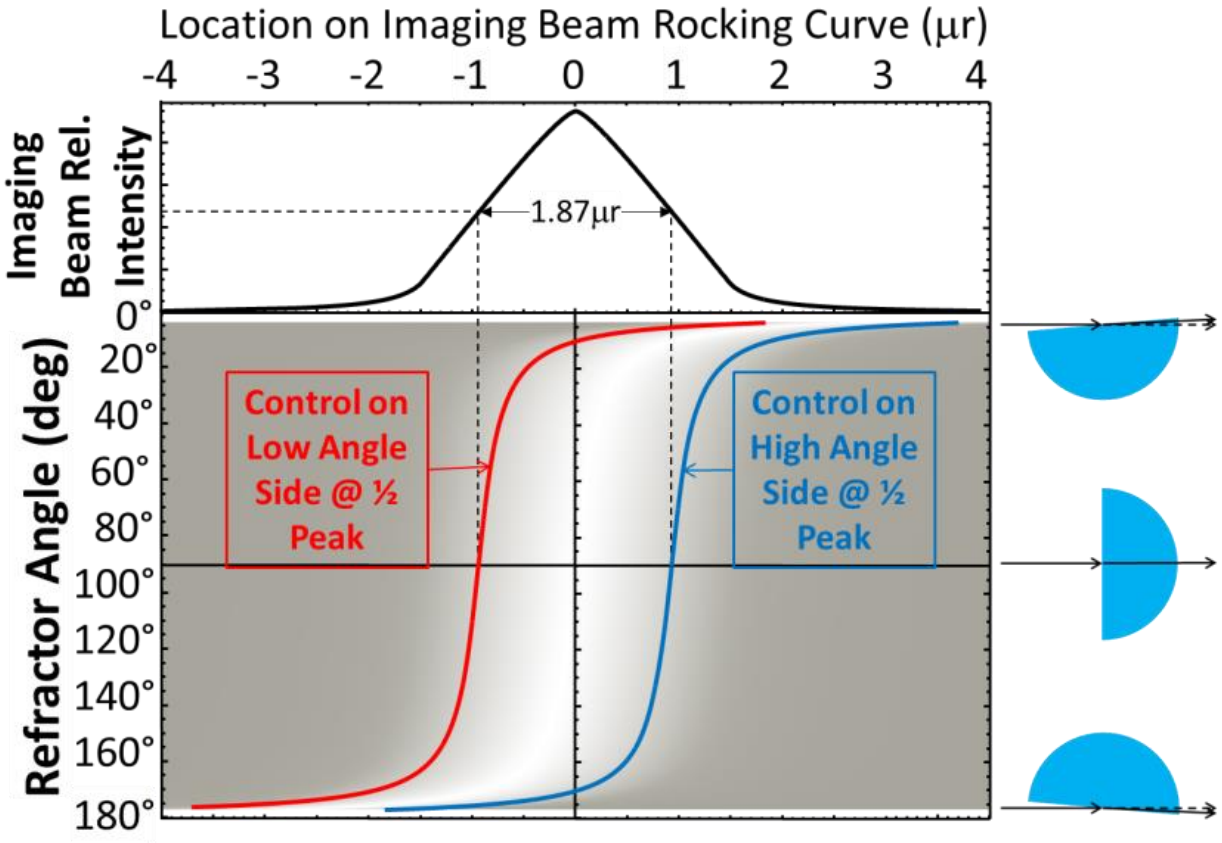

Figure 60: Diagram of the control beam rocking curve position vs. refractor angle. The control beam rocking curve is demonstrated by the intensity level in the lower region of the diagram.

By refracting the control beam half of a Darwin width (one quarter the ideal width of the rocking curve), one of the half maximum points of the control beam is placed on the peak of the imaging beam. This allows one to lock on to the half peak of the control beam overlapping the imaging beam curve, and the imaging beam will be effectively locked on to the peak. Drifting off the peak of the imaging beam will be seen by the control system as a drift from the half peak of the control beam, and thereby corrected efficiently (Figure 60). Secondly, if the prism face is set normal to the beam, the control beam and imaging beams align, and the system can be used to lock on to portions of the imaging curve near the half peaks. Thirdly, if the original prism orientation is retained and the control system is locked on to the opposite side of the control beam peak (the half peak farthest from the imaging beam peak), imaging may be done in the "tails" of the imaging peak, where low intensity and low slope would otherwise limit feedback response. As at the peak, drift from the desired point on the tail of the imaging beam rocking curve is seen by the control system as drift away from the half peak of the control beam rocking curve. Increasing the amount of refraction of the control beam will allow imaging even further out into the "tails" of the curve; even with fairly small prisms, this allows imaging at several Darwin widths on either side of the peak. The maximum angular difference possible between the imaging beam peak and the control beam peak is dependent on the dimensions of the prism. Smaller angle of incidence between the incoming beam and the prism face will produce greater refraction by the prism, and, therefore, a greater angular displacement of the control beam peak. However, rather than using an unreasonably large prism when imaging farther out into the tails is desired, a second prism, or a thin sheet of scattering material placed upstream of the prism, widening the control peak, may be used. Inserting a second prism will

additively refract the control beam, doubling the maximum range of the control system. A sheet of scattering material placed in the control beam will widen the control beam, pushing its half peak points farther from its own peak, again providing increased distance between the half peak used for control and the peak of the imaging curve (Figure 61). This control system, then, allows exploitation of all three areas of the curve: the peak, the sides, and far out into the tails.

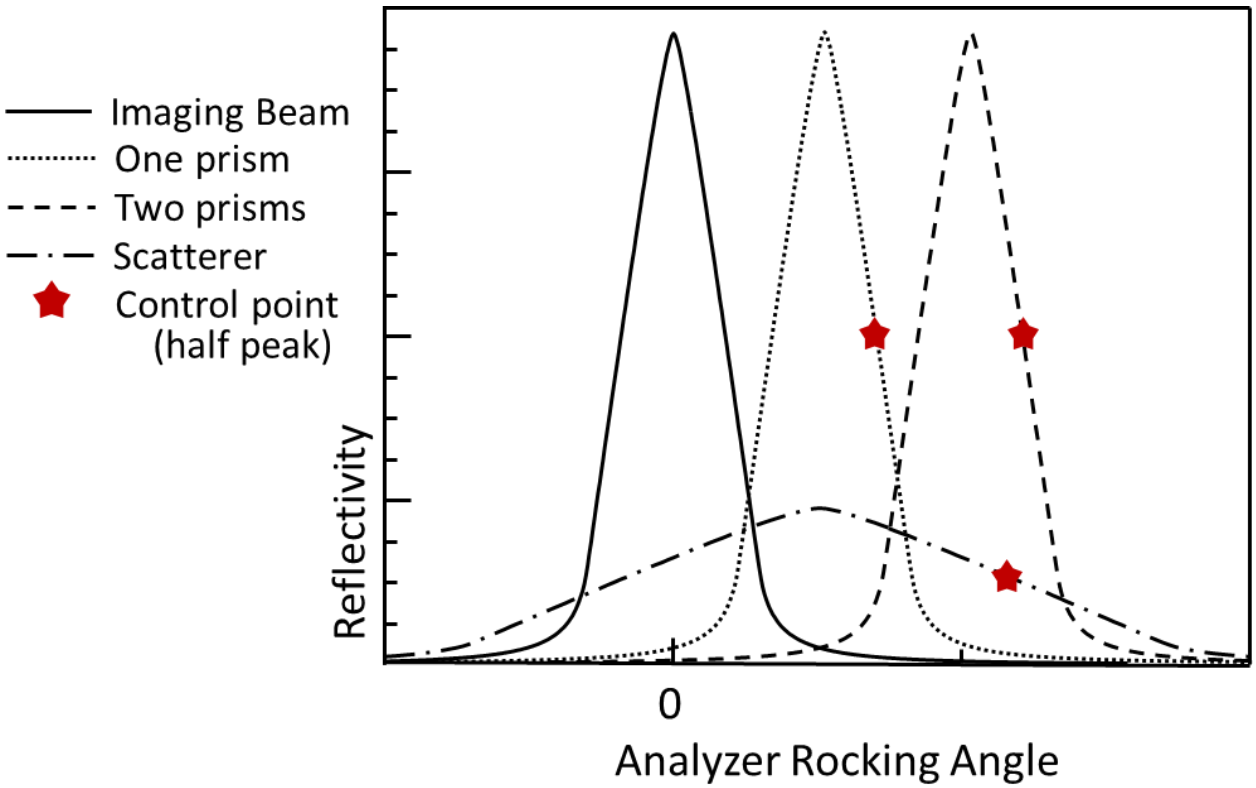

Figure 61: Plot displaying variations on the single prism control system to allow imaging farther into the tails of the imaging beam. Refraction of the control beam by a single prism, two prisms in series, and a single prism in combination with a scatterer placed in the control beam are each shown. The half peak control point of each scenario is demonstrated by a star on the curve representing that scenario.

It may be noticed from Figure 60 that it takes a relatively large change in prism angle to produce a noticeable change in the amount of refraction of the control beam. While the imaging system is extremely sensitive to changes in the analyzer crystal's orientation, the

feedback system is very robust in terms of slight changes in the angle of the prism. The whole imaging system has, therefore, two components dependent upon angle, viz., the analyzer and the prism, one to which the system is very sensitive, controlled by a feedback system very robust in terms of the angle of the other.

Results

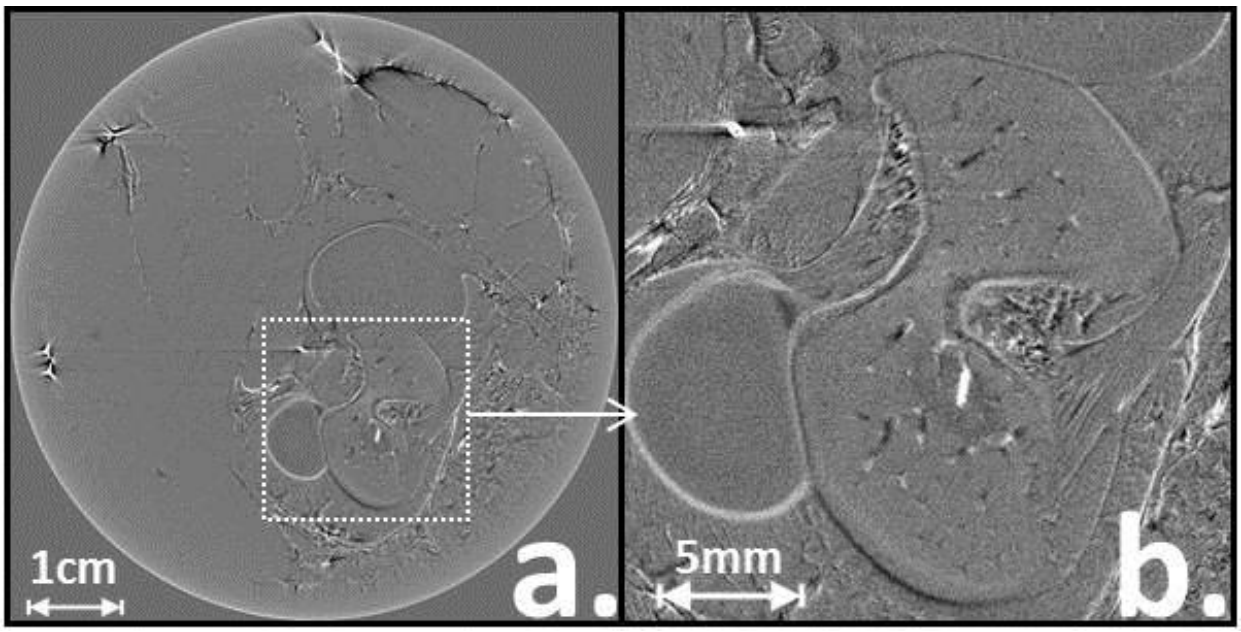

Figure 62: Slices through the femoral and tibial epiphyseal cartilage of fully intact 4 week porcine stifle joint from a DEI-CT refraction dataset.

DEI-CT were taken of a 4 week porcine stifle joint with a Photonic Science detector (fov of 72x72mm; 18.7 µm pixel size). 2501 projections at a 2s exposure time were used. Si (4,4,0) reflection at 40keV interrogated the 65mm sample, mounted in a cylindrical acrylic plastic holder. Imaging time at the peak of the curve was approximately 1hr 20 min. The feedback system recorded a total correction of more than a Darwin width throughout the length of the

scan. Similarly, a scan near the half peaks of the imaging curve with the same setup, but a 3s exposure time (approx. 2 hours scan time) once again yielded a correction of more than a Darwin width. An example from the CT data set is shown in Figure 62.

Conclusion

A refractor based DEI control system was successfully implemented and tested at the Biomedical Imaging and Therapy bend magnet beamline at the CLS. This system allows full control of the analyzer setting over several Darwin widths of angular placement relative to the imaging beam including the peak location and has enabled long scan times, such as required for high-resolution CT, without relying on mechanical stability. Future work might include an ultra-small angle scatterer (i.e. paper) or multiple prisms to expand the usable range into the far wings of the imaging beam.

CHAPTER 6: FINAL CONCLUSION

In summary, the objective of this research project was the development of DEI for high resolution visualization of hard and soft tissues in growing joints. In meeting this objective, it was necessary to implement CT in conjunction with DEI. It was also necessary to develop and implement a control system to precisely maintain the angle of the analyzer crystal for extended periods. The testing of planar DEI at the CLS for joints, implementation of a novel analyzer crystal control system, and the development and testing of DEI-CT at the CLS, therefore, dovetailed to form the basis of this thesis' research.

The basic conclusion of the single projection DEI experiments is that the visibility of soft tissue structures is quite limited, and detail at the level desired is not visible in intact joints. It is apparent that a large part of the problem is the overlying contrast from tissue interfaces at different depths than the joint. 2D superimposition is clearly a much larger issue in refraction images which captures contrast from soft tissues than in traditional absorption x-ray imaging, in which most of the tissues at different depths (e.g. skin, muscle, and connective tissue) produces little to no perceptible contrast in the image.

DEI-CT experiments, the first in Canada, display that DEI-CT at the CLS provides a quantifiable, three-dimensional image of bone and soft tissue at a resolution on the order of microns in growing porcine stifle joints. As a result of this project, DEI-CT is now available to other researchers at BMIT, with minimal setup time, and has already been implemented in other research projects. The development of this high resolution imaging system, providing excellent contrast for both hard and soft tissues, fills an important gap in the suite of imaging

modalities available to the researcher, particularly in examining joint diseases. DEI-CT at the CLS synchrotron has demonstrated a dramatic increase in soft tissue contrast over conventional x-ray imaging and CT, in images with voxel sizes as low as 37.4 microns, and in resolution compared to MRI. This improvement highlights DEI-CT as a new imaging modality for musculoskeletal research.

The novel analyzer control system developed in this research allows the analyzer to be set at any location in the analyzer rocking curve, including the peak location. The method described can be extended to include protocols that expand the range of analyzer control to several Darwin widths away from the analyzer peaked location. Such a system is necessary for the accurate implementation of DEI-CT and is intended to make analyzer-based imaging simpler without relying on repeated alignment during the imaging session. This control system expands the opportunity for experiments in the lower portions of the rocking curve, as well as experiments that require longer scan times. Future work might include an ultra-small angle scatterer (i.e. paper) or multiple prisms to expand the usable range even farther into the wings of the imaging beam.

The vasculature visualized within juvenile cartilage in this research provides opportunity for future exploration of how joint diseases of juvenile onset affects the cartilage vasculature. Exploration of the relationship of this vasculature to joint maturity may also offer insight into cartilage growth and development, leading to more effective cartilage restoration techniques. Future research might also include testing the ability of DEI-CT to detect collagen fiber orientation. The inherent directional sensitivity of DEI lends itself to experiments involving fiber orientation.

REFERENCES

Als-Nielsen, J., McMorrow, D. (2011). Elements of Modern X-ray Physics: Wiley.

Arthritis Foundation. (2013). from http://www.arthritis.org/

Authier, A. (2004). Dynamical Theory of X-ray Diffraction: Oxford University Press.

Babyn, P., Kim, H., Lemaire, C., Gahunia, H., Cross, A., DeNanassy, J., Pritzker, K. (1996). High-resolution magnetic resonance imaging of normal porcine cartilaginous epiphyseal maturation. Jmri-Journal of Magnetic Resonance Imaging, 6(1), 172-179. doi: 10.1002/jmri.1880060131

Barnewolt, C., Shapiro, F., Jaramillo, D. (1997). Normal gadolinium-enhanced MR images of the developing appendicular skeleton: Part I. Cartilaginous epiphysis and physis. American Journal of Roentgenology, 169(1), 183-189. doi: 10.2214/ajr.169.1.9207522

Bewer, B., Chapman, L. D. (2010). Development of an X-ray Prism for Analyzer Based Imaging Systems. Rev Sci Instrum, 81.

Björn, J. (2010). Front Matter Semiconductor Radiation Detection Systems (pp. i-xii): CRC Press.

Bombardier, C., Hawker, G., Mosher, D. (2011). The impact of arthritis in Canada: today and the next 30 years. Toronto: Arthritis Foundation.

Bragg, W., Bragg, W. (1913). The reflection of X-rays by crystals. Proceedings of the Royal Society of London Series a-Containing Papers of a Mathematical and Physical Character, 88(604), 428-428.

Brankov, J., Wernick, M., Yang, Y., Li, J., Muehleman, C., Zhong, Z., Anastasio, M. (2006). A computed tomography implementation of multiple-image radiography. Medical Physics, 33(2), 278-289. doi:http://dx.doi.org/10.1118/1.2150788

Bravin, A., Coan, P., & Suortti, P. (2013). X-ray phase-contrast imaging: from pre-clinical applications towards clinics. Physics in Medicine and Biology, 58(1), R1.

Bravin, A., Fiedler, S., Thomlinson, W. (2002). Very low dose mammography: New perspectives in Diffraction Enhanced Imaging (DEI) mammography, San Diego, CA, United states.

Bravin, A., Keyriläinen, J., Fernández, M., Fiedler, S., Nemoz, C., Karjalainen-Lindsberg, M., . . . Suortti, P. (2007). High-resolution CT by diffraction-enhanced x-ray imaging: mapping of breast tissue samples and comparison with their histo-pathology. Physics in Medicine and Biology, 52(8), 2197.

Burghardt, A., Link, T., Majumdar, S. (2011). High-resolution Computed Tomography for Clinical Imaging of Bone Microarchitecture. Clinical Orthopaedics and Related Research®, 469(8), 2179-2193. doi: 10.1007/s11999-010-1766-x

Carballido-Gamio, J., Joseph, G., Lynch, J., Link, T., Majumdar, S. (2011). Longitudinal analysis of MRI T2 knee cartilage laminar organization in a subset of patients from the osteoarthritis initiative: A texture approach. Magnetic Resonance in Medicine, 65(4), 1184-1194. doi: 10.1002/mrm.22693

Cecil, R., Goldman, L., Schafer, A. (2012). Goldman's Cecil medicine. Philadelphia: Elsevier/Saunders/.

Chapman, L. D., Thomlinson, W., Arfelli, F., Gmur, N., Zhong, Z., Menk, R., . . . Sayers, D. (1996). Mammography imaging studies using a Laue crystal analyzer. Review of Scientific Instruments, 67(9 [+CD-ROM]), 5 pp.

Chapman, L. D., Thomlinson, W., Johnston, R. E., Washburn, D., Pisano, E., Gmur, N., . . . Sayers, D. (1997). Diffraction enhanced x-ray imaging. Phys Med Biol, 42(11), 2015-2025.

Chapman, L. D., Chen, X., Cooper, D., Schreyer, D., Zhu, N. (2011). X-ray diffraction enhanced imaging as a novel method to visualize low-density scaffolds in soft tissue engineering. Tissue Engineering, Part C: Methods, 17, 1071+.

Chen, G., Tang, J., Leng, S. (2008). Prior image constrained compressed sensing (PICCS): a method to accurately reconstruct dynamic CT images from highly undersampled projection data sets. Med Phys, 35(2), 660-663.

Christensen, C., Chapman, L. D., Sidhu, N. (2005). The BioMedical Imaging and Therapy Beamline at the Canadian Light Source Inc. Medical Physics, 32(7), 2416-2416.

CLS. (2015). What is a Synchrotron. Retrieved 19 May, 2015, from http://www.lightsource.ca/education/whatis.php

Connor, D., Benveniste, H., Dilmanian, F., Kritzer, M., Miller, L., Zhong, Z. (2009). Computed tomography of amyloid plaques in a mouse model of Alzheimer's disease using diffraction enhanced imaging. Neuroimage, 46(4), 908-914. doi: 10.1016/j.neuroimage.2009.03.019

Connor, D., Pisano, E., Cole, E., Zhong, Z., Dilmanian, F., Parham, C., . . . Suortti, P. (2011). Translation of Synchrotron-based Research into the Clinic: Assessing the Current

Clinical Potential of Diffraction Enhanced Imaging. Synchrotron Radiation News, 24(2), 29-33. doi: 10.1080/08940886.2011.567166

Coolidge, W. (1916). USA Patent No. 1203495: USPTO.

Cooper, D., Bewer, B., Wiebe, S., Wysokinski, T., Chapman, L. D. (2011). Diffraction Enhanced X-ray Imaging of the Distal Radius: A Novel Approach for Visualization of Trabecular Bone Architecture. Canadian Association of Radiologists Journal-Journal De L Association Canadienne Des Radiologistes, 4, 251-255. doi: S0846-5371(10)00117-8 [pii]
10.1016/j.carj.2010.04.015

Cooper, D., Bewer, B., Wiebe, S., Belev, G., Wysokinski, T., Chapman, L. D. (2011). Preliminary Bone Imaging on 05B1-1 Beamline at the Canadian Light Source: Exploration of Diffraction Enhanced Imaging. Synchrotron Radiation News, 24(2), 13-18. doi: 10.1080/08940886.2011.567163

Cullity, B., Stock, S. (2001). Elements of X-ray Diffraction: Prentice Hall.

Dilmanian, F., Zhong, Z., Ren, B., Wu, X., Chapman, L. D., Orion, I., Thomlinson, W. (2000). Computed tomography of x-ray index of refraction using the diffraction enhanced imaging method. Phys Med Biol, 45(4), 933-946.

Dong, L., Li, J., Jian, W., Zhang, L., Wu, M., Shi, H., Luo, S. (2014). Emphysema early diagnosis using X-ray diffraction enhanced imaging at synchrotron light source. BioMedical Engineering OnLine, 13, 82-82. doi: 10.1186/1475-925X-13-82

Duan, J., Hu, C., Luo, S., Zhao, X., Wang, T. (2013). Microcomputed Tomography with Diffraction-Enhanced Imaging for Morphologic Characterization and Quantitative

Evaluation of Microvessel of Hepatic Fibrosis in Rats. PLoS ONE, 8(10), e78176. doi: 10.1371/journal.pone.0078176

Duyn, J. H. (2012). The future of ultra-high field MRI and fMRI for study of the human brain. NeuroImage, 62(2), 1241-1248. doi: http://dx.doi.org/10.1016/j.neuroimage.2011.10.065

Faulconer, L., Parham, C., Connor, D., Zhong, Z., Kim, E., Zeng, D., . . . Pisano, E. (2009). Radiologist Evaluation of an X-ray Tube-Based Diffraction-Enhanced Imaging Prototype Using Full-Thickness Breast Specimens. Academic Radiology, 16(11), 1329-1337. doi: http://dx.doi.org/10.1016/j.acra.2009.05.006

Faulconer, L., Pisano, E., University of North Carolina at Chapel Hill. Dept. of Biomedical Engineering. (2009). Evaluation of a diffraction-enhanced imaging DEI prototype and exploration of novel applications for clinical implementation of DEI (pp. 1 electronic text PDF (6.12 MB)). Retrieved from http://dc.lib.unc.edu/u?/etd,3432

Fazel, R., Krumholz, H., Wang, Y., Ross, J., Chen, J., Ting, H., . . . Nallamothu, Brahmajee K. (2009). Exposure to Low-Dose Ionizing Radiation from Medical Imaging Procedures. New England Journal of Medicine, 361(9), 849-857. doi: doi:10.1056/NEJMoa0901249

Fogarty, D., Reinhart, B., Tzvetkov, T., Nesch, I., Williams, C. (2011). In-Laboratory Diffraction-Enhanced X-Ray Imaging of an Equine Hoof. Journal of Equine Veterinary Science, 31(7), 365-369. doi: 10.1016/j.jevs.2011.03.015

Friedrich, W., Knipping, P., Laue, M. (1912). Interference phenomena with Rnigen rays. Konigliche Bayerische Akademie der Wissenschaften, Sitzungsberichte (Mathematisch-Physikalische Klasse), 303-322.

Frush, D. (2008). Pediatric dose reduction in computed tomography. Health Phys, 95(5), 518-527. doi: 10.1097/01.hp.0000326335.34281.63

Gold, G., Chen, C., Koo, S., Hargreaves, B., Bangerter, N. (2009). Recent Advances in MRI of Articular Cartilage. American Journal of Roentgenology, 193(3), 628-638. doi: 10.2214/AJR.09.3042

Hammond, C. (2009). The Basics of Crystallography and Diffraction: OUP Oxford.

Hasnah, M., Parham, C., Pisano, E., Zhong, Z., Oltulu, O., Chapman, L. D. (2005). Mass density images from the diffraction enhanced imaging technique. Med Phys, 32(2), 549-552.

Haug, E., Nakel, W. (2004). The elementary process of Bremsstrahlung. River Edge, NJ: World Scientific.

Hegenscheid, K., Puls, R., Rosenberg, C. (2012). Bildgebungsstrategie bei Kniegelenkverletzungen. Der Radiologe, 52(11), 980-986. doi: 10.1007/s00117-012-2411-3

Hounsfield, G. (1980). Nobel Award address. Computed medical imaging. Med Phys, 7(4), 283-290.

Huang, Z., Kang, K., Li, Z., Zhu, P., Yuan, Q., Huang, W., . . . Yu, A.. (2006). Direct computed tomographic reconstruction for directional-derivative projections of computed

tomography of diffraction enhanced imaging. Applied Physics Letters, 89(4), 041124. doi: http://dx.doi.org/10.1063/1.2219405

Huang, Z., Zhang, L., Kang, K., Chen, Z., Zhu, P., Yuan, Q., Huang, W. (2007). Local reconstruction in computed tomography of diffraction enhanced imaging. Applied Physics Letters, 91(1), 011117. doi: http://dx.doi.org/10.1063/1.2749427

Izadifar, Z., Chapman, L. D., Chen, X. (2014). Computed tomography diffraction-enhanced imaging for in situ visualization of tissue scaffolds implanted in cartilage. Tissue Eng Part C Methods, 20(2), 140-148. doi: 10.1089/ten.TEC.2013.0138

Jackson, P., Cockcroft, P. (2007). Handbook of Pig Medicine: Saunders Elsevier.

Jaramillo, D., Villegas-Medina, O., Doty, D., Rivas, R., Strife, K., Dwek, J., . . . Shapiro, F. (2004). Age-Related Vascular Changes in the Epiphysis, Physis, and Metaphysis: Normal Findings on Gadolinium-Enhanced MRI of Piglets. American Journal of Roentgenology, 182(2), 353-360. doi: 10.2214/ajr.182.2.1820353

Johnson, K., Wittkop, B., Haigh, F., Ryder, C., Gardner-Medwin, J. (2002). The early magnetic resonance imaging features of the knee in juvenile idiopathic arthritis. Clin Radiol, 57(6), 466-471. doi: 10.1053/crad.2001.0876

Johnson, K., Gardner-Medwin, J. (2002). Childhood Arthritis: Classification and Radiology. Clinical Radiology, 57(1), 47-58. doi: http://dx.doi.org/10.1053/crad.2001.0732

Johnston, R., Washburn, D., Pisano, E., Burns, C., Thomlinson, W., Chapman, L. D., . . . Sayers, D. (1996). Mammographic phantom studies with synchrotron radiation. Radiology, 200(3), 659-663. doi: 10.1148/radiology.200.3.8756911

Keyriläinen, J., Fernandez, M., Karjalainen-Lindsberg, M., Virkkunen, P., Leidenius, M., Von Smitten, K., . . . Bravin, A. (2008). Toward high-contrast breast CT at low radiation dose1. Radiology, 249(1), 321-327. doi: 10.1148/radiol.2491072129

Kirkhus, E., Flato, B., Riise, O., Reiseter, T., Smith, H. (2011). Differences in MRI findings between subgroups of recent-onset childhood arthritis. Pediatr Radiol, 41(4), 432-440. doi: 10.1007/s00247-010-1897-y

Knoll, G. (1989). Radiation detection and measurement: Wiley.

Krolzig, A., Materlik, G. , Swars, M., Zegenhagen. (1983). A Feedback Control System for Synchrotron Radiation Double Crystal Instruments. Nuclear Instruments and Methods in Physics Research, 208(1), 613-619.

Lee, K., Masi, J., Sell, C., Schier, R., Link, T., Steinbach, L., . . . Majumdar, S. (2005). Computer-aided quantification of focal cartilage lesions using MRI: Accuracy and initial arthroscopic comparison. Osteoarthritis and Cartilage, 13(8), 728-737. doi: http://dx.doi.org/10.1016/j.joca.2005.03.007

Li, H., Zhang, L., Wang, X., Wang, T., Wang, B., Zhao, X., Luo, S. (2009). Investigation of hepatic fibrosis in rats with x-ray diffraction enhanced imaging. Applied Physics Letters, 94(12). doi: 10.1063/1.3104860

Li, J., Zhong, Z., Connor, D., Mollenhauer, J., & Muehleman, C. (2009). Phase-sensitive X-ray imaging of synovial joints. Osteoarthritis Cartilage, 17(9), 1193-1196. doi: 10.1016/j.joca.2009.03.005

Li, J., Zhong, Z., Lidtke, R., Kuettner, K., Peterfy, C., Aliyeva, E., Muehleman, C. (2004). Radiography of Soft Tissue of the Foot and Ankle with Diffraction Enhanced Imaging.

Journal of the American Podiatric Medical Association, 94(3), 315-322. doi: 10.7547/0940315

Malattia, C., Damasio, M., Magnaguagno, F., Pistorio, A., Valle, M., Martinoli, C., . . . Martini, A. (2008). Magnetic resonance imaging, ultrasonography, and conventional radiography in the assessment of bone erosions in juvenile idiopathic arthritis. Arthritis Care Research, 59(12), 1764-1772. doi: 10.1002/art.24313

Masi, J., Sell, C., Phan, C., Han, E., Newitt, D., Steinbach, L., . . . Link, T. (2005). Cartilage MR Imaging at 3.0 versus That at 1.5 T: Preliminary Results in a Porcine Model. Radiology, 236(1), 140-150. doi: 10.1148/radiol.2361040747

McKeon, B., Bono, J., Richmond, J. (2009). Knee Arthroscopy: Springer.

Mills, D., Pollock, V. (1980). Stabilizing feedback system for synchrotron radiation monochromators. Review of Scientific Instruments, 51(12), 1664-1668. doi: 10.1063/1.1136146

Mollenhauer, J., Aurich, M., Zhong, Z., Muehleman, C., Cole, C., Hasnah, M., . . . Chapman, L. D. (2002). Diffraction-enhanced X-ray imaging of articular cartilage. Osteoarthritis and Cartilage, 10(3), 163-171.

Muehleman, C., Chapman, L. D., Kuettner, K., Rieff, J., Mollenhauer, J., Massuda, K., Zhong, Z. (2003). Radiography of rabbit articular cartilage with diffraction-enhanced imaging. Anat Rec A Discov Mol Cell Evol Biol, 272(1), 392-397. doi: 10.1002/ar.a.10043

Muehleman, C., Fogarty, D., Reinhart, B., Tzvetkov, T., Li, J., Nesch, I. (2010). In-laboratory diffraction-enhanced X-ray imaging for articular cartilage. Clin Anat, 23(5), 530-538. doi: 10.1002/ca.20993

Muehleman, C., Li, J., Connor, D., Parham, C., Pisano, E., Zhong, Z. (2009). Diffraction-enhanced imaging of musculoskeletal tissues using a conventional x-ray tube. Acad Radiol, 16(8), 918-923. doi: 10.1016/j.acra.2009.04.006

Muehleman, C., Li, J., Zhong, Z. (2006). Preliminary study on diffraction enhanced radiographic imaging for a canine model of cartilage damage. Osteoarthritis Cartilage, 14(9), 882-888. doi: 10.1016/j.joca.2006.02.011

Muehleman, C., Majumdar, S., Issever, A., Arfelli, F., Menk, R., Rigon, L., . . . Mollenhauer, J. (2004). X-ray detection of structural orientation in human articular cartilage. Osteoarthritis Cartilage, 12(2), 97-105.

Nesch, I., Fogarty, D., Tzvetkov, T., Reinhart, B., Walus, A., Khelashvili, G., . . . Chapman, L. D. (2009). The design and application of an in-laboratory diffraction-enhanced x-ray imaging instrument. Rev Sci Instrum, 80(9), 093702. doi: 10.1063/1.3213621

Nissi, M., Toth, F., Zhang, J., Schmitter, S., Benson, M., Carlson, C., Ellermann, J. (2014). Susceptibility weighted imaging of cartilage canals in porcine epiphyseal growth cartilage ex vivo and in vivo. Magnetic Resonance in Medicine, 71(6), 2197-2205. doi: 10.1002/mrm.24863

Oen, K., Reed, M., Malleson, P., Cabral, D., Petty, R., Rosenberg, A., Cheang, M. (2003). Radiologic outcome and its relationship to functional disability in juvenile rheumatoid arthritis. The Journal of Rheumatology, 30(4), 832-840.

Oltulu, O., Zhong, Z., Hasnah, M., Wernick, M., Chapman, L. D. (2003). Extraction of extinction, refraction and absorption properties in diffraction enhanced imaging. Journal of Physics D: Applied Physics, 36(17), 2152.

Pakin, S., Cavalcanti, C., La Rocca, R., Schweitzer, M., Regatte, R. (2006). Ultra–High-Field MRI of Knee Joint at 7.0T: Preliminary Experience. Academic Radiology, 13(9), 1135-1142. doi: http://dx.doi.org/10.1016/j.acra.2006.06.007

Parham, C., Zhong, Z., Connor, D., Chapman, L. D., Pisano, E., Parham, C., . . . Pisano, E. (2009). Design and implementation of a compact low-dose diffraction enhanced medical imaging system. Academic Radiology, 16(8), 911-917.

Petty, R., Southwood, T., Manners, P., Baum, J., Glass, D., Goldenberg, J., . . . Woo, P. (2004). International League of Associations for Rheumatology classification of juvenile idiopathic arthritis: second revision, Edmonton, 2001. J Rheumatol, 31(2), 390-392.

PHAC. (2010). (Public Health Agency of Canada) Canadian Paediatric Surveillance Program: 2009 Results. from http://www.arthritis.ca

PHAC. (2011). (Public Health Agency of Canada) Life with Arthritis in Canada: A personal and public health challenge. 2013, from http://www.phac-aspc.gc.ca/cd-mc/arthritis-arthrite/lwaic-vaaac-10/3-eng.php

Pisano, E., Johnston, R., Chapman, L. D., Geradts, J., Iacocca, M., Livasy, C., . . . Thomlinson, W. (2000). Human breast cancer specimens: diffraction-enhanced imaging with histologic correlation--improved conspicuity of lesion detail compared with digital radiography. Radiology, 214(3), 895-901.

Podgorsak, E. (2006). Radiation Physics for Medical Physicists: Springer Berlin Heidelberg.

Rasband, W. (1997). ImageJ 1.44p (Version 1.6.0_20) [32-bit]. USA: National Institutes of Health. Retrieved from http://imagej.nih.gov/ij/

Reicher, M., Rauschning, W., Gold, R., Bassett, L., Lufkin, R., Glen, W. (1985). High-resolution magnetic resonance imaging of the knee joint: normal anatomy. American Journal of Roentgenology, 145(5), 895-902. doi: 10.2214/ajr.145.5.895

Rhoades, G., Belev, G., Rosenberg, A., Chapman, L. D. (2013). A Novel Analyzer Control System for Diffraction Enhanced Imaging. *Journal of Physics: Conference Series, 425*. doi: 10.1088/1742-6596/425/2/022003

Rinck, P. (2015, 1 Jan 2015). Magnetic Resonance in Medicine. The Basic Textbook of the European Magnetic Resonance Forum. 8th. Retrieved May 09, 2015, from http://www.magnetic-resonance.org/ch/21-01.html

Schoth, F., Kraemer, N., Niendorf, T., Hohl, C., Gunther, R., Krombach, G. (2008). Comparison of image quality in magnetic resonance imaging of the knee at 1.5 and 3.0 Tesla using 32-channel receiver coils. European Radiology, 18(10), 2258-2264. doi: 10.1007/s00330-008-0972-3

Seidel, T., Hammer, N., Garnov, N., Schneider, G., Steinke, H. (2013). An algorithm for the calculation of three-dimensional collagen fiber orientation in ligaments using angle-sensitive MRI. Magnetic Resonance in Medicine, 69(6), 1594-1602. doi: 10.1002/mrm.24408

Seo, S., Sunaguchi, N., Yuasa, T., Huo, Q., Ando, M., Choi, G., . . . Kim, J. (2012). Visualization of microvascular proliferation as a tumor infiltration structure in rat glioma specimens using the diffraction-enhanced imaging in-plane CT technique. Phys Med Biol, 57(5), 1251-1262. doi: 10.1088/0031-9155/57/5/1251

Shtern, F. (1992). Digital mammography and related technologies: a perspective from the National Cancer Institute. Radiology, 183(3), 629-630. doi: 10.1148/radiology.183.3.1584908

Stanich, J., Carter, J., Whittum-Hudson, J. (2009). Rheumatoid arthritis: disease or syndrome. Open Access Rheumatology Research and Reviews, 1, 179-192.

Thakkar, R., Flammang, A., Chhabra, A., Padua, A., Carrino, J. (2012). 3-T MR Imaging of Cartilage Using 3D Dual-Echo Steady State Sequences. Paper presented at the AMERICAN JOURNAL OF ROENTGENOLOGY.

Theysohn, J., Kraff, O., Maderwald, S., Kokulinsky, P., Ladd, M., Barkhausen, J., Ladd, S. (2013). MRI of the ankle joint in healthy non-athletes and in marathon runners: image quality issues at 7.0 T compared to 1.5 T. Skeletal Radiology, 42(2), 261-267. doi: 10.1007/s00256-012-1454-x

Tóth, F., Nissi, M., Zhang, J., Benson, M., Schmitter, S., Ellermann, J., Carlson, C. (2013). Histological confirmation and biological significance of cartilage canals demonstrated using high field MRI in swine at predilection sites of osteochondrosis. Journal of Orthopaedic Research, 31(12), 2006-2012. doi: 10.1002/jor.22449

Vande Berg, B., Lecouvet, F., Poilvache, P., Jamart, J., Materne, R., Lengele, B., . . . Malghem, J. (2002). Assessment of Knee Cartilage in Cadavers with Dual-Detector Spiral CT Arthrography and MR Imaging. Radiology, 222(2), 430-436. doi: 10.1148/radiol.2222010597

Wang, M., Zhu, P., Zhang, K., Hu, X., Huang, W., Cen, Y., . . . Wang, J. (2007). A new method to extract angle of refraction in diffraction enhanced imaging computed tomography. Journal of Physics D: Applied Physics, 40(22), 6917.

Wang, Y., Yin, W. (2010). Sparse Signal Reconstruction via Iterative Support Detection. SIAM Journal on Imaging Sciences, 3(3), 462-491. doi: 10.1137/090772447

Webb, M., Belev, G., Wysokinski, T., Chapman, L. D. (2013). Diffraction enhanced imaging computed tomography (DEI-CT) at the BMIT facility at the Canadian Light Source. Journal of Instrumentation, 8(08), C08002.

Wernick, M., Wirjadi, O., Chapman, L. D., Zhong, Z., Galatsanos, N., Yang, Y., . . . Muehleman, C. (2003). Multiple-image radiography. Physics in Medicine and Biology, 48(23), 3875-3895. doi: Pii S0031-9155(03)65305-4

Wiebe, S., Rhoades, G., Wei, Z., Rosenberg, A., Belev, G., Chapman, L. D. (2013). Understanding refraction contrast using a comparison of absorption and refraction computed tomographic techniques. Journal of Instrumentation, 8(05), C05004.

Wiedemann, H. (2003). Synchrotron Radiation (1 ed.): Springer-Verlag Berlin Heidelberg.

Wilson-Gerwing, T., Pratt, I., Cooper, D., Silver, T., Rosenberg, A. (2013). Age-related differences in collagen-induced arthritis: clinical and imaging correlations. Comp Med, 63(6), 498-502.

Wilson, D., Mc Walter, E., Johnston, J. (2009). The Measurement of Joint Mechanics and Their Role in Osteoarthritis Genesis and Progression. Medical Clinics of North America, 93(1), 67-82. doi: http://dx.doi.org/10.1016/j.mcna.2008.08.004

Young, L., Parham, C., Zhong, Z., Chapman, L. D., Reaney, M. (2007). Non-destructive diffraction enhanced imaging of seeds. Journal of Experimental Botany, 58(10), 2513-2523. doi: 10.1093/jxb/erm116

Zachariasen, W. (1945). Theory of X-Ray Diffraction in Crystals. New York: John Wiley and Sons.

Zhong, Z., Chapman, L. D., Hasnah, M., Johnston, E., Kiss, M., Oltulu, O., . . . Thomlinson, W. (2002). X-ray diffraction order selection with a prism in DEI (abstract). Review of Scientific Instruments, 73(3), 1614.

Zhong, Z., Thomlinson, W., Chapman, L. D., Sayers, D. (2000). Implementation of diffraction-enhanced imaging experiments: at the NSLS and APS. Nucl Instr Meth Phys Res A, 450(2-3), 556.

Zschornack, G. (2007). Handbook of X-Ray Data: Springer Berlin Heidelberg.

Zwanenburg, J., van der Kolk, A., Luijten, P. (2013). Ultra-High-Field MR Imaging: Research Tool or Clinical Need? PET Clinics, 8(3), 311-328. doi: http://dx.doi.org/10.1016/j.cpet.2013.03.004